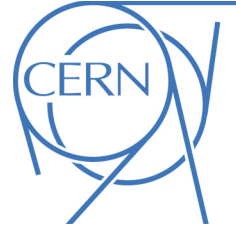




ATLAS NOTE

ATL-COM-PHYS-2011-052

April 29, 2011



Measurement of the W^+W^- production cross section in proton-proton collisions at $\sqrt{s} = 7$ TeV with the ATLAS detector

J. Alison^l, J. Barreiro Guimarães da Costa^p, T. Dai^g, J. Ebke^h, J. Elmsheuser^h, C. Hays^k, Y. Hernandezⁿ, T. M. Hong^l, S.-c. Hsu^a, J. Kroll^l, A. Kruse^o, J. Kunkle^l, D. Levin^g, S. Li^{d,f}, X. Li^g, E. Lipeles^l, J. Liu^g, L. Liu^g, Y. Liu^d, H. Ma^b, T. Masubuchi^m, B. Mellado^o, E. Monnier^f, M. Neubauerⁱ, R. Ospanov^l, M.-A. Pleier^b, A. Pranko^a, X. Ruan^{c,j}, R. Thun^g, D. Varouchas^a, E. Williams^e, G. Wooden^k, Y. Wu^{g,d}, H. Yang^g, Z. Zhang^j, Z. Zhao^d, B. Zhou^g, J. Zhu^g, Y. Zhu^o

^a*Lawrence Berkeley National Laboratory*

^b*Brookhaven National Laboratory*

^c*Institute of High Energy Physics, Chinese Academy of Sciences*

^d*University of Science & Technology of China (USTC)*

^e*Columbia University*

^f*CPPM, Aix-Marseille Université*

^g*The University of Michigan*

^h*Ludwig-Maximilians-Universität München*

ⁱ*University of Illinois*

^j*LAL, Univ. Paris-Sud and CNRS/IN2P3*

^k*Oxford University*

^l*University of Pennsylvania*

^m*University of Tokyo*

ⁿ*Instituto de Física Corpuscular (IFIC)*

^o*University of Wisconsin*

^p*Harvard University*

Abstract

This note presents a measurement of W^+W^- production in pp collisions at $\sqrt{s} = 7$ TeV using data collected by the ATLAS experiment from March to October 2010, corresponding to a total integrated luminosity of 34 pb^{-1} . The analysis focuses on the experimental signature of two isolated leptons with high transverse momenta and a large missing transverse energy in an event ($\ell^+\ell^- \not{E}_T$), where $\ell = e$ or μ . The major background for such final states comes from $V+\text{jets}$ (V denotes the vector bosons W and Z) and top events. The W^+W^- detection efficiencies are determined using data from the $Z \rightarrow \ell^+\ell^-$ process. These efficiencies are compared to MC signal simulations. The influence of backgrounds on $W^+W^- \rightarrow \ell^+\nu_\ell\ell^-\bar{\nu}_\ell$ detection is assessed using large MC samples of fully simulated background events. The $V+\text{jets}$, top and $Z/\gamma^* \rightarrow l^+l^-$ backgrounds are also estimated using data-driven methods. A total of eight candidates are selected with a jet veto requirement in the final state. The background contribution is estimated to be 1.7 ± 0.6 events. Our observation is consistent with the SM next-to-leading order predictions of W^+W^- production. Using a log-likelihood fit method, the W^+W^- production cross-section is measured to be $41.2^{+20.5}_{-16.2} \text{ (stat)} \pm 4.9 \text{ (syst) pb}$. The probability for the estimated background to fluctuate up to at least the observed number of events is 1.2×10^{-3} , corresponding to a signal significance of 3.0 standard deviations.

Contents

| | | |
|----------|--|-----------|
| 1 | Introduction | 3 |
| 2 | Analysis Overview | 4 |
| 2.1 | Event Selection Summary | 4 |
| 2.2 | Cross-section Calculation | 5 |
| 2.3 | Signal Acceptance and Background Modeling | 5 |
| 3 | Data samples | 6 |
| 4 | Signal and background MC samples | 7 |
| 5 | Lepton triggers | 11 |
| 5.1 | Tag and probe method for trigger efficiencies | 11 |
| 5.2 | Muon trigger efficiency | 12 |
| 5.2.1 | Comparison of data and MC trigger efficiencies | 13 |
| 5.2.2 | Systematic uncertainties on the trigger scale factor | 13 |
| 5.3 | Electron trigger efficiency | 14 |
| 5.3.1 | Comparison of data and MC trigger efficiencies | 14 |
| 5.3.2 | Scale factor calculation | 15 |
| 5.3.3 | Systematic uncertainties on trigger scale factor | 15 |
| 5.3.4 | Comparison with egamma group recommendation | 16 |
| 5.4 | Event-based scale factor calculation | 16 |
| 6 | Physics object reconstruction and identification | 23 |
| 6.1 | Electron identification and efficiencies | 23 |
| 6.1.1 | Determination of the Isolation and Impact Parameter Requirement Efficiencies | 24 |
| 6.1.2 | Electron Energy Calibration and Oversmearing | 25 |
| 6.2 | Muon identification and efficiencies | 25 |
| 6.2.1 | CB muon efficiency (ϵ_{CB}) | 26 |
| 6.2.2 | ID muon efficiency (ϵ_{ID}) | 28 |
| 6.2.3 | Muon isolation efficiency (ϵ_{iso}) | 29 |
| 6.2.4 | Overall muon reconstruction and identification efficiency ($\epsilon_{CB} \times \epsilon_{ID} \times \epsilon_{iso}$) | 30 |
| 6.2.5 | Muon momentum resolution and scale | 30 |
| 6.3 | Jet Reconstruction | 31 |
| 6.3.1 | Jet energy scale uncertainty effects on jet veto | 31 |
| 6.3.2 | Extraction of the jet veto efficiency from data | 31 |
| 6.4 | Missing Transverse Energy Determination | 33 |
| 6.4.1 | Relative Missing Energy | 33 |
| 6.4.2 | Missing Energy Smearing | 34 |
| 6.4.3 | Missing Transverse Energy Acceptance | 34 |
| 6.5 | Event vertices and pileup | 34 |
| 6.5.1 | Reweighting for pile-up MC using event vertices | 34 |
| 6.5.2 | Lepton track vertex and cut efficiencies | 40 |
| 6.6 | Object Overlap Removal | 40 |
| 6.7 | Summary of Overall Scale Factors | 42 |

| | |
|---|-----------|
| 7 Event Selection | 43 |
| 7.1 W^+W^- event selection criteria | 43 |
| 7.1.1 Relative MET cut optimization | 50 |
| 7.2 Event selection cut-flow | 52 |
| 7.3 Distributions for selected events | 52 |
| 7.4 W^+W^- signal event selection cut flow and acceptance | 52 |
| 8 Background estimation with data driven methods | 55 |
| 8.1 $W+jets$ background | 55 |
| 8.1.1 Data driven $W+jets$ background estimation | 55 |
| 8.1.2 Fake factor measurement | 56 |
| 8.1.3 $W+jets$ control regions | 59 |
| 8.1.4 $W+jets$ background prediction | 60 |
| 8.2 Drell-Yan Background | 64 |
| 8.2.1 Comparison of Monte Carlo Generators | 64 |
| 8.2.2 Systematic Uncertainty Estimate | 64 |
| 8.3 Background from cosmic muons | 67 |
| 8.4 Top Background | 69 |
| 8.4.1 Top Background Estimation from MC | 69 |
| 8.4.2 Initial and Final State Radiation of Top | 69 |
| 8.4.3 Top background estimation from data using events with large jet multiplicity (Method A) | 70 |
| 8.4.4 Top background estimation from data using a b -tagged control sample (Method B) | 71 |
| 8.4.5 Summary of top background estimates | 73 |
| 9 Systematics | 74 |
| 10 Results | 77 |
| 10.1 Observed W^+W^- candidates and MC expectations | 77 |
| 10.2 Measurement of the W^+W^- production cross section | 78 |
| 10.3 W^+W^- detection sensitivity | 79 |
| A W+jets background validation | 83 |
| B W+jets background cross check. | 83 |
| B.0.1 Calculation of the fake factor | 83 |
| B.0.2 Non- $W+jet$ Correction to $W+jet$ Control Region | 85 |
| B.0.3 Same sign control region | 85 |
| B.0.4 Application to Signal Region | 86 |
| B.0.5 Comparison of $W+jets$ methods | 86 |
| C Estimate $W+jets$ background using matrix method | 90 |
| D MET Studies | 92 |
| E PDF Uncertainty of WW Acceptance | 97 |
| F Additional W^+W^- Plots | 99 |

1 Introduction

The observation of W^+W^- is one of the first milestones in the ATLAS physics program. The leading-order Feynman diagrams for the dominant W^+W^- production mechanism at the LHC are shown in Figure 1 and are characterized by a quark-antiquark initial state.

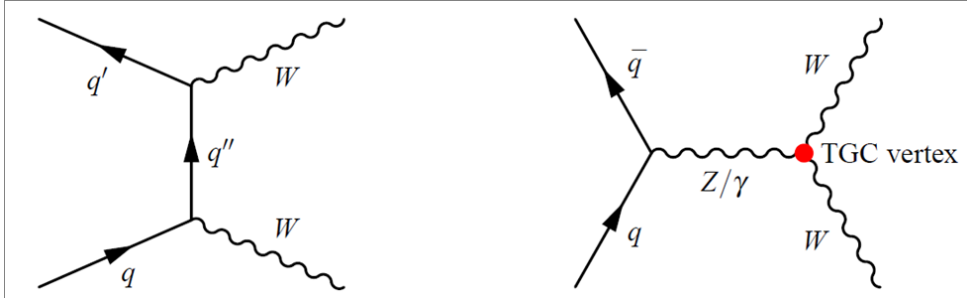


Figure 1: The Standard Model tree-level Feynman diagrams for W^+W^- production through the $q\bar{q}$ initial state in hadron colliders. The s -channel diagram, on the right, contains the WWZ and $WW\gamma$ trilinear gauge boson coupling (TGC) vertices.

Another non-negligible mechanism of W^+W^- production at the LHC is gluon-gluon fusion. The Feynman diagrams are shown in Figure 2. This process contributes $\sim 3\%$ event rate to the total W^+W^- production at $\sqrt{s} = 7$ TeV.

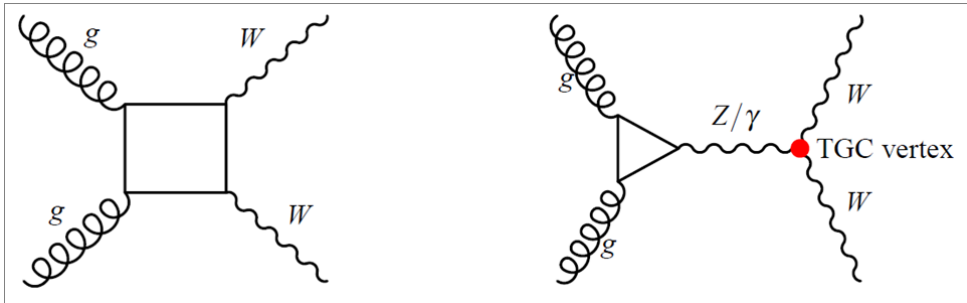


Figure 2: The Standard Model Feynman diagrams for W^+W^- production through gluon-gluon fusion in hadron colliders. Please note that the Z -exchange triangle diagrams cancel when summed over ‘massless’ up- and down-type contributions.

The measurement of the W^+W^- production cross section at the LHC will provide an important test of the Standard Model (SM) through the study of the charged triple gauge boson couplings that result from the non-abelian structure of the gauge symmetry group, $SU(2)_L \times U(1)_Y$, of the SM. The W^+W^- events produced through the SM process at the LHC are an irreducible background to Higgs detection in the W^+W^- final state. Understanding the SM W^+W^- production and ATLAS detection sensitivity to W -pair events is crucial to Higgs searches at the LHC.

This paper presents the observation of W^+W^- in dilepton channels with the ATLAS detector in LHC proton-proton collisions at $\sqrt{s} = 7$ TeV. The analysis and results are based on an integrated luminosity of 34 pb^{-1} collected by ATLAS in 2010 with a fully operational detector and stable beam conditions.

2 Analysis Overview

Because the W^+W^- production cross-section is so much smaller than the four jet QCD and $W+jets$ cross-sections, the W^+W^- signal is identified in the $\ell\ell\nu\nu$ final state, requiring both Ws to decay to leptons. The experimental signature of the $\ell\ell\nu\nu$ final state is then any combination of two e or μ leptons (including e or μ leptons that are the decay products of τ leptons from the W^+W^- decays) and missing transverse energy, E_T^{miss} . The $t\bar{t}$ process also produces a final state with two W bosons; however this is not considered signal and is suppressed in the signal selection by vetoing on the presence of any jets. In this final state there is no dominant background, but many moderate background contributions:

- $W+jets$ with a jet misidentified as a lepton,
- $Z+jets$ with E_T^{miss} due to mismeasurement or particles exiting down the beamline,
- $W + \gamma$ with the γ identified as an electron,
- $t\bar{t}$ where both b -jets are not detected,
- $WZ \rightarrow \ell\ell\nu\nu$ where one final state lepton is not detected,
- $ZZ \rightarrow \ell\ell\nu\nu$ where the dilepton invariant mass is not near the Z -mass, and
- finally it is possible to get background from multijet QCD where both leptons and the missing energy are due to misidentification.

2.1 Event Selection Summary

The selection criteria are designed to identify the final state $\ell\ell E_T^{\text{miss}}$ while suppressing the above backgrounds. At the conceptual level the selection is

- a single electron or muon trigger,
- exactly two oppositely charged isolated leptons (e or μ) over 20 GeV in p_T ,
- $E_{T, \text{Rel}}^{\text{miss}} > 40$ GeV for the ee and $\mu\mu$ channels and $E_{T, \text{Rel}}^{\text{miss}} > 20$ GeV for the $e\mu$ channel to suppress $Z \rightarrow \ell^+\ell^-$ where ℓ includes e , μ , and τ , and the $E_{T, \text{Rel}}^{\text{miss}}$ variable, defined in Equation 8, is the E_T^{miss} transverse to the nearest lepton or jet if that object is in the same hemisphere and E_T^{miss} itself otherwise,
- $|M_{\ell^+\ell^-} - M_Z| > 10$ GeV (ee , $\mu\mu$ channels) to further suppress $Z \rightarrow \ell^+\ell^-$,
- $M_{\ell^+\ell^-} > 15$ GeV (ee , $\mu\mu$ channels) to suppress multijet QCD and Υ ,
- and finally no jets with $E_T > 20$ GeV and $|\eta| < 3$ to suppress $t\bar{t}$.

The requirement of exactly two leptons helps to suppress contributions from the $WZ \rightarrow \ell\ell\nu\nu$ sample. The exact trigger, physics object, and event selections are detailed in Sections 5, 6, and 7.

2.2 Cross-section Calculation

The formula used to determine the cross-section is

$$\sigma_{WW} = \frac{N_{obs} - N_{bkg}}{\epsilon \mathcal{A} \mathcal{L} Br} \quad (1)$$

where N_{obs} is the number of observed events, N_{bkg} is the number of expected background, $\epsilon \mathcal{A}$ is the acceptance times efficiency which are treated as one number, Br is the branching fraction of dileptonic W^+W^- decays and \mathcal{L} is the integrated luminosity. In much of the text the acceptance is effectively reported as the expected number of reconstructed W^+W^- events in the 34 pb^{-1} sample. The acceptance times efficiency can be extracted from this number as $N_{WW}/(\sigma_{SM} \times \mathcal{L} \times Br)$. Using the SM cross-sections reported in Table 3 and the PDG branching fraction (including $\tau \rightarrow e\nu\nu$ and $\tau \rightarrow \mu\nu\nu$), 105 events of $WW \rightarrow \ell\ell\nu\nu$ have been produced before reconstruction. This means the final acceptance is $\epsilon \mathcal{A} = N_{reco}/N_{prod} = 7.4/105 = 7\%$ (see Section 10.2 for N_{reco}).

2.3 Signal Acceptance and Background Modeling

The signal and background contributions expected from the data are mainly modeled with Monte Carlo simulation corrected with several data-driven measurements. The one exception to this is the W +jets background where the modeling of the rare fragmentation effects which lead a jet to be misidentified as a lepton are not expected to be reliable in the simulation and a fully data-driven method is used (see Section 8.1). The corrections applied are:

| Correction | see Section |
|------------------------------------|-----------------------|
| Electron trigger efficiency | 5.3 |
| Muon trigger efficiency | 5.2 |
| Electron identification efficiency | 6.1 |
| Muon identification efficiency | 6.2 |
| Muon p_T smearing | 6.2.5 |
| Electron energy scale (data only) | 6.1.2 |
| Pile-up vertex reweighting | 6.5.1 |

In the case of correction factors that are run period dependent, the MC events samples are divided into samples reflecting the integrated luminosities in each period and the correction factors relevant to the corresponding period are applied.

3 Data samples

This study uses data collected at a center of mass energy of $\sqrt{s} = 7$ TeV in proton-proton collisions by the ATLAS experiment from March 30 until October 31, 2010 (data-taking periods A to I2). The corresponding total integrated luminosity after the data quality selection applied in this analysis is 34 pb^{-1} , as determined by the standard ATLAS tool for luminosity calculation [1]. The uncertainty of the integrated luminosity obtained from van der Meer scans is 3.4% and is dominated by the knowledge of the LHC beam currents. A single *Good Run List* (GRL) [2] created from the data quality flags as defined in tags `DetStatus-v03-pass1-analysis-2010X`, using the `StandardModel.Wmunuchannel1` configuration of the ATLAS GRL generator page is used for all three analysis channels. The analysis is based on ATHENA release 15, hence not using the fall 2010 data reprocessing and its data-quality.

The integrated luminosity for different run periods and for the different lepton triggers used in this analysis is listed in Table 1. The data for this analysis originate from the lepton streams shown in Table 2. The data are analyzed by different groups using either AOD files directly or D3PD ntuples. The D3PD ntuples are converted from electron/photon and muon streams (AOD data) [3] as common datasets for the SM WW and the Higgs $H \rightarrow WW$ working groups. A *filter* which requires at least one muon or electron candidate with $p_T > 10$ GeV is used when the AOD datasets are converted to D3PD data samples. The ATLAS central production uses ATHENA v15.6.13.2 to produce the datasets for this analysis. The total number of events and the number of events that passed the *filter* from each data file are listed on the W^+W^- analysis twiki page [3].

| Trigger | Run Period | Run Period | Run Period | Run Period |
|------------------|---------------------------------------|--|---|---|
| | A - E3 $\int Ldt [\text{pb}^{-1}]$ | E4 - G1 $\int Ldt [\text{pb}^{-1}]$ | G2 - I1 (run 167576) $\int Ldt [\text{pb}^{-1}]$ | I1 (run 167607) - I2 $\int Ldt [\text{pb}^{-1}]$ |
| L1_MU10 | 0.776 | | | |
| EF_mu10_MG | | 3.02 | | |
| EF_mu13_MG | | | 15.83 | |
| EF_mu13_MG_tight | | | | 15.57 |
| L1_EM14 | 0.776 | | | |
| EF_e15_medium | | 3.02 | 15.83 | |
| Total (A-I2) | 34 pb^{-1} (*) | | | 15.57 |

Table 1: Integrated luminosities for different run periods and single lepton signal triggers used in the W^+W^- analysis. L1_MU10, EF_mu10_MG, EF_mu13_MG and EF_mu13_MG_tight triggers are used in the $\mu\mu$ channel, while L1_EM14 and EF_e15_medium triggers are used in the ee channel. The *OR* of these triggers is used in the $e\mu$ channel analysis. Note that the transition between EF_mu13_MG and EF_mu13_MG_tight triggers does not coincide with the transition of run period I1. (*) 34 pb^{-1} is scaled down from the original 35.2 pb^{-1} .

| Run Period | Muon Stream | Electron Stream |
|----------------------|-------------|-----------------|
| A-D (152166-159224) | MuonswBeam | L1Calo |
| E-I (160387-167844) | Muons | Egamma |

Table 2: Data streams for different run periods.

4 Signal and background MC samples

The W^+W^- production processes from the quark initial states, $q\bar{q} \rightarrow W^+W^- \rightarrow \ell^+\nu_\ell\ell^-\bar{\nu}_\ell$, and subsequent pure leptonic decays, are modeled by the MC@NLO [4] Monte Carlo generator with parton density function (PDF) set CTEQ6.6, which incorporates the next-to-leading-order (NLO) QCD matrix elements into the parton shower by interfacing to the HERWIG/Jimmy [5] programs. The W^+W^- production cross section from $q\bar{q}'$ annihilation is calculated using MC@NLO with the CTEQ6.6 PDF set and MCFM with the MSTW2008 PDF set, yielding 43.15 ± 2.16 pb and 44.92 ± 2.25 pb, respectively. The gauge-boson decays into τ leptons are included in the MC event generator and these τ leptons decay to all the possible final states. The hard gluon emission is treated with a NLO computation and soft/collinear emission is treated with a regular parton shower MC. The matching between these two regions is smooth (no double-counting). W -boson width and spin-spin correlations are included in the generator. The process of W^+W^- production via gluon-gluon fusion with leptonic decays of the W bosons, $gg \rightarrow W^+W^- \rightarrow \ell^+\nu_\ell\ell^-\bar{\nu}_\ell$, is modeled by the MC generator gg2ww [6] and PDF set CTEQ6.6 (using MSTW2008 instead raises the cross section from 1.2 to 1.3 pb). Table 3 lists all the W^+W^- MC signal samples used in this analysis and corresponding cross sections (calculated using MCFM with PDF set MSTW2008 [7] for $q\bar{q}'$ annihilation and gg2ww with PDF set MSTW2008 for gluon-gluon fusion).

| Process | cross-section [fb] | ϵ_{filter} | N_{MC} | Generator |
|---|--------------------|----------------------------|----------|-----------|
| $q\bar{q}' \rightarrow W^+W^- \rightarrow e^+\nu e^-\nu$ | 524 | 1.0 | 49990 | MC@NLO |
| $q\bar{q}' \rightarrow W^+W^- \rightarrow \mu^+\nu\mu^-\nu$ | 524 | 1.0 | 49939 | MC@NLO |
| $q\bar{q}' \rightarrow W^+W^- \rightarrow e^+\nu\mu^-\nu$ | 524 | 1.0 | 49944 | MC@NLO |
| $q\bar{q}' \rightarrow W^+W^- \rightarrow \mu^+\nu e^-\nu$ | 524 | 1.0 | 49988 | MC@NLO |
| $q\bar{q}' \rightarrow W^+W^- \rightarrow e^+\nu\tau^-\nu$ | 524 | 1.0 | 49944 | MC@NLO |
| $q\bar{q}' \rightarrow W^+W^- \rightarrow \mu^+\nu\tau^-\nu$ | 524 | 1.0 | 49942 | MC@NLO |
| $q\bar{q}' \rightarrow W^+W^- \rightarrow \tau^+\nu\mu^-\nu$ | 524 | 1.0 | 49992 | MC@NLO |
| $q\bar{q}' \rightarrow W^+W^- \rightarrow \tau^+\nu e^-\nu$ | 524 | 1.0 | 49942 | MC@NLO |
| $q\bar{q}' \rightarrow W^+W^- \rightarrow \tau^+\nu\tau^-\nu$ | 524 | 1.0 | 49937 | MC@NLO |
| $gg \rightarrow W^+W^- \rightarrow e^+\nu e^-\nu$ | 15.5 | .9885 | 9999 | gg2ww |
| $gg \rightarrow W^+W^- \rightarrow \mu^+\nu\mu^-\nu$ | 15.5 | .9897 | 9999 | gg2ww |
| $gg \rightarrow W^+W^- \rightarrow e^+\nu\mu^-\nu$ | 15.5 | .9893 | 9998 | gg2ww |
| $gg \rightarrow W^+W^- \rightarrow \mu^+\nu e^-\nu$ | 15.5 | .9888 | 9999 | gg2ww |
| $gg \rightarrow W^+W^- \rightarrow e^+\nu\tau^-\nu$ | 15.5 | .9231 | 9999 | gg2ww |
| $gg \rightarrow W^+W^- \rightarrow \mu^+\nu\tau^-\nu$ | 15.5 | .9281 | 9949 | gg2ww |
| $gg \rightarrow W^+W^- \rightarrow \tau^+\nu\mu^-\nu$ | 15.5 | .9272 | 10000 | gg2ww |
| $gg \rightarrow W^+W^- \rightarrow \tau^+\nu e^-\nu$ | 15.5 | .9236 | 10000 | gg2ww |
| $gg \rightarrow W^+W^- \rightarrow \tau^+\nu\tau^-\nu$ | 15.5 | .3268 | 9999 | gg2ww |

Table 3: The W^+W^- signal production processes, cross-sections and numbers of fully simulated MC events. The MC simulation ‘filter’ is an event selection at the generator level. The corresponding filter efficiencies are given in the table. We also indicate the MC generators used to produce the MC events.

Major backgrounds for W^+W^- signal detection come from jets associated with W or Z gauge bosons ($V+jets$, Table 4) and top events ($t\bar{t}$ and single top, Table 5). We use MC@NLO to model the $t\bar{t}$ and single top events and ALPGEN to model the $V+jets$ background. Due to a bug when modelling the τ polarisation with ALPGEN, we use PYTHIA [8], a LO MC generator, to model $V+jets$ background with τ final states. Events with dileptons from Drell-Yan production (Table 4) are also modeled with ALPGEN or PYTHIA, depending on the presence of τ leptons in the final state. Events with heavy flavor dijets (Table 5) are modeled with PYTHIAB. The diboson processes WZ , ZZ and $W/Z + \gamma$ are modeled with MC@NLO,

HERWIG and **MADGRAPH**, respectively (Table 6).

The cross-sections for the different processes, the generator names, the generator level filter efficiencies and total number of events are shown in the tables. Whenever LO event generators are used, the cross-sections are corrected by using k-factors to NLO or NNLO (if available) matrix element calculations [9].

All the MC samples are simulated with in-time pile-up with an average of two event collision vertices. Additional technical details such as MC dataset numbers and event yields after D3PD single lepton filter selection are given on the SM WW analysis web pages [3]. The background MC samples generally correspond to $\sim 100\text{-}300 \text{ pb}^{-1}$ of integrated luminosity.

| Process | cross-section [pb] | k-factor | ϵ_{filter} | N_{MC} | Generator |
|---|--------------------|----------|----------------------------|----------|-----------|
| WenuNp0 | 6870.5 | 1.21 | 1 | 1381531 | ALPGEN |
| WenuNp1 | 1293.0 | 1.21 | 1 | 257958 | ALPGEN |
| WenuNp2 | 376.6 | 1.21 | 1 | 188896 | ALPGEN |
| WenuNp3 | 101.3 | 1.21 | 1 | 49978 | ALPGEN |
| WenuNp4 | 25.2 | 1.21 | 1 | 12991 | ALPGEN |
| WenuNp5 | 7.1 | 1.21 | 1 | 3449 | ALPGEN |
| WmunuNp0 | 6871.1 | 1.21 | 1 | 1386038 | ALPGEN |
| WmunuNp1 | 1294.7 | 1.21 | 1 | 255909 | ALPGEN |
| WmunuNp2 | 376.1 | 1.21 | 1 | 187860 | ALPGEN |
| WmunuNp3 | 100.7 | 1.21 | 1 | 49887 | ALPGEN |
| WmunuNp4 | 26.0 | 1.21 | 1 | 12991 | ALPGEN |
| WmunuNp5 | 7.1 | 1.21 | 1 | 3498 | ALPGEN |
| Wtaunu(incl) | 8941.5 | 1.17 | 1 | 999878 | PYTHIA |
| ZeeNp0($M > 40$ GeV) | 664 | 1.26 | 1 | 303966 | ALPGEN |
| ZeeNp1($M > 40$ GeV) | 132 | 1.26 | 1 | 62941 | ALPGEN |
| ZeeNp2($M > 40$ GeV) | 40 | 1.26 | 1 | 18997 | ALPGEN |
| ZeeNp3($M > 40$ GeV) | 11 | 1.26 | 1 | 5499 | ALPGEN |
| ZeeNp4($M > 40$ GeV) | 3 | 1.26 | 1 | 1499 | ALPGEN |
| ZeeNp5($M > 40$ GeV) | 0.75 | 1.26 | 1 | 500 | ALPGEN |
| ZmumuNp0($M > 40$ GeV) | 664 | 1.26 | 1 | 303947 | ALPGEN |
| ZmumuNp1($M > 40$ GeV) | 133 | 1.26 | 1 | 62996 | ALPGEN |
| ZmumuNp2($M > 40$ GeV) | 40 | 1.26 | 1 | 18993 | ALPGEN |
| ZmumuNp3($M > 40$ GeV) | 11 | 1.26 | 1 | 5497 | ALPGEN |
| ZmumuNp4($M > 40$ GeV) | 3 | 1.26 | 1 | 1499 | ALPGEN |
| ZmumuNp5($M > 40$ GeV) | 0.76 | 1.26 | 1 | 499 | ALPGEN |
| ZeeNp0($10 < M < 40$ GeV) | 3051.62 | 1.22 | 1 | 999443 | ALPGEN |
| ZeeNp1($10 < M < 40$ GeV) | 87.87 | 1.22 | 1 | 299849 | ALPGEN |
| ZeeNp2($10 < M < 40$ GeV) | 41.10 | 1.22 | 1 | 499638 | ALPGEN |
| ZeeNp3($10 < M < 40$ GeV) | 8.46 | 1.22 | 1 | 149763 | ALPGEN |
| ZeeNp4($10 < M < 40$ GeV) | 1.84 | 1.22 | 1 | 39983 | ALPGEN |
| ZeeNp5($10 < M < 40$ GeV) | 0.46 | 1.22 | 1 | 9996 | ALPGEN |
| ZmumuNp0($10 < M < 40$ GeV) | 3051.62 | 1.22 | 1 | 999236 | ALPGEN |
| ZmumuNp1($10 < M < 40$ GeV) | 87.87 | 1.22 | 1 | 299953 | ALPGEN |
| ZmumuNp2($10 < M < 40$ GeV) | 40.95 | 1.22 | 1 | 499578 | ALPGEN |
| ZmumuNp3($10 < M < 40$ GeV) | 8.41 | 1.22 | 1 | 149701 | ALPGEN |
| ZmumuNp4($10 < M < 40$ GeV) | 1.85 | 1.22 | 1 | 39983 | ALPGEN |
| ZmumuNp5($10 < M < 40$ GeV) | 0.46 | 1.22 | 1 | 9996 | ALPGEN |
| Ztautau($M > 60$ GeV) | 856.967 | 1.15 | 1 | 99980 | PYTHIA |
| Drell-Yan($\tau\tau, 10 < M < 60$ GeV) | 3454.0 | 1.15 | 1 | 99984 | PYTHIA |

Table 4: MC samples/processes used to model $Z+X$ and $W+X$ backgrounds, including $Z+\text{jets}$, $W+\text{jets}$ and Drell-Yan samples. The corresponding cross-sections, generator names, generator level filter efficiencies and total numbers of events are shown in this table. NpX (X=0..5) in the process name refers to the number of additional partons in the final state.

| Process | cross-section [pb] | k-factor | ϵ_{filter} | N_{MC} | Generator |
|----------------|--------------------|----------|----------------------------|----------|-----------|
| ttbar | 164.57 | 1 | 0.5562 | 999387 | MC@NLO |
| tchan->e | 6.34 | 1 | 1 | 9993 | MC@NLO |
| tchan->mu | 6.34 | 1 | 1 | 9997 | MC@NLO |
| tchan->tau | 6.34 | 1 | 1 | 10000 | MC@NLO |
| schan->e | 0.43 | 1 | 1 | 9950 | MC@NLO |
| schan->mu | 0.43 | 1 | 1 | 9996 | MC@NLO |
| schan->tau | 0.43 | 1 | 1 | 9996 | MC@NLO |
| Wt | 13.10 | 1 | 1 | 14995 | MC@NLO |
| bbcc_mu10mu10X | 2830.0 | 1 | 1 | 295084 | PYTHIA |
| bbcc_mu10e10X | 4017.0 | 1 | 1 | 788438 | PYTHIA |
| bbcc_e10e10X | 1693.0 | 1 | 1 | 285086 | PYTHIA |

Table 5: MC samples/processes used to model dijet and top backgrounds (including $t\bar{t}$ and single top). The corresponding cross-sections, generator names, generator level filter efficiencies and total numbers of events are shown in the table.

| Process | cross-section [pb] | k-factor | ϵ_{filter} | N_{MC} | Generator |
|-------------------------------|--------------------|----------|----------------------------|----------|-----------------|
| ZW ⁺ ->lnuqq | 1.69 | 1 | 1 | 24997 | MC@NLO |
| ZW ⁺ ->lnull | 0.16 | 1 | 1 | 24997 | MC@NLO |
| ZW ⁺ ->qql | 0.50 | 1 | 1 | 24987 | MC@NLO |
| ZW ⁺ ->taunull | 0.08 | 1 | 1 | 24996 | MC@NLO |
| ZW ⁺ ->lnutautau | 0.08 | 1 | 1 | 24995 | MC@NLO |
| ZW ⁺ ->taunutautau | 0.04 | 1 | 1 | 24998 | MC@NLO |
| ZW ⁻ ->lnuqq | 0.91 | 1 | 1 | 24989 | MC@NLO |
| ZW ⁻ ->lnull | 0.09 | 1 | 1 | 99884 | MC@NLO |
| ZW ⁻ ->qql | 0.27 | 1 | 1 | 99922 | MC@NLO |
| ZW ⁻ ->taunull | 0.04 | 1 | 1 | 24996 | MC@NLO |
| ZW ⁻ ->lnutautau | 0.04 | 1 | 1 | 24997 | MC@NLO |
| ZW ⁻ ->taunutautau | 0.02 | 1 | 1 | 24996 | MC@NLO |
| ZW ⁺ ->qqtautau | 0.25 | 1 | 1 | 24987 | MC@NLO |
| ZW ⁻ ->qqtautau | 0.13 | 1 | 1 | 24993 | MC@NLO |
| ZZ | 0.98 | 1.2 | 1 | 249725 | HERWIG |
| gammaWp(e) | 28.00 | 1 | 0.9 | 49948 | PYTHIA,MADGRAPH |
| gammaWp(mu) | 28.00 | 1 | 0.9 | 50000 | PYTHIA,MADGRAPH |
| gammaWp(tau) | 25.40 | 1 | 0.9 | 49943 | PYTHIA,MADGRAPH |
| gammaWm(e) | 18.53 | 1 | 0.9 | 49996 | PYTHIA,MADGRAPH |
| gammaWm(mu) | 18.62 | 1 | 0.9 | 49996 | PYTHIA,MADGRAPH |
| gammaWm(tau) | 16.80 | 1 | 0.9 | 49997 | PYTHIA,MADGRAPH |
| gammaZ(ee) | 9.63 | 1 | 0.9 | 49899 | PYTHIA,MADGRAPH |
| gammaZ(mumu) | 9.63 | 1 | 0.9 | 49996 | PYTHIA,MADGRAPH |
| gammaZ(tautau) | 9.41 | 1 | 0.15 | 49992 | PYTHIA,MADGRAPH |

Table 6: MC samples/processes used to model diboson backgrounds, including WZ , ZZ , $W\gamma$ and $Z\gamma$. The corresponding cross-sections, generator names, generator level filter efficiencies and total numbers of events are shown in the table.

5 Lepton triggers

The ATLAS trigger system consists of three stages: the hardware-based Level 1 (L1) trigger and the software-based Level 2 (L2) and Event Filter (EF) triggers, which are referred to collectively as the High Level Trigger (HLT). For events with electromagnetic clusters, the E_T is measured at L1 by trigger towers in a region of 0.1×0.1 in $\Delta\eta \times \Delta\phi$. The L1 muon trigger utilises a measurement of particle trajectories made by two parts of the muon detector: the Resistive Plate Chambers (RPC) in the barrel region and the Thin Gap Chambers (TGC) in the endcap region. Further requirements on the E_T are made by the HLT and additional quality criteria must be satisfied by electron candidates.

W^+W^- candidate events with multi-lepton final states are recorded with single muon and single electron triggers. The trigger p_T thresholds are different in different run periods due to the rapid increase in luminosity during the first year of LHC operation. Initially the HLT was not enabled, therefore only the L1 trigger could be used at the start of data-taking.

The trigger efficiencies for W^+W^- events, ϵ , are measured using the tag and probe method which is described in Section 5.1. It is assumed that the ratio of efficiencies measured using the tag and probe method is equivalent to the true ratio of efficiencies in the data and MC samples.

From these efficiencies, a per-lepton scale factor, SF, quantifying the difference between the trigger efficiency measured in data and MC can be defined as:

$$SF = \frac{\epsilon(Z, Data)}{\epsilon(Z, MC)}. \quad (2)$$

5.1 Tag and probe method for trigger efficiencies

To calculate the trigger efficiencies in data, the tag and probe method may be used. This method selects a very pure sample of events with well-identified leptons and uses these leptons to determine the trigger efficiency. For this analysis, a sample of Z events is selected from the full dataset using the following cuts:

- Two opposite sign leptons passing selection criteria as described in Section 7.1. For the muon channel, the p_T cut on the probe muon is lowered to $p_T(ME) > 10$ GeV. $p_T(ME)$ refers to the transverse momentum as measured by the muon spectrometer and extrapolated back to the interaction point taking into account the energy loss due to multiple scattering inside the calorimeter.
- $|M_{ll} - M_Z| < 12, 20$ GeV for electrons and muons respectively

A comparison of the number of Z events seen in data using these cuts and the number expected from MC is shown in Figure 3 for the ee channel and shows good agreement. There is a slight discrepancy in the shapes between data and MC since no electron smearing is applied. However, as the overall agreement in the number of events seen in data and MC is good, this is expected to have only a small effect on the determination of the trigger efficiencies.

Matching is performed between each lepton and the trigger RoI to determine if it was that particular lepton which fired the trigger. Leptons are considered matched if the ΔR between the trigger RoI and the offline lepton object, defined as $\Delta R = \sqrt{(\Delta\eta^2 + \Delta\phi^2)}$, satisfies the criteria shown in Table 7.

The values for the ΔR matching were chosen to ensure that all of the leptons which truly arise from Z decays and fire the trigger are correctly counted as matching. This can be seen by looking at the ΔR distributions for data and MC at each of the trigger levels in Figure 4 for electrons which show that the distributions have fallen off well before the ΔR cut values. A similar result is seen in the muon channel

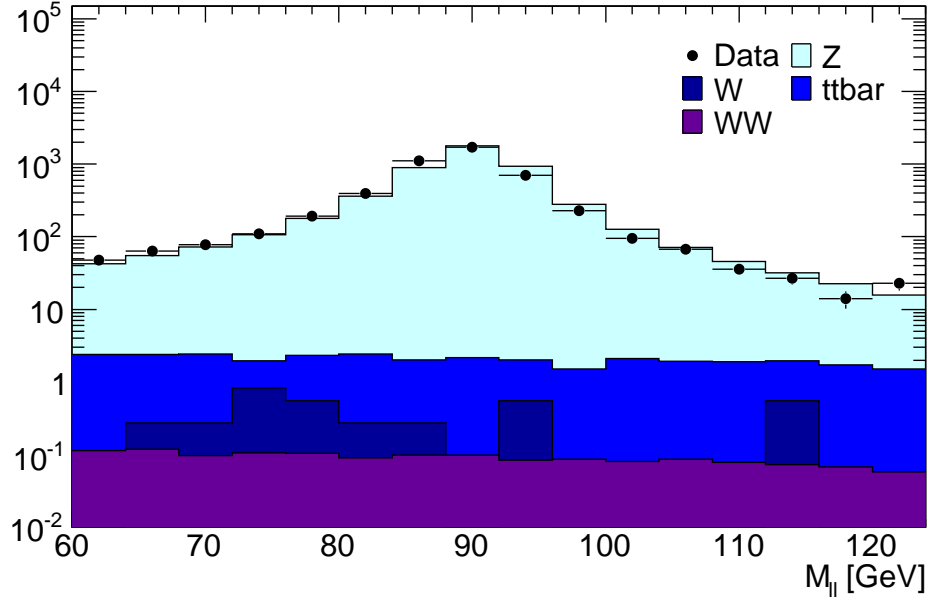


Figure 3: Di-electron invariant mass around the Z peak for data and MC with no electron smearing applied.

| Trigger level | ΔR cut | |
|---------------|----------------|-------|
| | Electrons | Muons |
| L1 | 0.15 | 0.40 |
| L2 | 0.05 | 0.20 |
| EF | 0.05 | 0.20 |

Table 7: Table showing the cut values used for ΔR matching between leptons and trigger RoIs. Leptons are considered matched to an ROI if the ΔR between the offline object and the trigger ROI is less than the cut value indicated above.

If a lepton matches the trigger ROI and the event satisfies the above criteria, it is considered a ‘tag’ lepton. The other lepton is then identified as the ‘probe’ and the trigger efficiency is defined as:

$$\epsilon = \frac{N_{\text{probes}}^{\text{matched}}}{N_{\text{probes}}}. \quad (3)$$

This means that for each event there are two possible tag leptons. This method can be applied to both data and MC and a comparison is performed in the next section.

5.2 Muon trigger efficiency

For the $\mu\mu$ and $e\mu$ analysis, a set of single muon triggers is used. An OR is performed between the muon and electron triggers in the $e\mu$ channel. The trigger used is L1_MU10 for periods A-E3, EF_mu10_MG for periods E4-G1, EF_mu13_MG for periods G2-I1 (up to run 167576) and EF_mu13_MG_tight for I1 (from run 167607)-I2. Both the L1_MU10 and EF_mu10_MG triggers are used in MC. The fraction of L1_MU10 trigger used is the integrated luminosity ratio between periods A-E3 and A-I2.

During the initial data taking period the muon trigger timing was still being tuned, thus the muon trigger signals were stretched to have an acceptance of 3 BC (bunch crossings) for a L1 trigger signal ($-3 \text{ BC} < T_{L1_MU} - T_{MBTS} < 1 \text{ BC}$). Those events with a positive BC difference were not collected by the data acquisition system. The fraction of triggers coming at the correct bunch crossing is 86% (95%) for RPC (TGC) in the first trigger period and almost 100% for both RPC and TGC in the other trigger periods. This fraction is displayed for the first trigger period for the RPC and TGC in Figure 5.

5.2.1 Comparison of data and MC trigger efficiencies

The muon trigger efficiency is measured using the tag and probe method on $Z/\gamma^* \rightarrow \mu\mu$ events. Both muons are required to pass the default offline muon selection cuts as described in Section 7, except the p_T cut on the probe muon is lowered to 10 GeV in order to observe the trigger turn-on curve. The tag muon must additionally pass a combination of MS-only, combined (CB) and MG (Muon-Girl algorithm) muon triggers. This combination is used in order to gain more statistics. The invariant mass of the di-muon system must be within the Z mass window ($|M_{\mu\mu} - M_Z| < 20 \text{ GeV}$) to make sure the probe muon is a real muon from Z decays. Both muons are also required to be separated in ϕ , with $\Delta\phi > \pi/2$, and come from the same primary vertex, with $|\Delta d_0(\mu\mu)| < 0.2 \text{ mm}$ and $|\Delta z_0(\mu\mu)| < 1 \text{ mm}$.

Figures 6 and 7 show the single muon trigger efficiency in data as a function of muon p_T for four trigger periods in the barrel and endcap regions. The trigger efficiency reaches the plateau region for $p_T > 20 \text{ GeV}$ within the statistical uncertainty. The L1_MU10 trigger efficiency in MC is found to be $(79.13 \pm 0.10)\%$ in barrel and $(95.19 \pm 0.05)\%$ in endcap respectively, and the EF_mu10_MG trigger efficiency is found to be $(78.18 \pm 0.10)\%$ in barrel and $(91.91 \pm 0.06)\%$ in endcap respectively. The luminosity weighted average trigger efficiency is $(78.20 \pm 0.10)\%$ in barrel and $(91.98 \pm 0.06)\%$ in endcap.

The average muon trigger efficiency is calculated by taking into account the integrated luminosity in different trigger periods. The efficiency as a function of offline muon p_T , η and ϕ for data and MC are shown in Fig. 8 to 10. We use 14 η bins (-1.05, -0.908, -0.791, -0.652, -0.476, -0.324, -0.132, 0, 0.132, 0.324, 0.476, 0.652, 0.791, 0.908, 1.05) and 16 ϕ bins (from $-15/16\pi$ to $17/16\pi$) for the RPC. We use 4 η bins (-2.4, -1.95, -1.05, 1.05, 1.95, 2.4)¹ and 8 ϕ bins (from $-13/12\pi$ to $11/12\pi$) for the TGC. The choices of binnings are determined by the geometry of the RPC and TGC detectors.

Table 8 shows the trigger efficiencies for muons with $p_T > 20 \text{ GeV}$ for four trigger periods together with the average trigger efficiency and data/MC scale factor. The luminosity-weighted trigger efficiency is $(77.1 \pm 0.4)\%$ for the barrel and $(93.4 \pm 0.2)\%$ for the endcap. The data/MC scale factor is 0.986 ± 0.005 for the barrel and is 1.016 ± 0.003 for the endcap with statistical errors only. Systematic errors are discussed in the following section.

5.2.2 Systematic uncertainties on the trigger scale factor

To estimate the systematic uncertainty on the scale factor, the following sources are considered:

- (1) The matching cone size for the offline muon and online trigger objects is varied. The default cone size used is 0.4 (0.2) for L1 (HLT), and the studies are repeated using a cone size of 0.3 (0.1) for L1 (HLT) and also 0.5 (0.3) for L1 (HLT). The scale factor changes by 0.0005 (0.0043) for barrel (endcap).
- (2) The η -dependence of the data/MC scale factor is checked. The error on the scale factor is 0.0044 (0.0025) for the barrel (endcap) across the whole η range when a fit is performed to the scale factor.
- (3) The number of same sign events is used to estimate the QCD background. The resulting variation on the scale factor is less than 0.0001.

¹Only two bins in each of the endcaps are used. The bin between -1.05 and 1.05 is not used

| Period | RPC efficiency | TGC efficiency |
|-----------------------------|----------------|----------------|
| A-E3 | (78.3 ± 2.7)% | (84.8 ± 2.5)% |
| E4-G1 | (74.5 ± 1.4)% | (94.9 ± 0.8)% |
| G2-167576 | (78.1 ± 0.6)% | (94.8 ± 0.3)% |
| 167607-I2 | (77.0 ± 0.6)% | (92.5 ± 0.4)% |
| Luminosity-weighted average | (77.3 ± 0.4)% | (93.6 ± 0.2)% |
| MC | (78.2 ± 0.1)% | (92.0 ± 0.1)% |
| Ratio | 0.986 ± 0.005 | 1.016 ± 0.003 |

Table 8: Trigger efficiencies for muons with $p_T > 20$ GeV for four trigger periods, together with the average trigger efficiencies and data/MC scale factors. Only statistical uncertainties are included.

- (4) The size of the mass window is varied ($\pm 15, \pm 20$ GeV) and the scale factor is found to change by 0.0020 (0.0006) for the barrel (endcap).

The final data/MC scale factor including systematic errors is found to be 0.986 ± 0.007 (1.016 ± 0.006) for the barrel (endcap).

Studies about the muon RPC and TGC trigger efficiencies can also be found at [10], similar results and systematics are obtained. Even though the actual trigger efficiency depends on the muon η , the efficiency η dependence is simulated well in MC and the data/MC scale factor is consistent with a constant number within 0.3%.

5.3 Electron trigger efficiency

The triggers used in data and MC for events containing electrons in the final state are:

- Periods A-E3: L1_EM14
- Periods E4-I2: EF_e15_medium

As described earlier, an OR is made between the electron and muon triggers for the $e\mu$ channel.

5.3.1 Comparison of data and MC trigger efficiencies

In order to evaluate the scale factor it is necessary to calculate the trigger efficiency using the tag and probe method on both data and MC. This is calculated for each trigger separately and then a luminosity weighted average is taken. The same method is used for the calculation of the scale factor.

To determine if the scale factor shows any dependence on the electron kinematics, it is useful to compare the distributions of some kinematic variables for the probe electrons in data and MC. Figure 11 shows good agreement between data and $Z \rightarrow ee$ MC for probe p_T , η and ϕ . The difference between MC and data remains approximately constant as a function of these kinematic variables, indicating that the scale factor is roughly independent of p_T , η and ϕ . This allows a constant scale factor to be defined, which differs from the muon case in which a different scale factor is required for the barrel and endcap regions.

The trigger efficiencies in data and MC are also compared as a function of p_T , η and ϕ for the full dataset. All these distributions, shown in Figure 12, demonstrate the remarkably good agreement between the data and MC, as well as the consistently high efficiency of these triggers.

5.3.2 Scale factor calculation

A comparison between the triggers used in data and MC and the corresponding single electron scale factor is made in Table 9. The luminosity-weighted efficiency of the triggers in MC is $0.991 \pm 0.00008(\text{stat})$. For data, the efficiency is $0.990 \pm 0.001(\text{stat})$, giving a scale factor of $0.999 \pm 0.001(\text{stat})$. This suggests that the MC models the data very well. These efficiencies are quoted with statistical errors only; a discussion of systematic errors is given in the following section.

| Trigger | Data efficiency | Scale factor |
|---------------|---------------------------|---------------------------|
| L1_EM14 | $0.990^{+0.006}_{-0.009}$ | $0.999^{+0.006}_{-0.009}$ |
| EF_e15_medium | 0.990 ± 0.001 | 0.999 ± 0.001 |
| Combined | 0.990 ± 0.001 | 0.999 ± 0.001 |

Table 9: Trigger efficiencies and single electron scale factors with statistical uncertainties only for electron triggers used in data.

5.3.3 Systematic uncertainties on trigger scale factor

There are several sources of systematic uncertainty which should be considered when evaluating the scale factor. These sources include the effect of varying the cut on $|M_{ll} - M_Z|$ which may result in a sample of Z events with different level of background and may affect the trigger efficiencies and hence the scale factor. Similarly, the electrons used are required to be isolated so that the sample is free from fake electrons which may not pass isolation criteria. Thus, the effect of using this isolation requirement is included as a source of systematic uncertainty. The scale factor has been calculated using the ratio of data to $Z \rightarrow ee$ MC, however there is expected to be some small contamination from background events in data. Figure 3 shows that this contamination is small but it should still be included as a source of systematic uncertainty and is done so by calculating the change in the scale factor when all the background samples, correctly weighted, are used instead of just the $Z \rightarrow ee$ sample. A further source of systematic uncertainty comes from the assumption that the scale factor is constant as a function of η . To study this, a fit to the scale factor expressed as a function of η is performed and the error on the fit is taken as the systematic uncertainty arising from any η -dependence of the scale factor.

| Uncertainty | SF | $\Delta\text{SF} (\times 10^{-4})$ |
|-----------------------------------|--------|------------------------------------|
| Original | 0.9985 | - |
| $ M_{ll} - M_Z < 10 \text{ GeV}$ | 0.9989 | -3.7 |
| $ M_{ll} - M_Z < 15 \text{ GeV}$ | 0.9985 | +0.10 |
| Unisolated electrons | 0.9985 | +0.27 |
| Background contamination | 0.9985 | -0.53 |
| η -dependence (upper) | 0.9987 | +2.0 |
| η -dependence (lower) | 0.9983 | -2.0 |

Table 10: Systematic uncertainties on scale factor

These uncertainties are summarised in Table 10. When added in quadrature with the statistical uncertainty for the full dataset, the resulting scale factor is calculated to be $\text{SF} = 0.999 \pm 0.001(\text{stat}) \pm 0.0004(\text{syst}) = 0.999 \pm 0.001(\text{stat+syst})$.

5.3.4 Comparison with egamma group recommendation

The trigger simulation in MC was done using a different menu from that used during data-taking. Therefore, the egamma group recommends that trigger efficiencies should be taken from data only, with a $99 \pm 1\%$ efficiency. The 1% uncertainty will be taken as the systematic uncertainty for electron trigger efficiency calculation. Since the trigger efficiencies in data and MC are calculated to be $99 \pm 0.1\%$ and $99.1 \pm 0.008\%$ respectively, giving a data/MC scale factor of 1 for dilepton events, the results described here are entirely equivalent to those using the official egamma group recommendation.

5.4 Event-based scale factor calculation

The di-leptonic channel is used for this W^+W^- analysis, therefore there are two chances to pass a single-lepton trigger. It is necessary to define an event-based scale factor which is dependent on the lepton-based scale factor calculated above. Assuming a constant scale factor, the event-based scale factor for l_1, l_2 events, where $l = e, \mu$, is defined as:

$$SF_{l_1, l_2} = \frac{1 - [1 - \epsilon_{l_1}(Z, data)][1 - \epsilon_{l_2}(Z, data)]}{1 - [1 - \epsilon_{l_1}(Z, MC)][1 - \epsilon_{l_2}(Z, MC)]} \quad (4)$$

This may be rearranged to give:

$$SF_{l_1, l_2} = \frac{1 - [1 - \epsilon_{l_1}(Z, MC) \times SF_{l_1}][1 - \epsilon_{l_2}(Z, MC) \times SF_{l_2}]}{1 - [1 - \epsilon_{l_1}(Z, MC)][1 - \epsilon_{l_2}(Z, MC)]} \quad (5)$$

There are 6 possible W^+W^- final states: ee , $\mu\mu$ (barrel-barrel), $\mu\mu$ (endcap-endcap), $\mu\mu$ (barrel-endcap), $e\mu$ (barrel) and $e\mu$ (endcap) where barrel and endcap denote where the muon lies in the detector. Using the above equation 5, the event-based scale factors can be calculated for each different scenario separately. These results are shown in Table 11.

| Channel | SF | Error on SF |
|--------------------------|------|-------------|
| ee | 1.00 | 0.0002 |
| $\mu\mu$ (barrel-barrel) | 0.99 | 0.001 |
| $\mu\mu$ (endcap-endcap) | 1.00 | 0.0002 |
| $\mu\mu$ (barrel-endcap) | 1.00 | 0.0006 |
| $e\mu$ (barrel) | 1.00 | 0.0002 |
| $e\mu$ (endcap) | 1.00 | 0.00007 |

Table 11: Event-based scale factors with errors

Using the expected proportion of $\mu\mu$ events which have both muons in the barrel, both in the endcap and one in each region from W^+W^- MC, a weighted $\mu\mu$ event-based scale factor can be calculated. This method is also used to determine the average $e\mu$ event-based scale factor and Table 12 summarises the overall scale factors and their associated errors for each channel: ee , $\mu\mu$ and $e\mu$.

| Channel | SF | Error on SF |
|----------|------|-------------|
| ee | 1.00 | 0.0002 |
| $\mu\mu$ | 1.00 | 0.0004 |
| $e\mu$ | 1.00 | 0.0002 |

Table 12: Event-based scale factors averaged over all regions with errors

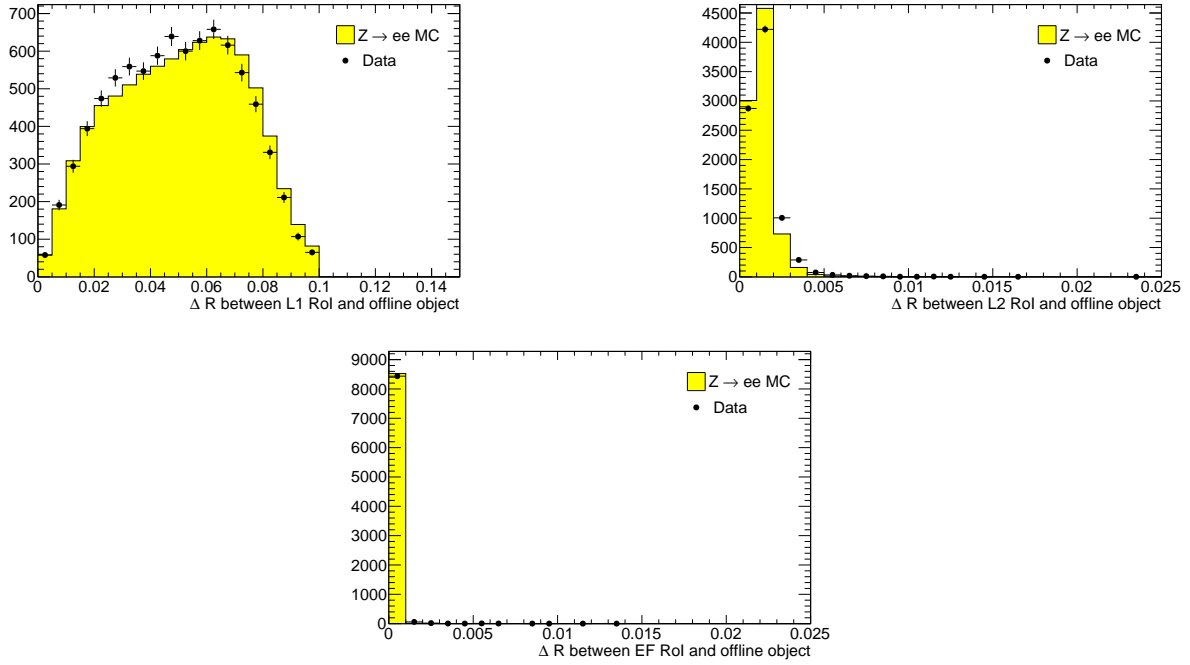


Figure 4: Distributions of ΔR between trigger ROI and offline electrons for RoIs calculated at L1, L2 and EF.

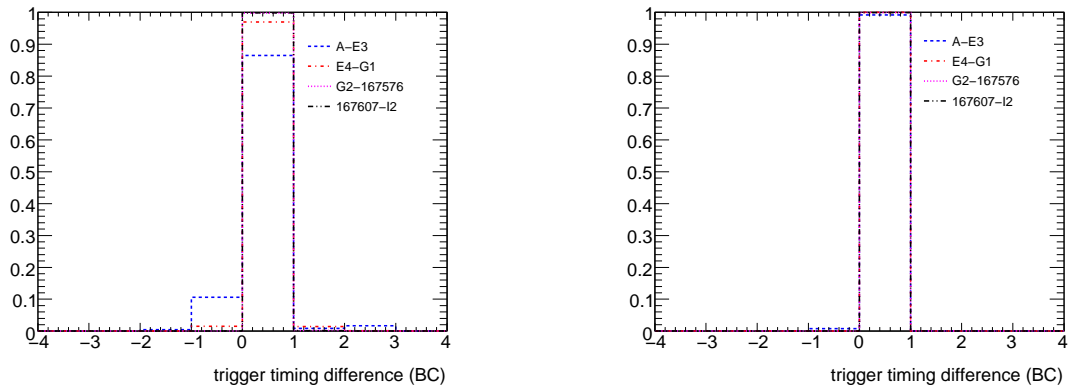


Figure 5: Muon trigger timing difference as a function of bunch crossings (BC) for the RPC (left) and TGC (right) for all data periods with all distributions scaled to unity.

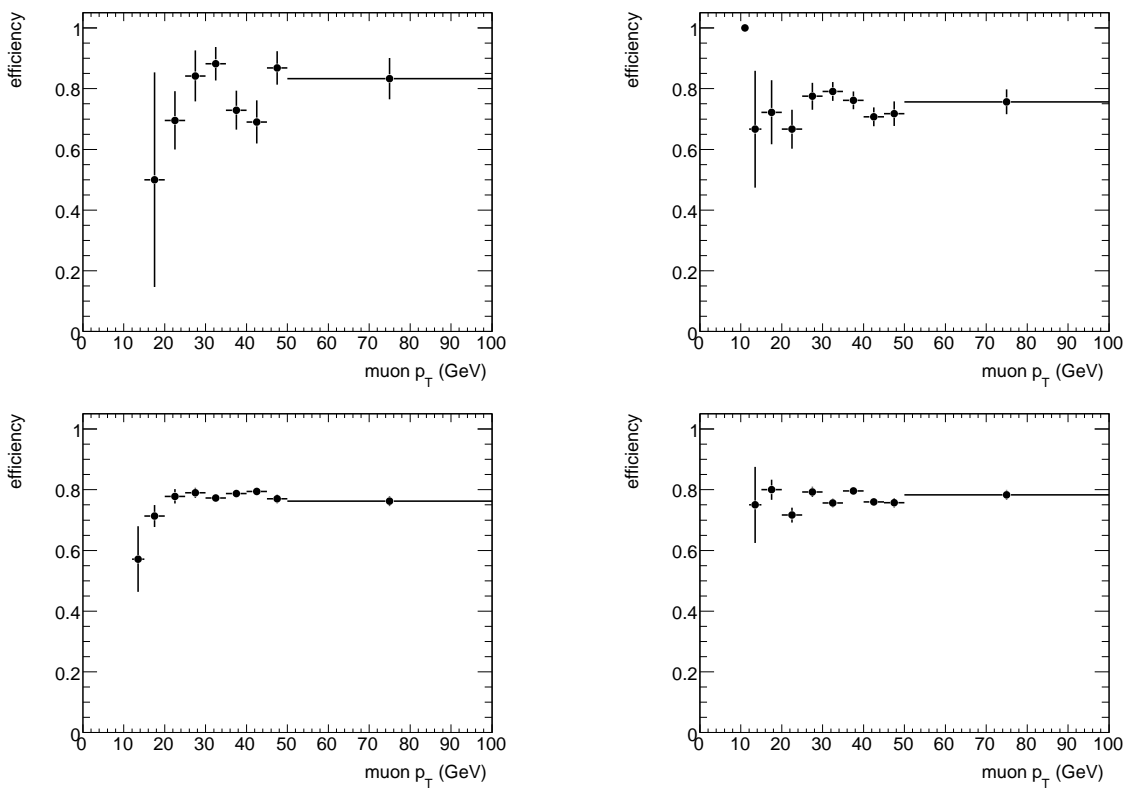


Figure 6: Muon trigger efficiency as a function of muon p_T in the barrel region for four trigger periods: top left for A to E3; top right for E4 to G1; bottom left for G2 to H1 (run 167576) and bottom right for H1 (run 167607) to I2.

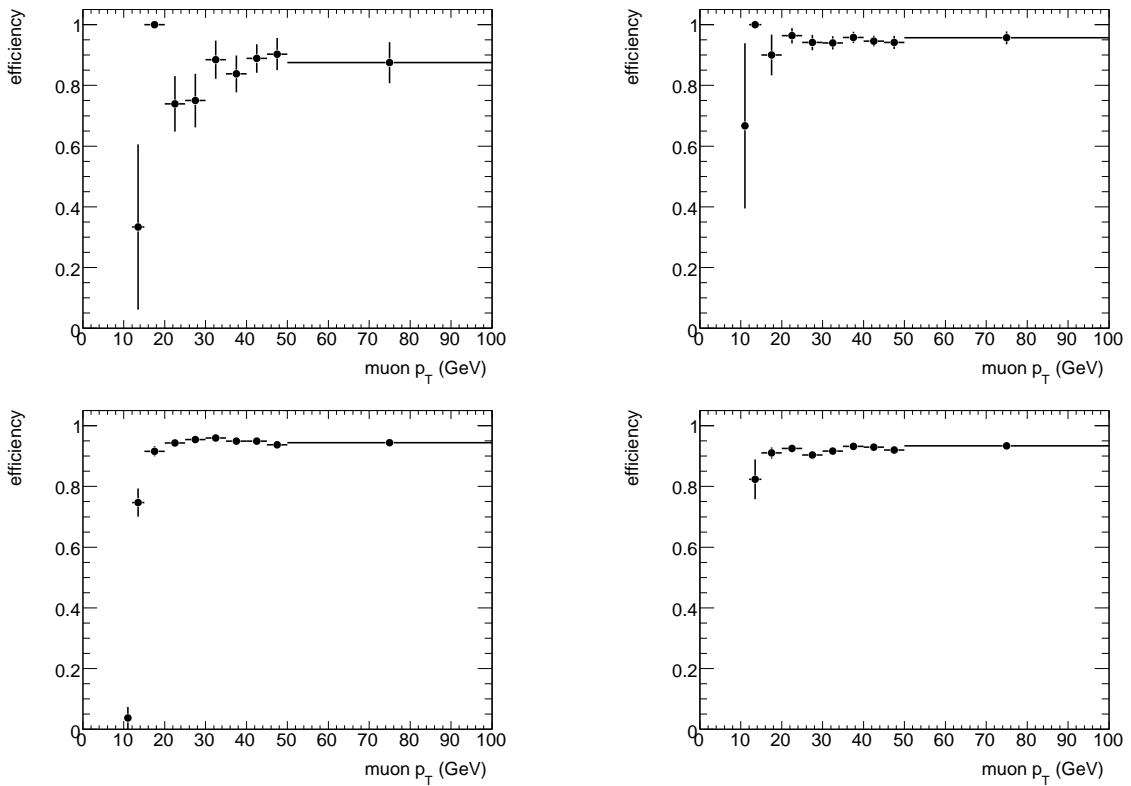


Figure 7: Muon trigger efficiency as a function of muon p_T in the endcap region for four trigger periods: top left for A to E3; top right for E4 to G1; bottom left for G2 to H1 run 167576 and bottom right for H1 run 167607 to I2

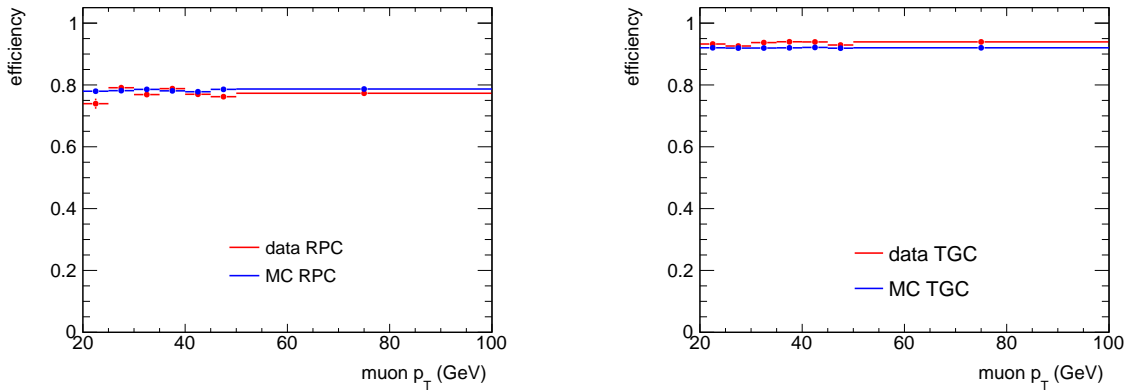


Figure 8: Data and MC comparison for average muon trigger efficiencies as a function of muon p_T for the barrel (left plot) and endcap (right plot) regions. HLT triggers are used in data while only L1_MU10 is used in MC. The relevant region for the W^+W^- analysis is for muons with $p_T > 20$ GeV.

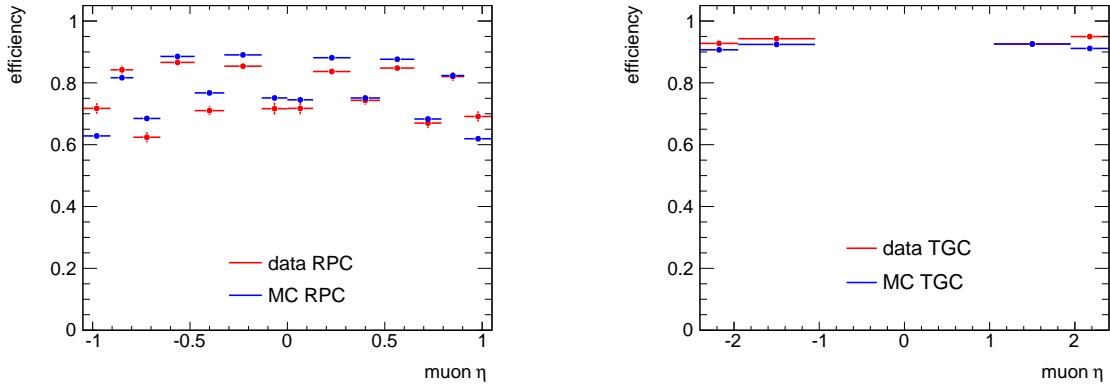


Figure 9: Data and MC comparison for average muon trigger efficiencies as a function of muon η for the barrel (left plot) and endcap (right plot) regions. Only probe muons with $p_T > 20$ GeV are used.

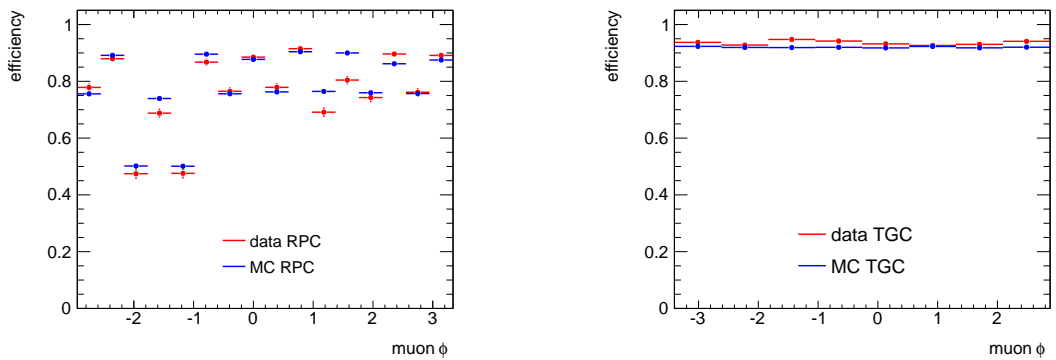


Figure 10: Data and MC comparison for average muon trigger efficiencies as a function of muon ϕ in the barrel (left plot) and endcap (right plot) regions. Only probe muons with $p_T > 20$ GeV are used.

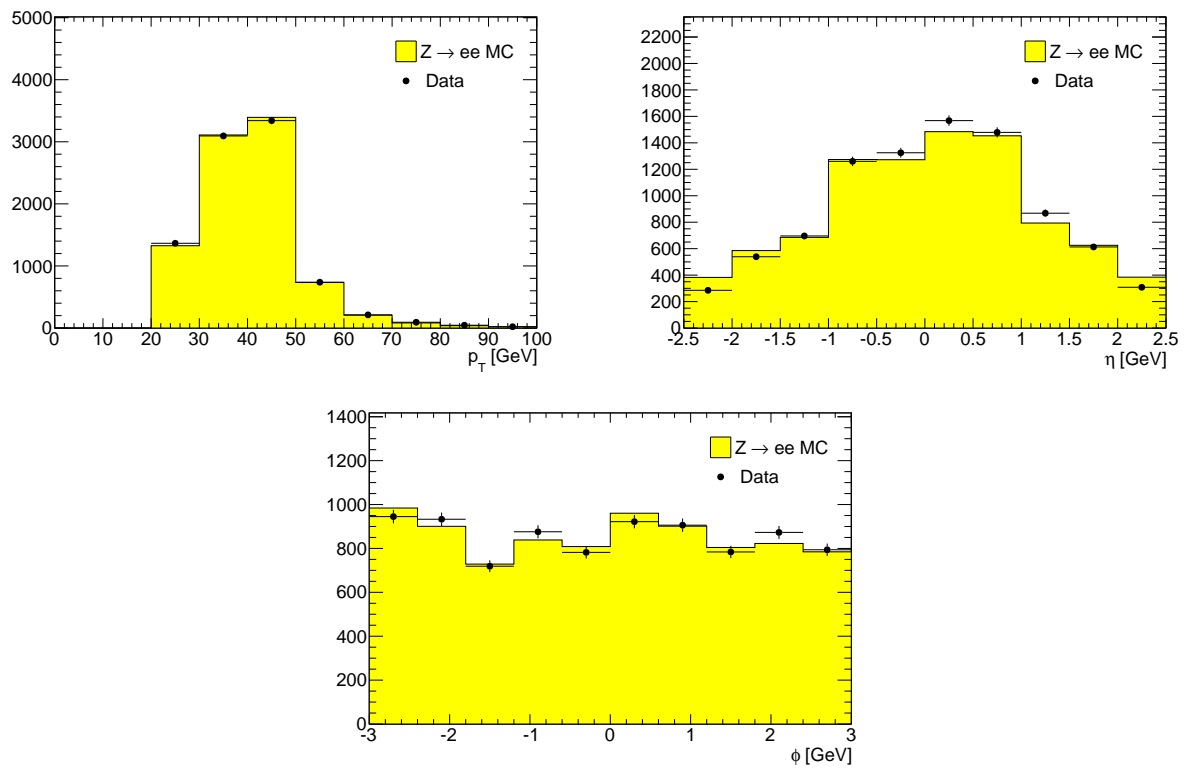


Figure 11: Distributions of p_T , η and ϕ for probe electrons in data and $Z \rightarrow ee$ MC.

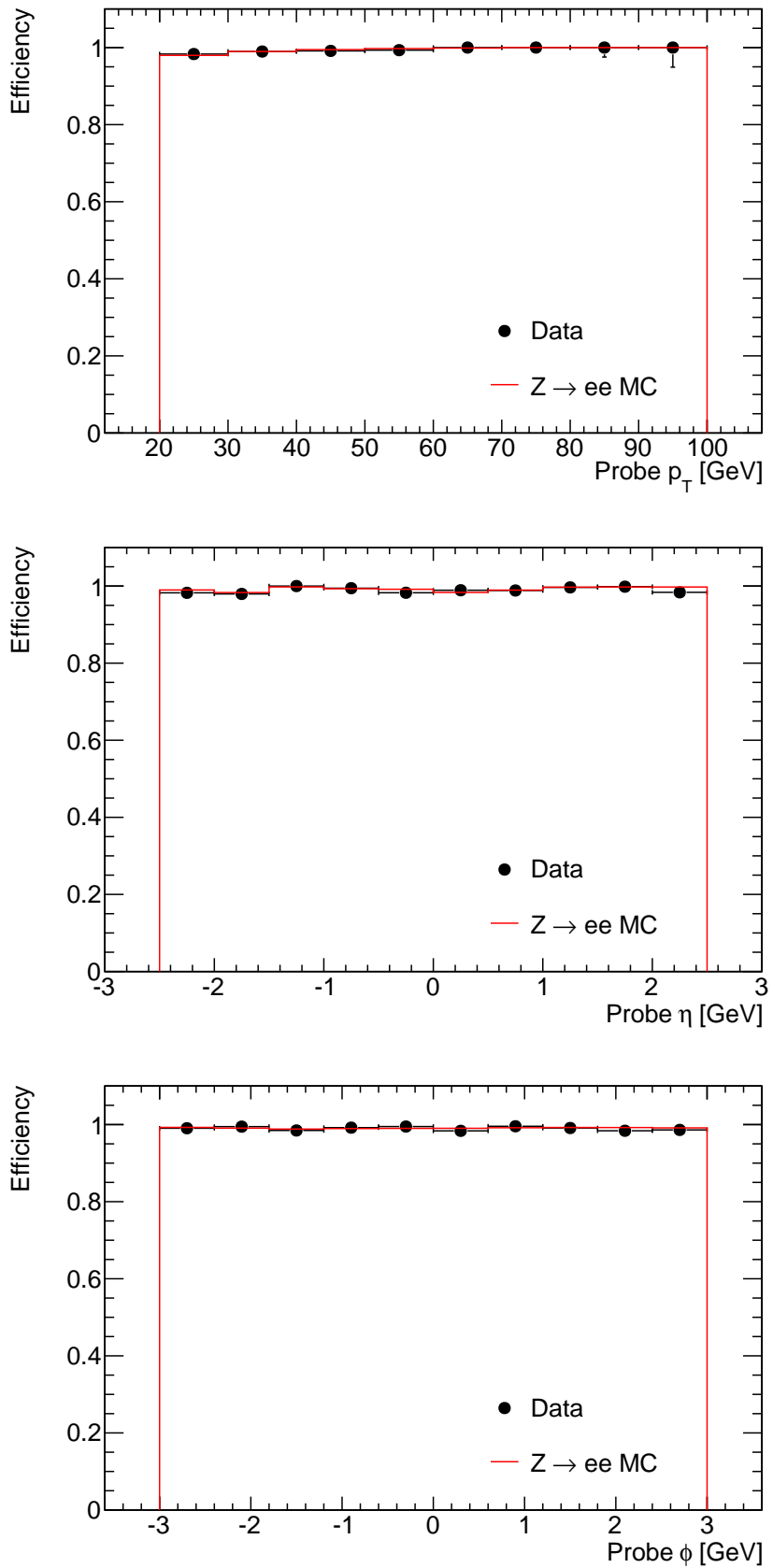


Figure 12: Trigger efficiency as a function of p_T , η and ϕ for probe electrons in data and $Z \rightarrow ee$ MC.

6 Physics object reconstruction and identification

The ATLAS detector and its performance is described in detail elsewhere [11]. A brief description of the physics objects used in this W^+W^- analysis is given below. The major physics objects used for the W^+W^- analysis are electrons, muons, missing transverse energy (E_T^{miss}), and hadronic jets. In addition, lepton trigger objects and event production vertices are also used in this analysis.

6.1 Electron identification and efficiencies

Electrons are reconstructed as energy deposits in the calorimeter, matched to tracks found in the inner detector. Further identification criteria are applied to reject background. The electron selection used in this analysis is listed in Table 13. The identification criteria RobusterTight [12], is a reference set of electron selection requirements that is based on shower shape, track quality, detection of transition radiation, and track-to-calorimeter-cluster matching. The isolation requirement is on the sum of calorimeter energy in a cone of 0.3 around the electron and excludes the energy in the electron cluster.

| Electron Selection |
|--|
| Reconstructed Electron Candidate |
| Geometrical Acceptance: $ \eta < 2.5$, outside crack region |
| Object Quality: Outside regions w/LAr readout problems |
| Kinematic Acceptance: $E_T > 20\text{GeV}$ |
| Identification Criteria: RobusterTight |
| Isolation Requirement: $\sum_{\Delta R < 0.3} E_T(i) < 6\text{ GeV}$ |
| Transverse Impact parameter requirement: $\frac{d_0}{\sigma_{d_0}} < 10$ |
| Longitudinal Impact parameter requirement: $ z_0 < 10\text{mm}$ |

Table 13: Electron Definition

The electron ID efficiency is determined from data using the *tag-and-probe* method on $Z \rightarrow e^+e^-$ and $W \rightarrow ev$ events. The total electron efficiency has been calculated in eight bins in η , and the MC scale factors are given in Tables 14 and 15. The combined electron efficiency is composed of three terms. The first is the efficiency to reconstruct the electron. This has been measured to be $97 \pm 1.5\%$ [13], and is found to be in agreement with the MC prediction. The second is the efficiency of a reconstructed electron to pass the RobusterTight electron identification criteria. The third term is the efficiency of a RobusterTight electron to pass the additional isolation and impact parameter requirements used in this analysis. The determination of the first two terms is not unique to this analysis and will not be presented here. The determination of the final term is specific to W^+W^- electron definition and is presented in the following section. The combined electron efficiencies in W^+W^- events are provided in Tables 14 and 15.

| η bin | [-2.47,-2.01] | [-2.01,-1.52] | [-1.37,-0.8] | [-0.8,0] |
|------------------------------|-------------------|-------------------|-------------------|-------------------|
| Scale Factor | 0.910 ± 0.039 | 0.988 ± 0.032 | 0.986 ± 0.029 | 0.975 ± 0.027 |
| $\epsilon_{\text{combined}}$ | 0.638 ± 0.035 | 0.665 ± 0.036 | 0.715 ± 0.033 | 0.771 ± 0.031 |

Table 14: Combined electron identification scale factors and electron efficiencies for $-2.47 < \eta < 0$.

In addition to the η -dependence of the scale factors presented in Tables 14 and 15, an E_T -dependence has been observed from the efficiency measurement using the tag and probe method with W bosons. For the current analysis, the decision was made to leave the central value of the scale factors uncorrected, and

| η bin | [0,0.8] | [0.8,1.37] | [1.52,2.01] | [2.01,2.47] |
|-----------------------|-------------------|-------------------|-------------------|-------------------|
| Scale Factor | 0.982 ± 0.027 | 1.024 ± 0.033 | 1.020 ± 0.050 | 0.916 ± 0.039 |
| $\epsilon_{combined}$ | 0.784 ± 0.031 | 0.75 ± 0.037 | 0.685 ± 0.053 | 0.643 ± 0.043 |

Table 15: Combined electron identification scale factors and electron efficiencies for $0 < \eta < 2.47$.

assign a larger, E_T -dependent, uncertainty to the scale factor. In accordance with the recommendation by the e/ γ combined performance group, these additional uncertainties are taken to be the difference in E_T -dependent scale factor from unity plus the uncertainty associated to the E_T -dependent scale factor. These additional uncertainties are provided in Table 16. The added uncertainty in the W^+W^- acceptance has been calculated using the W^+W^- MC, and found to be 6.0% ee-channel and 3.4% in the e μ -channel.

| E_T bin [GeV] | [20,25] | [25,30] | [30,35] | [35,40] | [40,45] | above 45 |
|------------------------|---------|---------|---------|---------|---------|----------|
| Additional Uncertainty | 0.16 | 0.05 | 0.01 | 0.01 | 0.01 | 0.03 |

Table 16: Additional electron efficiency scale factor uncertainties which account for E_T -dependence.

6.1.1 Determination of the Isolation and Impact Parameter Requirement Efficiencies

The efficiency of the isolation and impact parameter requirements was determined from data using the *tag-and-probe* method on selected $Z \rightarrow e^+e^-$ events. Tag electrons were selected by requiring basic acceptance and RobusterTight electron identification. Probe electrons were then selected by requiring basic acceptance and that they combine with a tag electron to form an invariant mass within 10 GeV of the Z mass. The efficiency of the isolation and impact parameter requirements with respect to RobusterTight electron identification, was then calculated as:

$$\epsilon_{Iso+d_0+z_0} = \frac{N_{probes}(W^+W^- Selection)}{N_{probes}(\text{RobusterTight})}, \quad (6)$$

where: $N_{probes}(W^+W^- Selection)$ is the number of probes passing the full W^+W^- electron selection, including the isolation and the d_0 and z_0 impact parameter requirements, and $N_{probes}(\text{RobusterTight})$ is the number of probes passing RobusterTight. This efficiency calculation was performed both in data and $Z \rightarrow e^+e^-$ MC, and using the same η bins used to determine the RobusterTight ID efficiencies. The results are presented in Tables 17 and 18.

| η bin | [-2.47,-2.01] | [-2.01,-1.52] | [-1.37,-0.8] | [-0.8,0] |
|---------------------------------|-------------------|-------------------|-------------------|-------------------|
| $\epsilon_{Iso+d_0+z_0}$ (Data) | 0.966 ± 0.008 | 0.954 ± 0.008 | 0.951 ± 0.006 | 0.966 ± 0.004 |
| $\epsilon_{Iso+d_0+z_0}$ (MC) | 0.982 ± 0.001 | 0.96 ± 0.001 | 0.97 ± 0.001 | 0.972 ± 0.001 |
| Scale Factor | 0.984 ± 0.009 | 0.993 ± 0.009 | 0.98 ± 0.006 | 0.993 ± 0.004 |

Table 17: Isolation and Impact Parameter Significance Efficiency Calculation for $-2.47 < \eta < 0$

The isolation and impact parameter significance efficiencies described here are combined with the electron reconstruction and RobusterTight ID efficiencies to give the total electron ID efficiencies for the W^+W^- selection. A systematic uncertainty of 2%, independent of η , has been included in the combined scale factors as per recommendation of the e/γ performance group. This two percent appears as an

| η bin | [0,0.8] | [0.8,1.37] | [1.52,2.01] | [2.01,2.47] |
|---------------------------------|-------------|-------------|-------------|-------------|
| $\epsilon_{Iso+d_0+z_0}$ (Data) | 0.967±0.004 | 0.96±0.005 | 0.953±0.008 | 0.963±0.009 |
| $\epsilon_{Iso+d_0+z_0}$ (MC) | 0.971±0.001 | 0.969±0.001 | 0.961±0.001 | 0.983±0.001 |
| Scale Factor | 0.995±0.004 | 0.991±0.005 | 0.992±0.008 | 0.979±0.009 |

Table 18: Isolation and Impact Parameter Significance Efficiency Calculation for $0 < \eta < 2.47$

intrinsic systematic uncertainty on the *tag and probe* method as applied to data and covers any systematic associated to background contamination. These combined efficiencies are presented in Tables 14 and 15.

For completeness the efficiencies and scale factors of the intermediate steps are given in Tables 19 to 22. Tables 19 and 20 show the isolation efficiency and scale factors with respect to the RobusterTight requirement.

| η bin | [-2.47,-2.01] | [-2.01,-1.52] | [-1.37,-0.8] | [-0.8,0] |
|-------------------------|---------------|---------------|--------------|-------------|
| ϵ_{Iso} (Data) | 0.97±0.008 | 0.958±0.008 | 0.959±0.006 | 0.986±0.003 |
| ϵ_{Iso} (MC) | 0.984±0.001 | 0.965±0.001 | 0.977±0.001 | 0.988±0.0 |
| Scale Factor | 0.986±0.008 | 0.993±0.008 | 0.981±0.006 | 0.998±0.003 |

Table 19: Isolation Efficiency Calculation for $-2.47 < \eta < 0$

| η bin | [0,0.8] | [0.8,1.37] | [1.52,2.01] | [2.01,2.47] |
|-------------------------|-------------|-------------|-------------|-------------|
| ϵ_{Iso} (Data) | 0.986±0.002 | 0.97±0.004 | 0.959±0.007 | 0.965±0.009 |
| ϵ_{Iso} (MC) | 0.988±0.0 | 0.976±0.001 | 0.966±0.001 | 0.985±0.001 |
| Scale Factor | 0.999±0.002 | 0.994±0.005 | 0.993±0.008 | 0.979±0.009 |

Table 20: Isolation Efficiency Calculation for $0 < \eta < 2.47$

Tables 21 and 22 show the d_0 efficiency and scale factors with respect to the RobusterTight and isolation requirements.

6.1.2 Electron Energy Calibration and Oversmearing

We use the electron energy scale correction in data as recommended by the e/γ performance group and documented in [14]. The corresponding reduced energy scale uncertainties (1% in the barrel and 3% in the endcap) are propagated through the analysis as systematics. The energy resolution uncertainties are used as well to assess the related systematic uncertainty by oversmearing the Monte Carlo accordingly.

6.2 Muon identification and efficiencies

Muons are reconstructed using information from the outer muon spectrometer (MDT and CSC precision tracking chambers and trigger chambers for the barrel (RPC) and for the endcaps (TGC)), the inner tracking detectors and the calorimeters. Muons are identified with a tracking algorithm that associates a track found in the muon spectrometer with a corresponding inner detector track, after the former is corrected for energy loss in the calorimeter. The combined muon detection rapidity coverage is $|\eta| < 2.5$. The candidate muons are required to be isolated in the inner tracker to minimize the contributions of muons originating from hadronic jets.

| η bin | [-2.47,-2.01] | [-2.01,-1.52] | [-1.37,-0.8] | [-0.8,0] |
|-----------------------------|---------------|---------------|--------------|-------------|
| ϵ_{Iso+d_0} (Data) | 0.966±0.008 | 0.954±0.008 | 0.951±0.006 | 0.966±0.004 |
| ϵ_{Iso+d_0} (MC) | 0.982±0.001 | 0.96±0.001 | 0.97±0.001 | 0.973±0.001 |
| Scale Factor | 0.984±0.009 | 0.993±0.009 | 0.98±0.006 | 0.993±0.004 |

Table 21: d_0 Efficiency Calculation for $-2.47 < \eta < 0$

| η bin | [0,0.8] | [0.8,1.37] | [1.52,2.01] | [2.01,2.47] |
|-----------------------------|-------------|-------------|-------------|-------------|
| ϵ_{Iso+d_0} (Data) | 0.967±0.004 | 0.96±0.005 | 0.953±0.008 | 0.963±0.009 |
| ϵ_{Iso+d_0} (MC) | 0.972±0.001 | 0.969±0.001 | 0.961±0.001 | 0.984±0.001 |
| Scale Factor | 0.995±0.004 | 0.991±0.005 | 0.992±0.008 | 0.979±0.009 |

Table 22: d_0 Efficiency Calculation for $0 < \eta < 2.47$

The muon reconstruction and identification efficiencies are determined by applying the *tag-and-probe* method on $Z/\gamma^* \rightarrow \mu\mu$ candidates in data as well as simulated $Z/\gamma^* \rightarrow \mu\mu$ MC events separately. The muon selection criteria are listed in Sect. 7. The efficiencies are determined for the following three categories:

- The *Combined* muon efficiency (ϵ_{CB}): the probability for an isolated probed muon track to match with a muon identified as a *combined muon*;
- Inner Detector muon efficiency (ϵ_{ID}): the probability for a *Muon Spectrometer* (MS) muon to match with an isolated track in the inner tracker which also satisfies the pixel, SCT and TRT hit requirements and $|p_T^{ID} - p_T^{MS}|/p_T^{ID} < 0.5$;
- Muon isolation efficiency (ϵ_{iso}): the probability for a *combined* muon to pass the tracker isolation requirement.

The data sample used in this study are from run period A to I2, and the MC samples used are PYTHIA $Z \rightarrow \mu^+\mu^-$ events processed with the GEANT4 simulation of the ATLAS detector and with pileup events included. The overall muon reconstruction and identification efficiency is the multiplication of ϵ_{CB} , ϵ_{ID} and ϵ_{iso} .

6.2.1 CB muon efficiency (ϵ_{CB})

For the CB muon efficiency measurement, the *tag muon* is required to be an isolated combined muon that passes all the *tight* selection requirements. The *probe muon* is an isolated track found in the inner tracker. The CB muon efficiency is defined as the probability for this isolated track to matched with a reconstructed combined muon.

The *tag muon* is a combined muon with $p_T > 20$ GeV, $|\eta| < 2.4$ and $|\Delta d_0| < 10$ mm. It is also required to be isolated in the inner tracker with $\text{ptcone20}/p_T < 0.1$ and have $|p_T^{ID} - p_T^{MS}|/p_T^{ID} < 0.5$. Furthermore, the ID track has the same pixel, SCT and TRT hit requirements as the muons used in the final event selection.

The *probe track* is an ID track with $p_T > 20$ GeV, $|\eta| < 2.4$, $|\Delta d_0| < 10$ mm and at least 10 TRT hits if $|\eta| < 1.96$. The crack region near $\eta = 0$ is removed by requiring $|\eta| > 0.005$. In addition, the track has to be isolated in the inner tracker with $\text{ptcone20}/p_T < 0.1$ and satisfy the pixel, SCT and TRT hit requirements. Different definitions and cut values of muon isolation are used to estimate the

systematic uncertainties. To further reduce the QCD backgrounds, the *probe track* is required to have opposite charge with the *tag muon* and the invariant mass of the *tag muon* and the *probe track* must be within the Z mass window $75 < M_{\mu+\text{track}} < 105$ GeV. The transverse momentum of the dimuon system should have $p_T(\mu + \text{track}) < 65$ GeV. The track and the *tag muon* are also required to be back-to-back in ϕ with $|\Delta\phi| > 2$. The probe track and the tag muon must come from the same primary vertex with $|\Delta d_0(\mu\mu)| < 0.1$ mm and $|\Delta z_0(\mu\mu)| < 2$ mm.

For each *probe track*, we search for all possible CB muons in the event. If a combined muon has $p_T > 10$ GeV, $|\eta| < 2.4$ and the distance between the *probe track* and the combined muon in $\eta - \phi$ space has $\Delta R = \sqrt{\Delta\eta^2 + \Delta\phi^2} < 0.01$, then the two objects are matched with each other. The CB muon efficiency as a function of muon p_T , η and ϕ are shown in Fig. 13. The matching efficiency is found to be $(93.2 \pm 0.17)\%$ in data and $(94.8 \pm 0.03)\%$ in MC.

To estimate the systematic uncertainties, we use different isolation definitions and also vary the isolation cut values for the *probe track*. As shown in Table 23 the measured efficiency for data varies by 0.3%. We also check the background fraction using the MC simulated samples. The amount of background is estimated to be 0.4% from $W + \text{jets}$, 0.5% from QCD dijet, 0.1% from $t\bar{t}$ and 0.3% from $W \rightarrow \mu\nu$ events. This has negligible effect on the efficiency measurement. Figure 14 shows the efficiency for four different run periods. We observe that the efficiency varies by 0.6%. The final data/MC scale factor for the combined muon efficiency is estimated to be $0.983 \pm 0.002(\text{stat}) \pm 0.007(\text{syst})$.

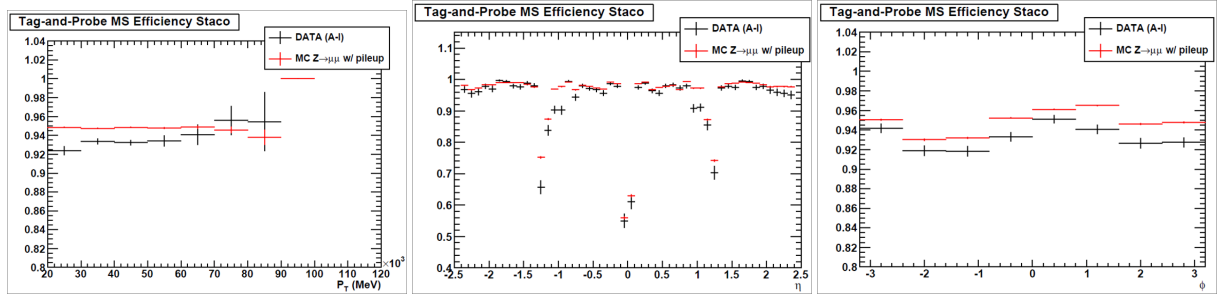


Figure 13: The CB muon efficiency as a function of muon p_T , η and ϕ .

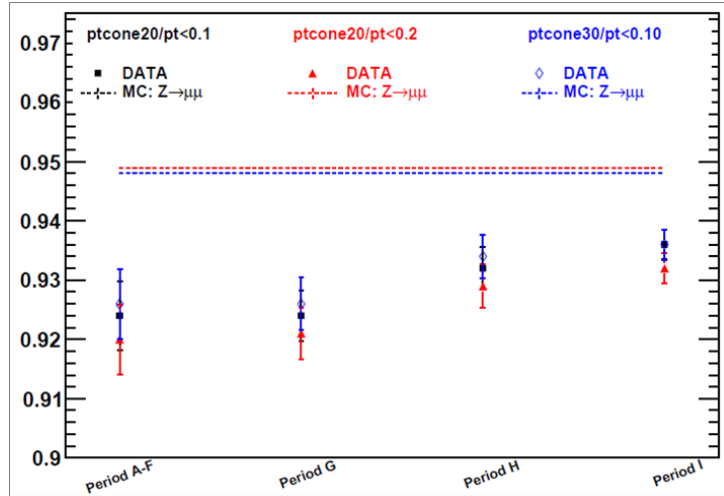


Figure 14: The CB muon efficiency for four run periods.

| Isolation cone size | Isolation cut | ϵ_{CB} (Data) | ϵ_{CB} (MC) | Ratio |
|---------------------|---------------|------------------------|----------------------|-------|
| 0.2 | 0.05 | (93.2 ± 0.17)% | (94.8 ± 0.03)% | 98.3% |
| 0.2 | 0.10 | (93.2 ± 0.17)% | (94.8 ± 0.03)% | 98.3% |
| 0.2 | 0.15 | (93.1 ± 0.17)% | (94.8 ± 0.03)% | 98.2% |
| 0.2 | 0.20 | (92.9 ± 0.17)% | (94.8 ± 0.03)% | 98.0% |
| 0.3 | 0.05 | (93.3 ± 0.19)% | (94.7 ± 0.03)% | 98.5% |
| 0.3 | 0.10 | (93.3 ± 0.17)% | (94.7 ± 0.03)% | 98.5% |
| 0.3 | 0.15 | (93.2 ± 0.17)% | (94.8 ± 0.03)% | 98.3% |
| 0.3 | 0.20 | (93.1 ± 0.17)% | (94.8 ± 0.03)% | 98.2% |
| 0.4 | 0.05 | (93.5 ± 0.20)% | (94.7 ± 0.03)% | 98.7% |
| 0.4 | 0.10 | (93.4 ± 0.18)% | (94.7 ± 0.03)% | 98.6% |
| 0.4 | 0.15 | (93.3 ± 0.18)% | (94.7 ± 0.03)% | 98.5% |
| 0.4 | 0.20 | (93.3 ± 0.17)% | (94.7 ± 0.03)% | 98.5% |

Table 23: ϵ_{CB} and data/MC scale factor measured for different isolation cone sizes and isolation cut values used for the probe track.

6.2.2 ID muon efficiency (ϵ_{ID})

For the ID muon efficiency measurement, the *tag muon* has the same requirements as the *tag muon* used for ϵ_{CB} determination. The *probe muon* is a muon with $p_T^{MS} > 10$ GeV, $|\eta| < 2.4$ and $\text{ptcone20}/p_T < 0.1$. To further reduce the QCD backgrounds, the *probe muon* is required to have opposite charge with the *tag muon* and the invariant mass of the tag-probe muons must be within the Z mass window $75 < M_{\mu+\text{track}} < 105$ GeV. The MS muon and the *Tag muon* are also required to be back-to-back with $|\Delta\phi| > 2$ and to come from the same primary vertex with $|\Delta d_0(\mu\mu)| < 0.2$ mm and $|\Delta z_0(\mu\mu)| < 2$ mm. We then check how often the *probe MS muon* is a combined muon with the pixel, SCT and TRT hit requirements and $|p_T^{ID} - p_T^{MS}|/p_T^{ID} < 0.5$. The ID muon efficiency as a function of muon p_T , η and ϕ are shown in Fig. 15. The matching efficiency is found to be $(99.0 \pm 0.07)\%$ in data and $(99.2 \pm 0.01)\%$ in MC. Figure 16 shows the efficiency for four different run periods and a systematic uncertainty of 0.1% is assigned. We also repeat this measurement using different definitions of muon isolation and cut values, the efficiency is found to be exactly the same. We check the background fractions using the MC simulated events. The amount of background is estimated to be 0.009% from $W + \text{jets}$, 0.245% from QCD dijet, 0.07% from $t\bar{t}$ and 0.003% from $W \rightarrow \mu\nu$ events. With and without background subtraction, the efficiency difference is 0.3%. The overall data/MC scale factor is $0.998 \pm 0.001(\text{stat}) \pm 0.003(\text{syst})$.

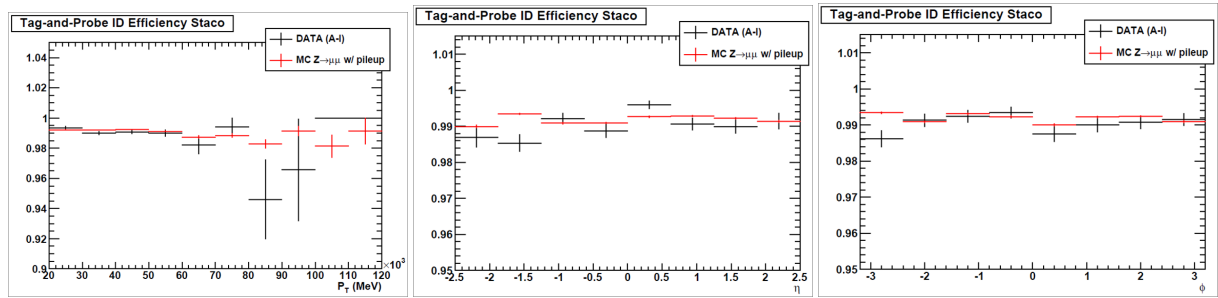


Figure 15: The ID muon efficiency as a function of muon p_T , η and ϕ .

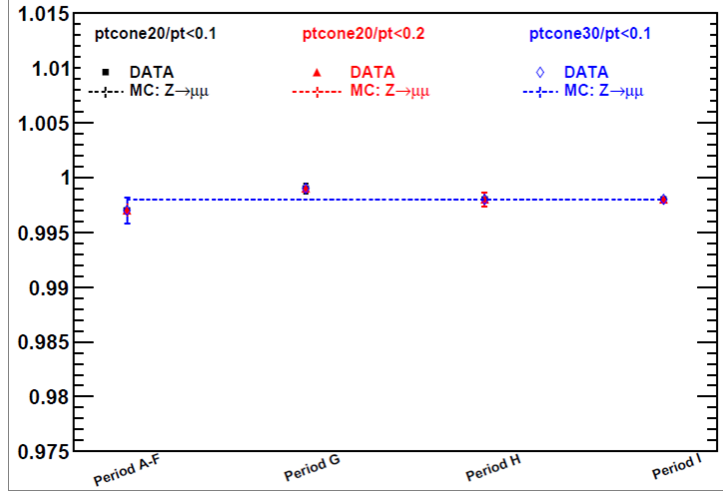


Figure 16: The ID muon efficiency for four run periods.

6.2.3 Muon isolation efficiency (ϵ_{iso})

For the muon isolation efficiency measurement, the *tag muon* has the same requirements as that used for ϵ_{CB} determination. The *probe muon* is a combined muon without requiring isolation. The *probe Muon* should have $p_T > 20$ GeV, $|\eta| < 2.4$, $|\Delta d_0| < 1$ mm and $|\Delta z_0| < 5$ mm. To further reduce the QCD backgrounds, the *probe muon* is required to have opposite charge with the *tag muon* and the invariant mass of the two muons must be within the Z mass window $75 < M_{\mu+\text{track}} < 105$ GeV. The two muons are also required to be back-to-back with $|\Delta\phi| > 2$ and come from the same primary vertex with $|\Delta d_0(\mu\mu)| < 0.2$ mm and $|\Delta z_0(\mu\mu)| < 2$ mm. We then check how often the *probe muon* passes the isolation requirement $\text{ptcone}20/p_T < 0.1$. The isolation efficiency is found to be $(99.3 \pm 0.06)\%$ in data and $(99.4 \pm 0.01)\%$ in MC. Figure 18 shows the efficiency for four different run periods where the efficiency varies by 0.4%. We also check the background fraction using MC simulated events. The amount of background is estimated to be 0.04% from $W+\text{jets}$, 0.21% from QCD dijet, 0.07% from $t\bar{t}$ and 0.04% from $W \rightarrow \mu\nu$ events. These background have negligible effects on the efficiency measurement. The data/MC scale factor is found to be $0.999 \pm 0.0006(\text{stat}) \pm 0.004(\text{syst})$.

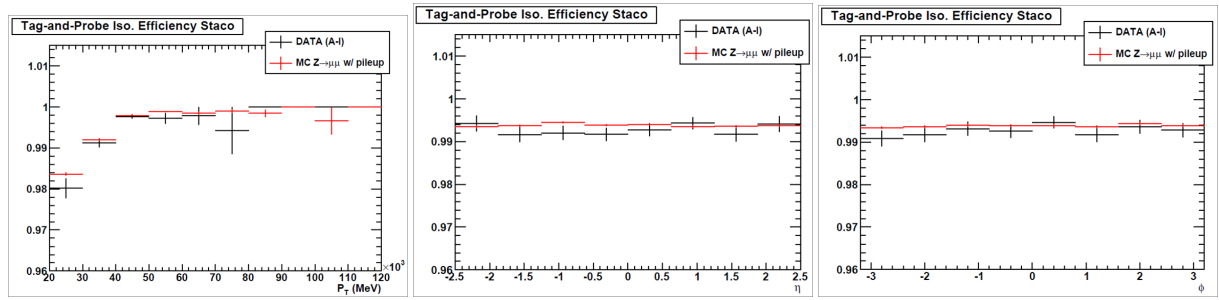


Figure 17: The muon isolation efficiency as a function of muon p_T , η and ϕ .

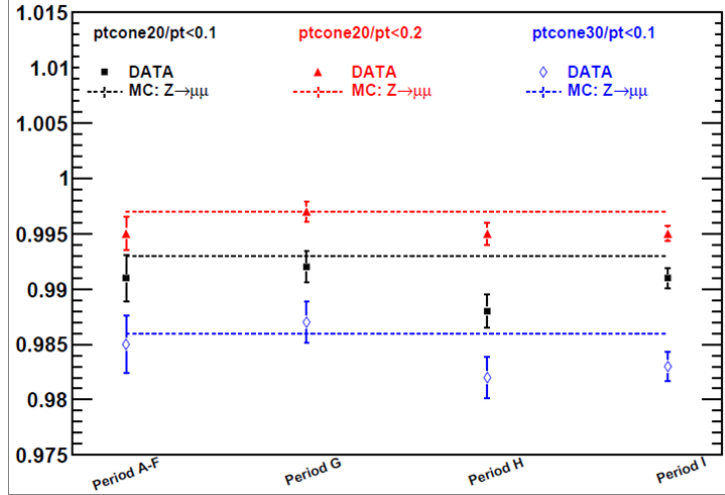


Figure 18: The muon isolation efficiency for four run periods.

6.2.4 Overall muon reconstruction and identification efficiency ($\epsilon_{CB} \times \epsilon_{ID} \times \epsilon_{iso}$)

The overall muon reconstruction and identification efficiency is the multiplication of ϵ_{CB} , ϵ_{ID} and ϵ_{iso} . It is found to be $(91.62 \pm 0.19)\%$ in data and $(93.48 \pm 0.03)\%$ in MC. The data/MC scale factor is 0.980 ± 0.008 . The systematics on overall muon identification scale factor is around 1% as the combination of CB, ID and Iso.

Independent tag-probe studies of the muon combined efficiencies can be found at [15] and [16], the results are consistent with what have been shown here. Studies about the ID track matching efficiency and isolation efficiency can also be found at [16], the data/MC efficiency scale factors are found to be very stable versus muon p_T and η .

6.2.5 Muon momentum resolution and scale

Based on the studies on the $Z \rightarrow \mu\mu$ invariant mass distribution, we observed that the muon momentum resolution in data was not well reproduced in the MC simulation [13]. Additional muon momentum smearing in MC is necessary to get better data/MC agreement. The muon momentum scale and extra-smearing parameters are determined using the dimuon mass distribution from Z decays and the charge times curvature difference between the MS and ID muons ($(q/p_T^{MS} - q/p_T^{ID})$ distribution) from W decays based on the recommendations from the muon combined performance group [17]. These distributions in data are compared with the predictions in MC with different smearing parameters applied. A negative log likelihood is calculated to determine the best smearing parameters. These smearing parameters are determined for four detector regions (barrel, transition, endcap and CSC) separately. The determined extra-smearing parameters are then applied on MC events. The muon momentum scale is found to be consistent with 1 and has an uncertainty of 0.1%-0.4% depending on the detector region. For the momentum smearing, two terms that represent multiple scattering and intrinsic detector resolution are introduced, the measured values together with statistical and systematic uncertainties are listed in [18].

To estimate the systematic uncertainties, we repeat the whole analysis by varying the momentum scaling and smearing parameters used in the MC simulation by $\pm 1\sigma$. For $\mu\mu$ channel, the relative change is 0.56% for number of W^+W^- signal and 0.77% for number of backgrounds. For $e\mu$ channel, the relative change is 0.22% for number of W^+W^- signal and 0.04% for number of backgrounds. The systematic uncertainty is smaller for $e\mu$ channel due to the fact that there is only one muon in the final state.

6.3 Jet Reconstruction

Jets are reconstructed from topological clusters using the Anti- k_T algorithm [19] with the size parameter $D = 0.4$. These jets are calibrated from the electromagnetic (EM) scale to the hadronic energy scale using a E_T and η dependent correction factor(EM-JES) [20] based on Monte Carlo simulation. The selected jets are required to have $E_T > 20$ GeV at the hadronic energy scale and $|\eta| < 3$. In this setup the systematics of the jet energy resolution (JER) is $\sim 14\%$, see Ref. [21]. The jet energy scale (JES) uncertainty depends on E_T and η and it is less than 10% for $E_T > 20$ GeV and $|\eta| < 2.8$, see Ref. [22]. The JES uncertainty tends to increase with decreasing E_T .

Selected jets are identified as b -jets if they contain a displaced secondary vertex reconstructed by the SV0 algorithm [23] with a weight greater than 5.72. In this analysis, b -tagging is only used in a control sample to extract top backgrounds. This entails the measurement of a ratio in which the efficiency of b -tagging cancels out. For this reason the $E_T > 20$ GeV threshold is used.

6.3.1 Jet energy scale uncertainty effects on jet veto

To minimize the top and other QCD background contributions to $WW \rightarrow \ell^+\ell^- E_T^{\text{miss}}$ signals, a jet veto cut is used in this analysis. The major uncertainty for the jet veto cut comes from jet energy scale uncertainties. To understand the influence of jet energy scale uncertainty on W^+W^- event selection, we conduct a study by following a procedure below:

- Use the ATLAS analysis tool *JESUncertaintyProvider* to obtain the *JES* and the associated uncertainty (*JESUncert*) as functions of jet E_T and η .
- Recalculate the *JES* for each selected jet by using the following formula

$$JES_{\text{new}} = JES \times (1 \pm JES\text{Uncert}) \times (1 + JERE\text{ffects}),$$

where *JERE\text{ffects}* is the jet energy resolution effects (ATLAS-COM-PHYS-2011-031); and \pm indicating changing the *JES* “up” and “down” to obtained the systematics for the jet veto cut.

- Use JES_{new} to re-calculate the jet transverse energy E_T^{jet} .
- Propagate the changes of *JES* to the E_T^{miss}
- Select the W^+W^- events using different *JES* (“up” and “down”) to recalculate the jet energies and to apply the jet veto in selection.
- The systematic uncertainties for jet veto are determined by the ratio of the selected events (normalized to 34 pb^{-1} integrated luminosity): $0.5 \times (N_{\text{DOWN}} - N_{\text{UP}})/N_{\text{nominal}}$.

Table 24 gives the jet-veto systematic uncertainties for different processes. The top events have the largest uncertainty, 40%; The W^+W^- signal acceptance uncertainty due to jet veto is about 6.7% based on MC studies. The average background uncertainty for jet veto is about 27%.

6.3.2 Extraction of the jet veto efficiency from data

The acceptance of the jet veto for W^+W^- events can be measured using Z boson decays to leptons, with Monte Carlo accounting for the difference in acceptance between W^+W^- and Z production for the jet veto. This can be expressed by the equation,

| Source | $N_{nominal}$ | N_{UP} | N_{DOWN} | $0.5 \times (N_{DOWN} - N_{UP})/N_{nominal}$ |
|-----------------|-----------------|-----------------|-----------------|--|
| Top | 0.58 ± 0.10 | 0.41 ± 0.08 | 0.85 ± 0.11 | 0.40 |
| W+X | 0.48 ± 0.25 | 0.36 ± 0.23 | 0.48 ± 0.25 | 0.10 |
| Z+X | 0.25 ± 0.07 | 0.24 ± 0.07 | 0.53 ± 0.15 | 0.58 |
| other Diboson | 0.40 ± 0.05 | 0.39 ± 0.05 | 0.45 ± 0.05 | 0.079 |
| W^+W^- signal | 8.05 ± 0.06 | 7.49 ± 0.06 | 8.56 ± 0.07 | 0.067 |

Table 24: Selected MC events in different processes for different jet energy scale and uncertainties. The number of selected events from different processes are normalized to 34 pb^{-1} .

$$\epsilon_{WW}^{data} = \epsilon_Z^{data} \frac{\epsilon_{WW}^{MC}}{\epsilon_Z^{MC}}, \quad (7)$$

where $\epsilon = N_{0 \text{ jets}}/N_{\geq 0 \text{ jets}}$ for each sample.

The measurement of ϵ_Z^{data} has a small statistical uncertainty, and a negligible uncertainty from background contamination. The Monte Carlo prediction of $\frac{\epsilon_{WW}^{MC}}{\epsilon_Z^{MC}}$ has uncertainties from the choice of renormalization and fragmentation scales, and from uncertainties on the parton distribution functions. These have been investigated at the parton level [24], with the result that the ratio has a theoretical uncertainty of ≈ 0.05 .²

Another uncertainty arises from the modelling of cuts used to select W^+W^- events relative to Z boson events. The main source of this uncertainty is expected to arise from the modelling of the cut on missing E_T , which is only applied to the W^+W^- sample. The effect of this cut is studied for $N_{0 \text{ jets}}$ in Section 6.4 and included as part of the systematic uncertainty on the W^+W^- acceptance due to modelling of missing E_T .

The uncertainty due to the jet energy scale is investigated by varying the jet energies up and down by the 1σ uncertainty on the jet energy scale, corresponding to a change in jet P_T of $\pm 1.4 \text{ GeV}$, and recalculating the efficiency ratio $\frac{\epsilon_{WW}^{MC}}{\epsilon_Z^{MC}}$. This is a simplified, more conservative method compared to that described in Section 6.3.1. However, since the uncertainty is itself small in comparison to the theory error, any slight overestimation of this uncertainty has only a small effect on the overall error.

A further source of uncertainty arises from the modelling of the Z mass distribution. The effect this has on the estimated jet veto efficiency for W^+W^- is determined by varying the width of the Z mass window from $|M_Z - M_{ll}| < 12 \text{ GeV}$ to $|M_Z - M_{ll}| < 10$ and 15 GeV .

The results of the measurements of ϵ_Z^{data} and $\frac{\epsilon_{WW}^{MC}}{\epsilon_Z^{MC}}$ are shown in Table 25, with the statistical uncertainty on the ϵ_Z^{data} measurement and the theoretical and experimental uncertainties on $\frac{\epsilon_{WW}^{MC}}{\epsilon_Z^{MC}}$ shown separately. The ϵ_Z^{data} measurement uses the same lepton identification and fiduciality as used for the W^+W^- cross section measurement. The W^+W^- selection for $N_{0 \text{ jets}}$ is the same as that of the cross section measurement. We use MC@NLO for the measurement of $\frac{\epsilon_{WW}^{MC}}{\epsilon_Z^{MC}}$. In practice, the jet veto acceptance is applied as a correction of $\frac{\epsilon_{WW}^{data}}{\epsilon_{WW}^{MC}} = 0.966 \pm 0.013(\text{stat}) \pm 0.011(\text{syst}) \pm 0.058 \text{ (theory)} = 0.966 \pm 0.060(\text{stat+syst+theory})$ to the W^+W^- acceptance prediction.

²The reference has investigated a variety of center-of-mass energies and uses different mass windows for the Drell-Yan normalization, but finds small variation in the uncertainty for the different choices (though an uncertainty is not quoted for the specific case of $\sqrt{s} = 7 \text{ TeV}$ and $|M_Z - M_{ll}| < 12 \text{ GeV}$).

| | Value | Stat. error | Syst. error | Theory error | Combined error |
|--------------------------------------|-------|-------------|-------------|--------------|----------------|
| ϵ_Z^{data} | 0.732 | 0.007 | - | - | 0.007 |
| ϵ_Z^{MC} | 0.759 | 0.0006 | - | - | 0.0006 |
| ϵ_{WW}^{MC} | 0.633 | 0.002 | - | - | 0.002 |
| $\epsilon_{WW}^{MC}/\epsilon_Z^{MC}$ | 0.834 | 0.002 | 0.007 | 0.050 | 0.051 |
| ϵ_{WW}^{data} | 0.612 | 0.008 | 0.007 | 0.037 | 0.038 |

Table 25: The jet veto efficiency for Z data and Z and W^+W^- MC with errors. These quantities are used to calculate the expected jet veto efficiency in W^+W^- data, which is also shown in the table.

6.4 Missing Transverse Energy Determination

The missing transverse energy (E_T^{miss}) is determined by the energy collected by the electromagnetic and hadronic calorimeters and by the muons measured by the muon spectrometer and inner detector. The E_T^{miss} attributed to the calorimeters is the sum of the transverse energy of calibrated topological clusters which is stored in the MET_LocHadTopo term. Topological clustering extends to $|\eta| < 4.5$ allowing nearly all of the transverse energy in an event to be recorded in calibrated topological clusters. The region from $4.5 < |\eta| < 5.0$ is excluded because of energy calibration problems in the FCAL. Topological clusters are seeded by calorimeter cell deposits having energy exceeding 4 standard deviations of the cell noise level. Neighboring cells having energy greater than 2 standard deviations of the noise level are then added and finally all neighboring cells are included regardless of the energy deposit. Calibration is applied at the local hadron level which corrects for the non-compensating nature of the detector as well as for dead material and out of cluster deposits.

The momentum carried by muons which escape the calorimeters is accounted for by including measurements of the muon track. For isolated muons ($\Delta R(\text{Muon}, \text{Jet}) > 0.3$) in $|\eta| < 2.4$ the corresponding E_T^{miss} is obtained from the combined inner detector and muon spectrometer track, accounting for double counting of energy lost by the muon in the calorimeters. For non-isolated muons or muons outside of the inner detector acceptance ($2.4 < |\eta| < 2.7$) the E_T^{miss} is obtained from the muon spectrometer track only. The E_T^{miss} from muon track measurements is contained in the MET_MuonBoy term while energy double counting in the calorimeter is prevented by subtracting the MET_RefMuonTrack term. The exact formula used in the W^+W^- analysis to calculate E_T^{miss} is (following the JetEtMiss group's recommendation [25]):

$$\cancel{E}_X = \text{MET_LocHadTopo_etx} + \text{MET_MuonBoy_etx} - \text{MET_RefMuonTrack_etx}$$

$$\cancel{E}_Y = \text{MET_LocHadTopo_ety} + \text{MET_MuonBoy_ety} - \text{MET_RefMuonTrack_ety}$$

$$E_T^{\text{miss}} = \sqrt{(\cancel{E}_X)^2 + (\cancel{E}_Y)^2}$$

6.4.1 Relative Missing Energy

This analysis uses a modified missing transverse energy, E_T^{miss} Relative ($E_{T, \text{Rel}}^{\text{miss}}$) which is defined as

$$E_{T, \text{Rel}}^{\text{miss}} = \begin{cases} E_T^{\text{miss}} \times \sin(\Delta\phi_{\ell,j}) & \text{if } \Delta\phi < \pi/2 \\ E_T^{\text{miss}} & \text{if } \Delta\phi \geq \pi/2 \end{cases} \quad (8)$$

Where $\Delta\phi_{\ell,j}$ is the difference in phi between the E_T^{miss} and nearest lepton or jet. Using this variable tends to reduce the sensitivity to mis-measured leptons or jets therefore increasing the sensitivity to missing transverse energy from neutrinos. For example, high p_T muons have a large momentum uncertainty

which can easily cause momentum mis-measurement and fake E_T^{miss} . Therefore using the $E_{T,\text{Rel}}^{\text{miss}}$ variable reduces the background to the W^+W^- selection from high mass di-muon pairs. This variable is also less sensitive to the missing transverse energy created by decays of taus to a lepton and neutrinos.

6.4.2 Missing Energy Smearing

When analyzing Monte Carlo samples, a momentum smearing is applied to muons as described in section 6.2.5. The energy scale for electrons is oversmeared in MC for systematic studies and corrected in data as described in section 6.1.2. The amount by which the energy of each object is scaled must be propagated to the missing transverse energy. Any change in the p_T of muons passing full identification is added vectorially to the Met_MuonBoy term. Similarly, any change of the p_T of electrons passing full identification is added vectorially to the Met_LocHadTopo term.

6.4.3 Missing Transverse Energy Acceptance

The E_T^{miss} calculation depends not only on the charged lepton and jet p_T measurements but also on the underlying event contribution and activity from additional pp collisions. The simulation of the underlying event and pileup contributions in MC is checked with $Z \rightarrow ee$ and $Z \rightarrow \mu\mu$ events. In Z events, besides the two decayed high p_T charged leptons, we also have the system that is recoiling against the Z boson. The recoil system p_T is calculated as the following:

$$\vec{p}_T^{\text{rec}} = -[\vec{p}_T(\ell 1) + \vec{p}_T(\ell 2) + \vec{E}_T^{\text{miss}}]$$

where $\vec{p}_T(\ell 1)$ and $\vec{p}_T(\ell 2)$ are the transverse momentum vectors of the two charged leptons.

Due to the fact that the recoil system mainly contains neutral pions, charged pions and kaons, the detector responses to the recoil system and to the charged leptons are different. For Z s, the transverse momentum of the Z boson, \vec{p}_T^Z , can be obtained from either the measurement of the two charged leptons, or from the recoil activity in the event $-\vec{p}_T^{\text{rec}}$. To minimize the effect of the recoil system response relative to the charged lepton response, the momentum imbalance was measured with respect to the (η, ξ) -coordinate system. The η axis is defined as the bisector of the two charged lepton transverse directions. In the transverse plane, the axis orthogonal to the η axis is the ξ axis. The transverse momentum of the recoil system p_T^{rec} and the η -imbalance ($(\vec{p}_T^{\text{rec}} + \vec{p}_T^Z) \cdot \hat{\eta}$) are sensitive to the underlying event and pileup contributions. An additional Gaussian smearing with $\sigma = 1.72 \pm 0.12$ GeV for the E_T^{miss} vector along the x and y components is needed in order to get best agreement between the data and MC for the η -imbalance distribution. Figure 19 shows the data and MC comparison for p_T^{rec} and η -imbalance distributions. Good agreement between data and MC in both electron and muon channels have been observed. We check the W^+W^- signal and background estimations with and without the 1.72 GeV extra-smearing for the E_T^{miss} x and y components and find the systematic effect is less than 0.3%.

6.5 Event vertices and pileup

6.5.1 Reweighting for pile-up MC using event vertices

As the instantaneous luminosity and collision rates increase, one event can contain multiple interactions, also referred to as pile-up. Pile-up may produce extra tracks and more energy deposited in the calorimeter system. This influences the applied event selection criteria such as lepton identification, isolation requirements and E_T^{miss} calculation.

The pile-up MC used in this analysis is simulated with a mean number of ~ 2 interactions per event, which may not model well the real pile-up situation in collision data. Since the number of primary vertices in the events is directly related to pile-up, we compare the number of good vertices with at least

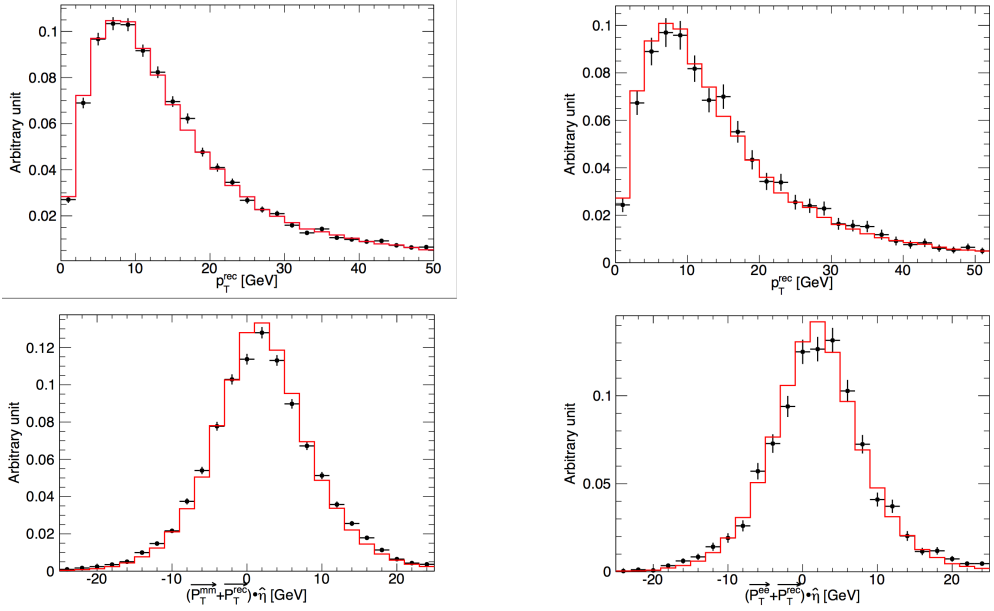


Figure 19: Data and MC comparison the left two plots are for $Z \rightarrow \mu\mu$, and the right two plots are for $Z \rightarrow ee$ events.

3 good reconstructed tracks in both data and pile-up MC samples. We obtain reweighting factors for MC events by correcting the vertex multiplicity distribution in MC to data. These reweighting factors are then applied to the pile-up MC events in the analysis. The procedure used follows the ATLAS EW Group recommendation [26], and the details are described in the following:

1. Events with leptons are selected with the common GRL and trigger requirements as described in section 7. The lepton definitions are the same as used in the W^+W^- analysis, except that the lepton p_T threshold is lowered to 15 GeV to increase the data sample statistics.
2. The number of collision vertices (N_{vtx}) each having at least 3 good reconstructed tracks are counted and then filled in a histogram to obtain the vertex multiplicity distribution. The histograms with the full dataset and pileup MC samples are used to determine the pile-up reweighting correction factors.
3. The distributions of N_{vtx} from data for different run periods are shown in Figure 20 with a comparison with the vertex distributions of W^+W^- MC signal. Increasing pile-up can be observed in these plots: the distributions of the vertices vary over data taking periods, and data are compared with MC period by period in order to obtain the reweighting factors. The pile-up MC samples used in the W^+W^- analysis are simulated with an average of 2 vertices per event; therefore they should have identical vertex distributions as shown in Figure 21.
4. Using the histograms for N_{vtx} obtained in the previous steps, the correction factors are determined bin by bin by comparing data with W^+W^- MC signal. In each N_{vtx} bin, the percentage is calculated from the number of events in this bin over the total entries of the histogram. We obtain the event fraction for each bin in data and in MC. The MC reweighting factors are the ratios of the event fraction of data to that of MC in each bin. The reweighting factors and the corresponding statistical errors are shown in Figure 22 for different run periods. The summary of the vertex reweighting factors can be found in Table 26. Please note that data collected in periods A,B,C and D are merged to get sufficient statistics. The same was done for periods G4 and G5.

5. The final vertex reweighting factors used in the W^+W^- analysis are luminosity weighted based on the factors derived above. For each N_{vtx} bin, we weight the reweighting factors for all the run periods by their corresponding integrated luminosity and then sum them up to be the correction factor. The corresponding numbers are given in Table 27.
6. To validate these vertex reweighting factors, we apply them to MC W^+W^- signal samples. The effectiveness of the reweighting method can be observed in Figure 23.
7. We select events having two and only two leptons with $p_T > 15$ GeV and compare data with W^+W^- MC signal to obtain the correction factors. To estimate the systematic uncertainties on the reweighting factors, we vary the procedures described above and compare the results:
 - Select events with 1 good electron and compare data with a $W \rightarrow ev$ MC sample
 - Select events with 1 good muon and compare data with a $W \rightarrow \mu\nu$ MC sample
 - Select events with 2 good leptons and compare data with an inclusive W^+W^- signal MC sample
 - Select events with 2 good leptons and compare data with an inclusive Z MC sample
 - Vary the lepton p_T requirement for all the above with $p_T > 13, 15, 17$ and 20 GeV

With the different sets of reweighting factors obtained in the comparisons above, the systematic uncertainties are then calculated for each N_{vtx} bin as shown in Table 28, and finally we determine that the overall systematic uncertainty for vertex reweighting is about $\sim 1\%$.

8. We propagate the vertex reweighting systematics uncertainties to the W^+W^- analysis by varying the reweighting factors. We find that the overall systematics in the W^+W^- selection due to vertex reweighting is about 0.5%.

| run period | $N_{vtx}=1$ | $N_{vtx}=2$ | $N_{vtx}=3$ | $N_{vtx}=4$ | $N_{vtx}=5$ | $N_{vtx}=6$ | $N_{vtx}=7$ |
|------------|-------------|-------------|-------------|-------------|-------------|-------------|-------------|
| ABCD | 3.8437 | 1.1738 | 0.2618 | 0.0305 | 0.0699 | 0.0000 | 0.0000 |
| E | 0.5564 | 0.3068 | 0.0938 | 0.0350 | 0.0064 | 0.0016 | 0.0000 |
| F | 0.4273 | 0.3413 | 0.1647 | 0.0522 | 0.0128 | 0.0018 | 0.0000 |
| G1 | 0.2970 | 0.3503 | 0.2204 | 0.0882 | 0.0325 | 0.0116 | 0.0000 |
| G2 | 0.3133 | 0.3442 | 0.2289 | 0.0740 | 0.0310 | 0.0052 | 0.0034 |
| G3 | 0.2985 | 0.3522 | 0.2239 | 0.0910 | 0.0313 | 0.0030 | 0.0000 |
| G4,G5 | 0.2594 | 0.3708 | 0.2219 | 0.1104 | 0.0284 | 0.0091 | 0.0000 |
| G6 | 0.3138 | 0.3656 | 0.2156 | 0.0764 | 0.0218 | 0.0055 | 0.0014 |
| H1 | 0.2648 | 0.3431 | 0.2421 | 0.1023 | 0.0300 | 0.0145 | 0.0025 |
| H2 | 0.3134 | 0.3525 | 0.2040 | 0.0916 | 0.0273 | 0.0067 | 0.0030 |
| I1 | 0.1609 | 0.2961 | 0.2656 | 0.1566 | 0.0810 | 0.0276 | 0.0094 |
| I2 | 0.2115 | 0.3204 | 0.2569 | 0.1378 | 0.0536 | 0.0156 | 0.0037 |

Table 26: Vertex reweighting factors (Data/MC) for different run periods and different vertex multiplicity bins, including N_{vtx} from 1 to 7.

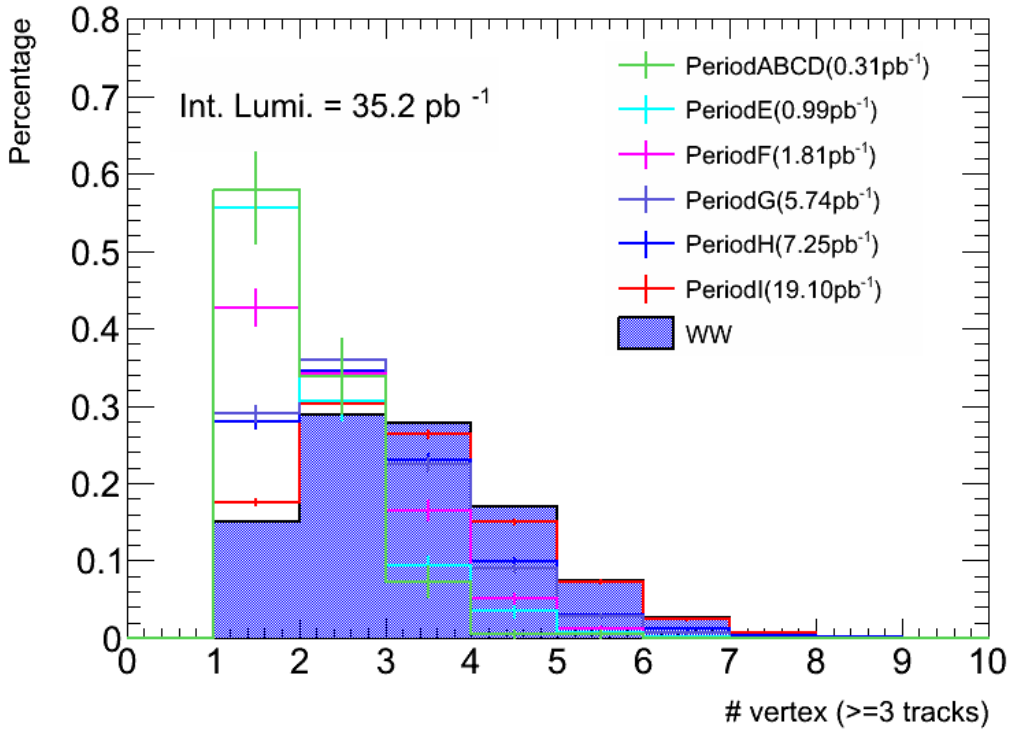


Figure 20: Vertex multiplicity distributions for the different data taking periods A-I compared with W^+W^- MC signal.

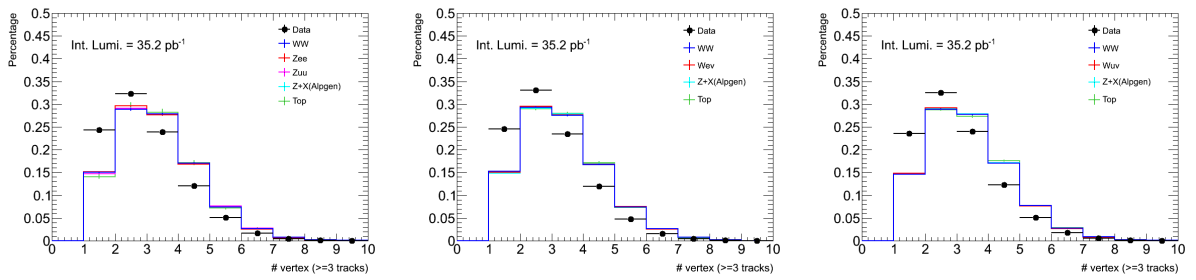


Figure 21: Vertex multiplicity distributions for different MC samples. Events are selected with two and only two leptons (left), at least one electron (middle), and at least one muon (right).

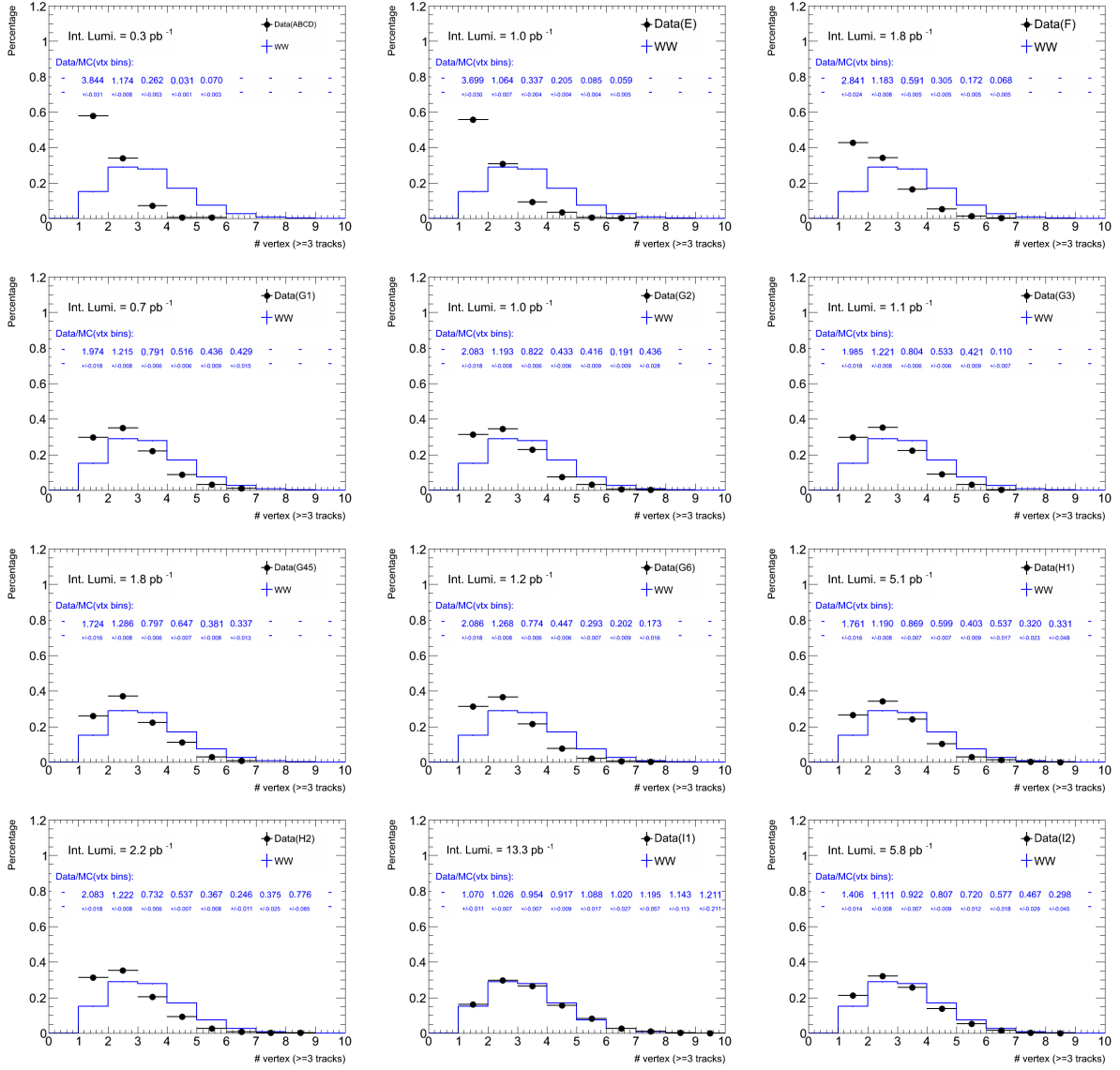


Figure 22: Determination of vertex reweighting correction factors by comparing MC with data for different run periods. MC samples are normalized to the integrated luminosities of the data periods considered.

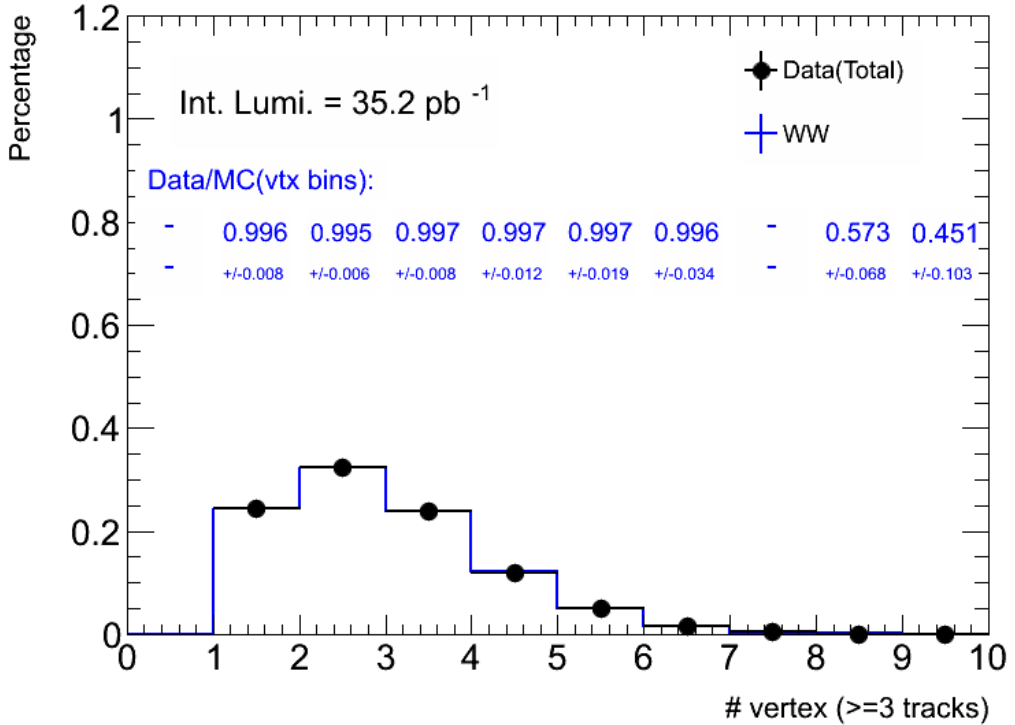


Figure 23: Validation of the vertex reweighting factors by applying them to W^+W^- MC signal samples and comparing the vertex distributions with data. Good agreement shows the success of this method.

| | $N_{vtx}=1$ | $N_{vtx}=2$ | $N_{vtx}=3$ | $N_{vtx}=4$ | $N_{vtx}=5$ | $N_{vtx}=6$ | $N_{vtx}=7$ |
|-----------------|-------------|-------------|-------------|-------------|-------------|-------------|-------------|
| CF (lumi. wgt.) | 1.6169 | 1.1216 | 0.8561 | 0.7070 | 0.6859 | 0.6218 | 0.6168 |
| stat. error | 0.0151 | 0.0076 | 0.0065 | 0.0078 | 0.0121 | 0.0191 | 0.0354 |

Table 27: Vertex reweighting factors CF (Data/MC) for different vertex multiplicity bins, which are the weighted average for all the data taking periods using their corresponding integrated luminosities. The statistical errors for the factors are also shown in the table. These reweighting factors are used in the W^+W^- analysis.

| | $N_{vtx}=1$ | $N_{vtx}=2$ | $N_{vtx}=3$ | $N_{vtx}=4$ | $N_{vtx}=5$ | $N_{vtx}=6$ | $N_{vtx}=7$ |
|-------------------|-------------|-------------|-------------|-------------|-------------|-------------|-------------|
| syst. uncertainty | 0.0097 | 0.0063 | 0.0056 | 0.0101 | 0.0283 | 0.0409 | 0.038 |
| overall syst. | 1% | | | | | | |

Table 28: Systematic uncertainties for the vertex reweighting. The overall uncertainty is calculated by adding the uncertainty of each bin weighted by its percentage in the vertex distribution.

6.5.2 Lepton track vertex and cut efficiencies

To reject tracks from cosmic ray muons and to reduce the numbers of muons from hadronic decays with secondary vertices, the impact parameter $d0$ of any lepton in the x-y plane with respect to the primary interaction vertex must be within 10 times the estimated standard deviation of that measurement. The distribution of the $d0$ resolution estimate in both data and MC has a maximum at 0.15 mm. The maximum of the effective cut value on $d0$ is therefore around 1.5mm. The efficiency of this cut in signal MC is 99% for electrons and 99.9% for muons.

A tag-probe method is also used to estimate the cut efficiency difference between data and MC. The impact parameter significance for *probe* electrons and muons is shown in Figure 24 and Figure 25, respectively. Table 29 and Table 30 show the results: the efficiencies obtained from data for both electrons and for muons agree well with MC simulations.

| $ d0/\sigma_{d0} < 10$ | Data | MC(Pileup) |
|-------------------------|----------------------|----------------------|
| Tag e | 383267 | 13559.40 ± 15.09 |
| Probe e | 5445 ± 74 | 5691.47 ± 9.77 |
| Probe e (Pass) | 5366 ± 73 | 5626.89 ± 9.72 |
| Efficiency | $98.55\% \pm 0.02\%$ | $98.87\% \pm 0.02\%$ |
| Eff(Data/MCSig) | | $99.68\% \pm 0.02\%$ |

Table 29: Electron $d0/\sigma_{d0}$ cut efficiency (Data VS MC)

| $ d0/\sigma_{d0} < 10$ | Data | MC(Pileup) |
|-------------------------|----------------------|-----------------------|
| Tag e | 156952 | 17541.32 ± 19.72 |
| Probe e | 9657 ± 98 | 10816.10 ± 15.49 |
| Probe e (Pass) | 9646 ± 98 | 10812.05 ± 15.49 |
| Efficiency | $99.89\% \pm 0.03\%$ | $99.96\% \pm 0.003\%$ |
| Eff(Data/MCSig) | | $99.93\% \pm 0.03\%$ |

Table 30: Muon $d0/\sigma_{d0}$ cut efficiency (Data VS MC)

6.6 Object Overlap Removal

Object reconstruction is followed by the “overlap removal” procedure. This procedure removes analysis objects where two or more analysis objects represent the same measurement. In this analysis, there are three different types of object overlap removal: e/e , μ/e and e/jet .

By far the most important of these is the e/jet overlap removal. Any calorimeter cluster associated with a high- p_T electron will also be reconstructed as part of a jet object. Therefore, if the electron object passes all quality criteria, any jet inside a cone of 0.3 around the electron in the $\eta\phi$ plane is removed. Energy from other clusters of that jet is not ignored and is considered in the calorimeter isolation criterion of the electron.

Removing the jet is not the optimal procedure, since the electron also affects the reconstruction and scale of additional jets, but since we only consider isolated electrons this effect should not be important for this study [27].

The other two removal schemes are meant to deal with rare problems, and are more relevant in the case of loosened quality criteria and have little effect with the current selection.

In rare cases (about 0.002% in the ALPGEN $Z \rightarrow \mu\mu$ MC) a muon traversing the detector will “fake” an electron cluster, for example by emitting a bremsstrahlung photon. This can result in an electron object

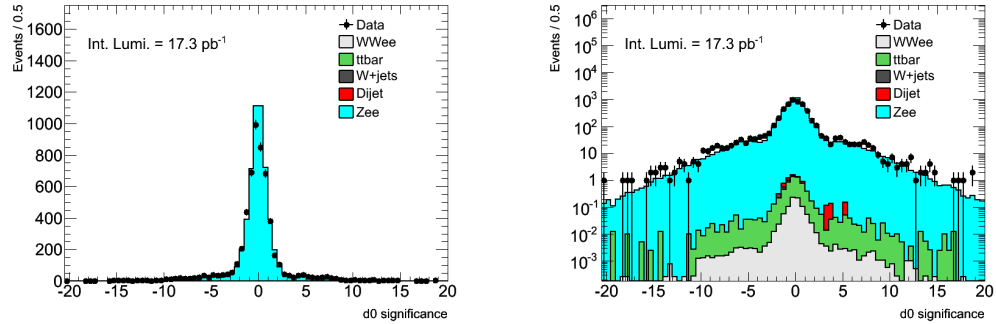


Figure 24: $d0/\sigma_{d0}$ distribution of probe electron, comparison between data and MC for period A-H.

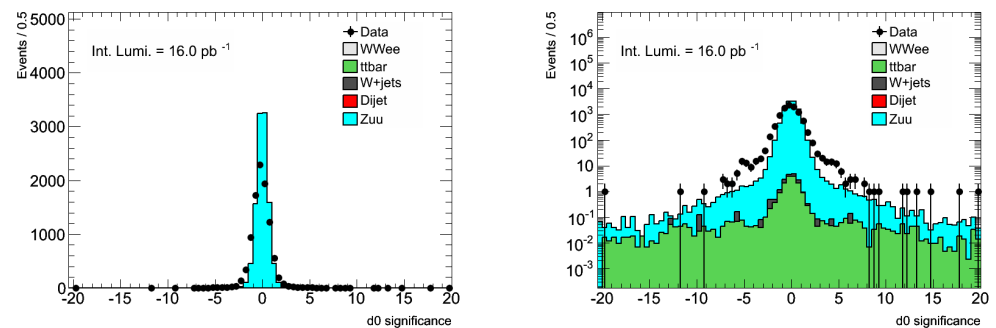


Figure 25: $d0/\sigma_{d0}$ distribution of probe muon, comparison between data and smeared MC for period A-H.

very close to the muon. For this reason any electron with a distance of less than 0.1 to a muon will be removed.

If multiple tracks point to the same calorimeter cluster, there can be two reconstructed electron objects, usually with low transverse momenta. To remove this duplication, if two electrons have a distance in the η - ϕ plane of 0.1 or less, the one with less transverse momentum is dropped. This has not yet occurred in data.

6.7 Summary of Overall Scale Factors

We summarize the scale factors for ee (Table 31), $\mu\mu$ (Table 32) and $e\mu$ (Table 33) channels separately, and indicate where to apply these scale factors to correct MC predictions. The lepton trigger and identification scale factors are applied to all MC estimates. The jet veto scale factor is estimated using data from Z events compared with MC@NLO MC predictions (see Section 6.3.2). Therefore, it only applies to MC events produced by MC@NLO (WW and WZ). The scale factors are determined by using Z samples, typical statistic uncertainty for muons is $\sim 0.2\%$ and around 0.4% for electrons. We only quote systematic uncertainties in SF summary tables.

| Source | Mean | Systematic Uncertainty | Apply to MC |
|---------------------------------------|-------|------------------------|-------------|
| ee trig. SF | 100% | 0.02% | |
| e eff. SF (ID) | 97.0% | 3.3% | |
| ee acceptance (E_T^e dependence) | 100% | 6.0% | |
| ee SF (trigger and ID) | 94.1% | 7.6% | all MC |
| Jet Veto Eff. SF | 96.6% | 6.0% | Diboson MC |

Table 31: Scale factors for event selection in ee channel ($94.1\% = 100\% \times 97.0\% \times 97.0\%$)

| Source | Mean | Systematic Uncertainty | Apply to MC |
|------------------------------|-------|------------------------|-------------|
| $\mu\mu$ trig. SF | 100% | 0.04% | |
| μ eff. SF (ID) | 98.0% | 1.0% | |
| $\mu\mu$ SF (trigger and ID) | 96.0% | 1.5% | all MC |
| Jet Veto Eff. SF | 96.6% | 6.0% | Diboson MC |

Table 32: Scale factors for event selection in $\mu\mu$ channel ($96.0\% = 100\% \times 98.0\% \times 98.0\%$)

| Source | Mean | Systematic Uncertainty | Apply to MC |
|---|-------|------------------------|-------------|
| $e\mu$ trig. SF | 100% | 0.02% | |
| e eff. SF (ID) | 97.0% | 3.3% | |
| μ eff. SF (ID) | 98.0% | 1.0% | |
| $e\mu$ acceptance (E_T^e dependence) | 100% | 3.4% | |
| $e\mu$ SF (trigger and ID) | 95.1% | 4.9% | all MC |
| Jet Veto Eff. SF | 96.6% | 6.0% | Diboson MC |

Table 33: Scale factors for event selection in $e\mu$ channel ($95.1\% = 100\% \times 97.0\% \times 98.0\%$)

7 Event Selection

The analysis includes three dilepton channels, $e^+e^-E_T^{\text{miss}}$, $\mu^+\mu^-E_T^{\text{miss}}$ and $e^\pm\mu^\mp E_T^{\text{miss}}$ final states. The muon and electron data streams (see Table 2) are used for analysis of $\mu\mu$ and ee channels, respectively. The inclusive $e\mu$ sample is obtained by using both muon and electron data streams, where duplicate events are removed. For all three channels, we applied common event selection criteria except that the Z-veto cut was applied only to the same flavor (ee and $\mu\mu$) dilepton events. The event selection cuts were optimized by trigger choices and by maximizing the signal to background ratio for W^+W^- detection. This section presents the cuts used in our analysis, the cut-flows, and the selected events. MC event selection results are also given in this section for comparison.

7.1 W^+W^- event selection criteria

The event selection includes a pre-filter at the stage of converting the AOD events from muon and electron data streams to WWD3PD ntuples. The filter cuts are given below.

- At least one muon or one electron candidate with $E_T > 10$ GeV and $\eta < 2.7$.
- Removal of the overlaps for combined muon and electron D3PD datasets.

The $W^+W^- \rightarrow \ell^+\nu_\ell\ell^-\bar{\nu}_\ell$ events are further selected (preselection) by requiring two leptons (ee , $\mu\mu$ or $e\mu$) from stable pp collisions and collected by muon or electron triggers. The transverse momentum of both leptons must be greater than 20 GeV. This cut is optimized for trigger efficiencies and associated uncertainties, as well as for W^+W^- signal detection sensitivities. Our study has shown that if lowering one lepton p_T threshold to 15 GeV in the event selection, the signal selection efficiency would increase by 10%, but background contributions (mainly $W+$ jets) would increase by 33%. The corresponding signal detection sensitivity would be slightly worse compared to requiring both leptons to have $p_T > 20$ GeV. The detailed cuts of the preselection are listed below.

1. **Data Quality:** Events must be in the *Good-Run-List*, reflecting luminosity blocks with fully functional sub-detectors during data taking.
2. **Object Overlap Removal:** Overlapping objects are removed, as described in Section 6.6. This removal can be summarized as follows:
 - e/e removal: If two electrons overlap within a cone of $\Delta R = 0.1$, remove e with lower $p_T(\text{cluster})$;
 - μ/e removal: If one muon and one electron overlap within a cone of $\Delta R = 0.1$, remove the electron;
 - e/jet removal: If one jet and one electron overlap within a cone of $\Delta R = 0.3$, remove the jet.
3. **MET Cleaning:** To remove effects from EM coherent noise, HEC spikes and cosmics/beam background on jet and E_T^{miss} reconstruction, we apply the “Loose” jet cleaning cuts as defined by the jet/MET group [28]. An event is removed if least one bad jet with E_T^{jet} (EM scale with JES correction) ≥ 20 GeV is found.
4. **Primary Vertex Selection:** The primary vertex (vertex with largest Sum P_T^2) is required to be reconstructed with at least 3 good tracks.
5. **Trigger Selection:** Each of the three signal channels has its own trigger requirement as outlined in Table 1:

- For ee events, L1_EM14 and EF_e15_medium are used for periods A-E3 and E4-I2, respectively.
- For $\mu\mu$ events, L1_MU10, EF_mu10_MG, EF_mu13_MG and EF_mu13_MG_tight are used for periods A-E3, E4-G1, G2-I1(run 167576) and I1(run 167607)-I2, respectively.
- For $e\mu$ events, the triggers used are the “OR” of the electron and muon triggers described above.
- For MC, we use luminosity-weighted triggers. For the electron channel, L1_EM14 or EF_e15_medium are used according to the integrated luminosity of periods A-E3 and E4-I2. For the muon channel, the same procedure is applied using L1_MU10 and EF_mu10_MG instead. The $e\mu$ channel uses again the “OR” of electron and muon triggers.

6. Dilepton Selection:

An event is selected if it has two and only two good leptons.

* The good electron selection criteria are:

- The electron reconstruction author is 1 or 3.
- It should pass the ”OTX” cleaning cut (to avoid LAr EM calorimeter dead regions). MC uses the last pp data run map `ObjectQualityMaps_run167521.root`, corresponding to the bulk of the integrated luminosity collected in data.
- $p_T(\text{cluster}) > 20 \text{ GeV}$ (to have a good trigger efficiency). Energy scale corrections for data are applied as detailed in Section 6.1.2.
- $|\eta| < 2.47$, $|\eta| < 1.37$ or $|\eta| > 1.52$ (using cluster- η).
- It must be a ”RobusterTight” electron [12].
- Cut on the longitudinal impact parameter: $|z_0(e)| < 10 \text{ mm}$.
- The transverse impact parameter significance w.r.t. the primary vertex must be less than 10: $|d_0/\sigma_{d_0}| < 10$.
- To reject QCD background, the electron must be isolated by requiring $\text{EtCone}30 < 6 \text{ GeV}$, where Etcone30 is the sum of transverse energy deposited in a cone $\Delta R = 0.3$ around the electron.

* The good muon selection criteria are:

- The muon is reconstructed as a combined staco muon.
- $p_T > 20 \text{ GeV}$ (to have a good trigger efficiency). For MC, the muon momentum scale and resolution are adjusted as detailed in Section 6.2.5.
- $p_T(\text{MS}) > 10 \text{ GeV}$, where $p_T(\text{MS})$ is the transverse momentum measured by the standalone muon spectrometer. This cut is to ensure that the muon is well identified within the muon spectrometer.
- $|\text{pt}(\text{MS}) - \text{pt}(ID)/\text{pt}(ID)| < 0.5$, where $\text{pt}(ID)$ is the transverse momentum measured by inner detector. This cut is to remove poorly reconstructed tracks and muons from π/K decays.
- Inner detector hits requirements:
 - $\text{nPixHits} \geq 1$ and $\text{nSCTHits} \geq 6$;
 - $(\text{nTRTOutliers} + \text{nTRTHits}) \geq 6$ and $\text{nTRTOutliers}/(\text{nTRTOutliers} + \text{nTRTHits}) < 0.9$ for $|\eta| < 1.9$;
 - $\text{nTRTOutliers}/(\text{nTRTOutliers} + \text{nTRTHits}) < 0.9$ for $|\eta| > 1.9$ and $(\text{nTRTOutliers} + \text{nTRTHits}) \geq 6$.

- $|\eta| < 2.4$.
- Cut on the longitudinal impact parameter: $|z_0(\mu)| < 10$ mm.
- The transverse impact parameter significance w.r.t. the primary vertex must be less than 10: $|d_0/\sigma_{d_0}| < 10$.
- The muon must be isolated by requiring $\text{PtCone20}/p_T < 0.1$, where PtCone20 is the sum of transverse momenta of the tracks around the muon in a cone $\Delta R = 0.2$.

7. Opposite Charge Requirement for the two leptons.

After the preselection, the dominant contribution (>97%) to ee and $\mu\mu$ events comes from the inclusive $Z/\gamma^* \rightarrow \ell^+\ell^-$ process. The W^+W^- signal only contributes $\sim 0.06\%$ of the selected events. For the $e\mu$ final state, the W^+W^- signal contributes already 9.7%, where the major background contributions come from $t\bar{t}$ /single-top (45%), $Z \rightarrow \tau\tau$ (27.2%) and QCD di-jets (12.4%). Above numbers are based on MC studies. Figures 26 and 27 show some relevant kinematic distributions after the preselection detailed above, where the MC has been normalized to the integrated luminosity of the dataset (34 pb^{-1}) using the NLO SM cross-sections. Figure 26 shows the lepton transverse momenta, $E_{T,\text{Rel}}^{\text{miss}}$, E_T^{miss} , minimum separation phi angle between E_T^{miss} and jet or lepton and for the ee , $\mu\mu$ and $e\mu$ channels. Figure 27 shows the dilepton invariant mass, transverse momentum, angular correlation distributions and jet multiplicity distributions. Data and MC agree well in all these distributions for pre-selected dilepton events, illustrating good understanding of our backgrounds.

The **final W^+W^- event selection cuts** are chosen to optimize the signal to background ratio, and are listed below.

- 1) The invariant mass of same-flavor dilepton pairs ($M_{\ell\ell}$) must be greater than 15 GeV to further remove dijet events. (See invariant mass distributions in Figure 27).
- 2) Z-veto: $|M_{\ell_1\ell_2} - M_Z| > 10$ GeV for the ee , $\mu\mu$ channels to remove events from $Z \rightarrow \ell^+\ell^-$.
- 3) $E_{T,\text{Rel}}^{\text{miss}} > 40$ GeV for the ee and $\mu\mu$ channels and > 20 GeV for the $e\mu$ channel. $E_{T,\text{Rel}}^{\text{miss}}$ is calculated as follows:

$$E_T^{\text{Rel}} = E_T \times \sin(\Delta\phi) \quad \text{if } \Delta\phi < \pi/2; \quad E_T^{\text{Rel}} = E_T \quad \text{if } \Delta\phi \geq \pi/2,$$

where $\Delta\phi$ is the minimum separation ϕ angle between lepton or jet and E_T^{miss} . For more details on E_T^{miss} see Section 6.4. The optimization of the chosen cut values is explained in Section 7.1.1. Figure 28 shows the $E_{T,\text{Rel}}^{\text{miss}}$ distributions without $E_{T,\text{Rel}}^{\text{miss}}$ applied for ee , $\mu\mu$ and $e\mu$ channels after Z mass veto cut(first row) and after jet-veto cut(second row).

- 4) Jet-veto: The number of jets ($E_T > 20$ GeV, $|\eta| < 3$) is required to be zero. Figure 29 shows the jet multiplicity distribution before the jet veto cut is applied to the selected W^+W^- candidate events. This cut removes very effectively inclusive top events with leptonic decay mode. Independent studies by several groups showed that including dilepton events with one jet would not increase the signal detection sensitivity (as an example, see Figure 30).

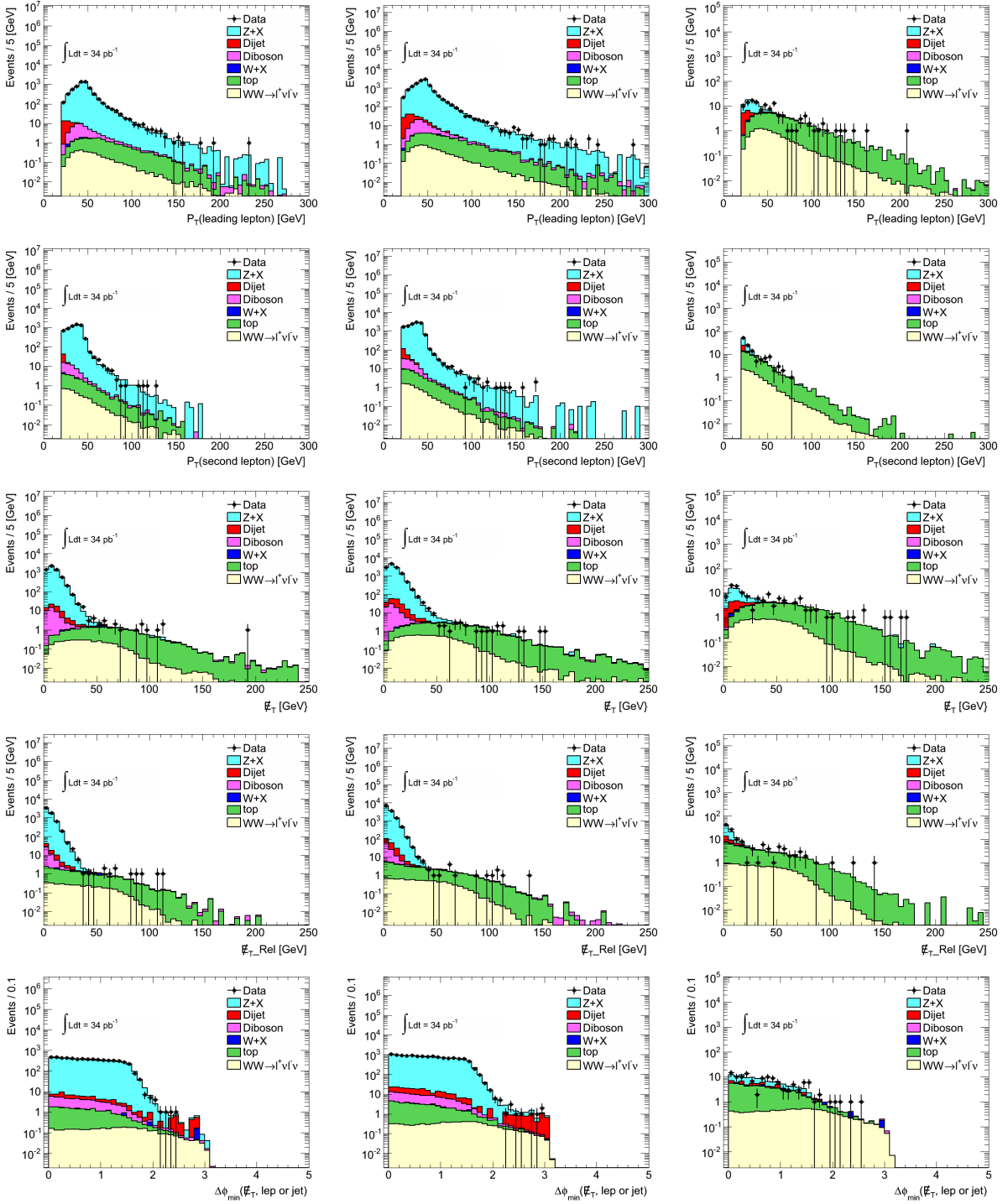


Figure 26: Kinematic variable distributions at preselection level (two good leptons) where the left column shows the ee channel, the middle column the $\mu\mu$ channel and the right column the $e\mu$ channel. The first row is the p_T of the lepton; the second row is the p_T of the trailing lepton; the third row is the relative missing E_T ($E_{T,\text{Rel}}$), the fourth row shows the original missing E_T , the bottom row shows the minimum separation phi angle between missing E_T and jet or lepton. The dots represent data and the stacked histograms are the MC predictions. Lepton trigger and identification scale factors (described in Section 6.7) are applied to MC.

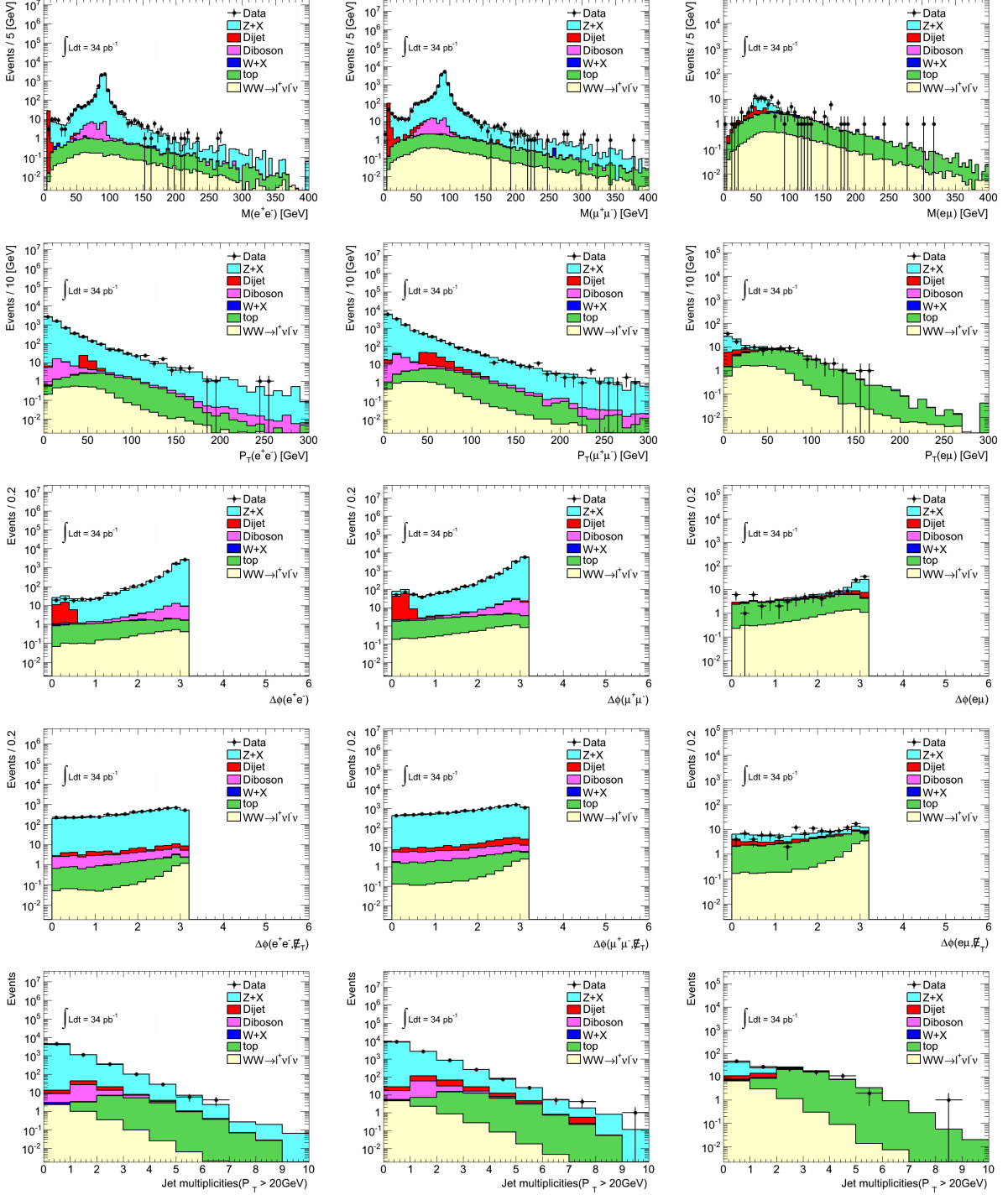


Figure 27: Distributions for the dilepton system at preselection level where the left column shows the ee channel, the middle column the $\mu\mu$ channel and the right column the $e\mu$ channel. The first row is the dilepton invariant mass; the second row is the dilepton p_T ; the third row is the ϕ angle separation between the two leptons, the fourth row shows the ϕ angle difference between dilepton system and E_T^{miss} , and the jet multiplicity is in the bottom row. The dots represent data and the stacked histograms are the MC predictions. Lepton trigger and identification scale factors (described in Section 6.7) are applied to MC.

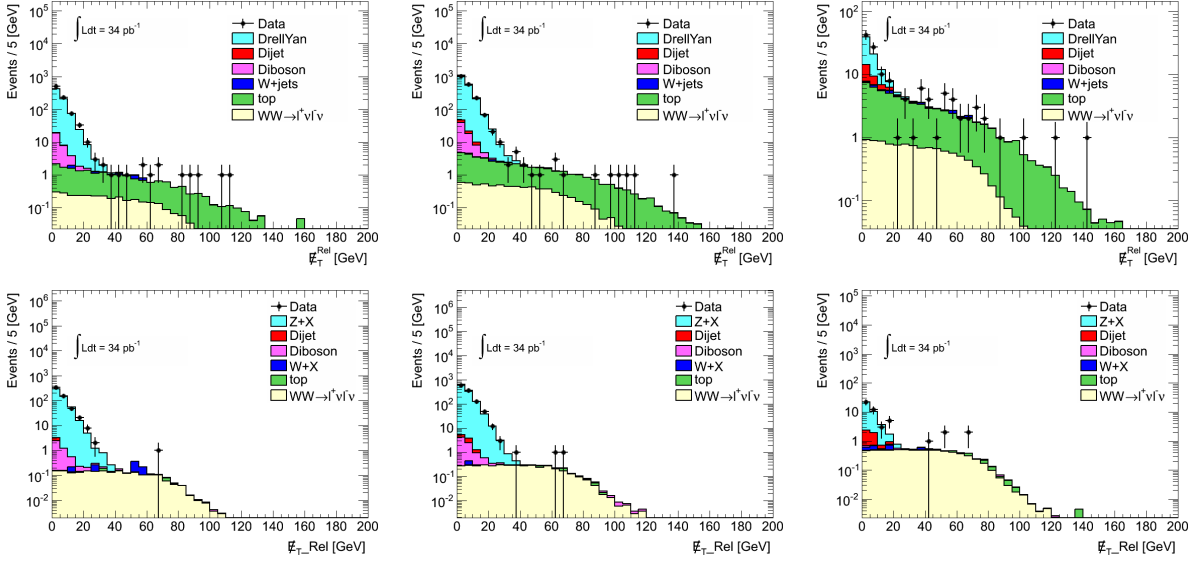


Figure 28: $E_{T,\text{Rel}}^{\text{miss}}$ distributions (without $E_{T,\text{Rel}}^{\text{miss}}$ cut applied) for ee (left), $\mu\mu$ (middle) and $e\mu$ (right) channels after the Z-veto cut (first row) and after jet-veto cut (second row). The dots represent data and the stacked histograms are the MC predictions. Lepton trigger and identification scale factors (described in Section 6.7) are applied to MC.

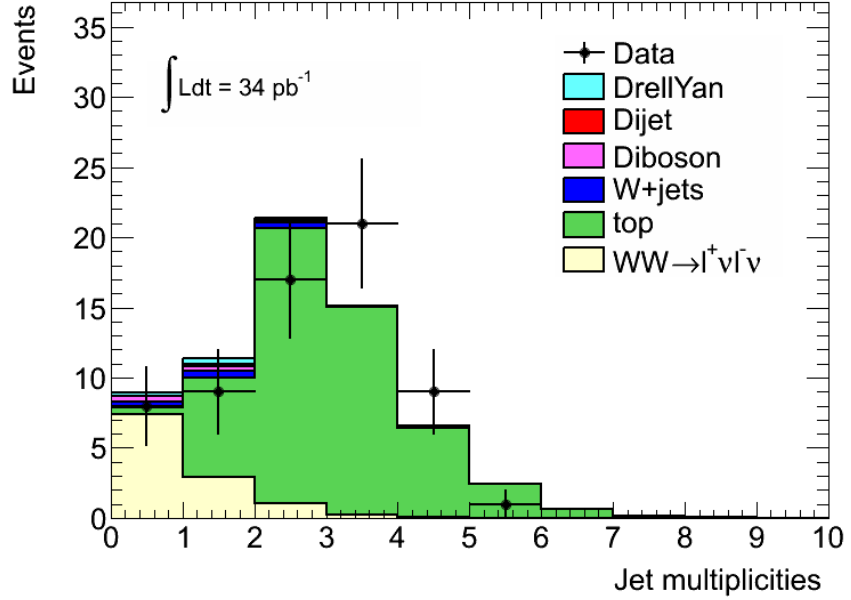


Figure 29: Jet multiplicity for events passing the full W^+W^- selection except jet veto. The dots represent data and the stacked histograms are the MC predictions. Lepton trigger and ID scale factors (described in Section 6.7) are applied to MC.

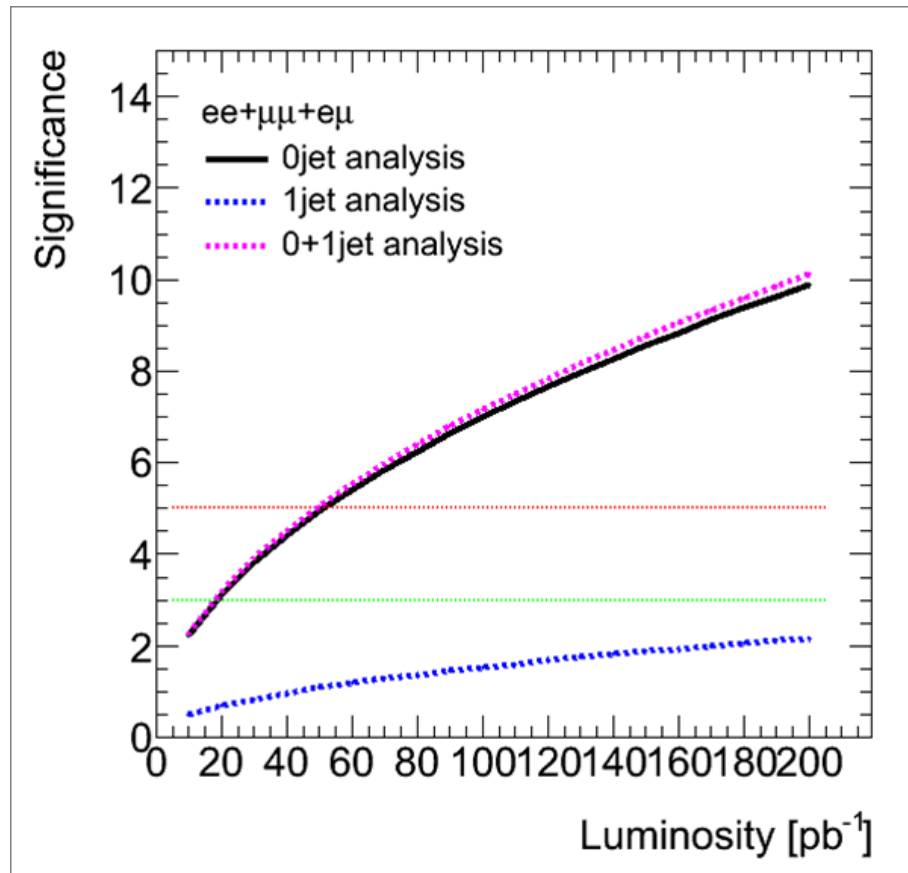


Figure 30: Comparison of W^+W^- detection sensitivity between selections using $\text{Njet}=0$ versus $\text{Njet}=0+1$, as a function of integrated luminosity.

7.1.1 Relative MET cut optimization

In order to suppress more efficiently Drell-Yan background, a $E_{T, \text{Rel}}^{\text{miss}}$ cut (section 6.4.1) is applied. The advantageous aspect of the $E_{T, \text{Rel}}^{\text{miss}}$ variable is the fact that it is almost insensitive to jet/lepton momentum mis-measurements, which fake E_T^{miss} . As a consequence, it is a powerful discriminating variable against all backgrounds, which do not have real MET.

To determine the optimal cut value, a MC-based signal sensitivity study is performed, taking into consideration only Drell-Yan events as background³. Signal sensitivity is calculated for every cut value of $E_{T, \text{Rel}}^{\text{miss}}$ in a 2 GeV bin, producing the so-called signal sensitivity curve. The peak of this curve indicates the cut value, which provides the highest sensitivity, and thus the optimal $E_{T, \text{Rel}}^{\text{miss}}$ cut value. To deal with limited MC statistics, 1 jet bin events were added to the 0 baseline jet bin, under the approximation that kinematics are not significantly changed. Adding more than 1-jet multiplicity events would be misleading, due to the fact that the top quark background becomes dominant.

Contamination from Drell-Yan to the $e^\pm\mu^\mp$ channel comes mainly from the $Z \rightarrow \tau^\pm\tau^\mp \rightarrow e^\pm\mu^\mp + v's$ background. True E_T^{miss} is expected in this case, contrary to the e^+e^- or $\mu^+\mu^-$ cases where no true E_T^{miss} is present. As a result, optimization study is done separately for the $e^\pm\mu^\mp$ channel and the merged $e^+e^-/\mu^+\mu^-$ channels. Kinematics of the e^+e^- and $\mu^+\mu^-$ channel are very similar, a fact, which motivates the merging of those channels, while MC statistics are increased.

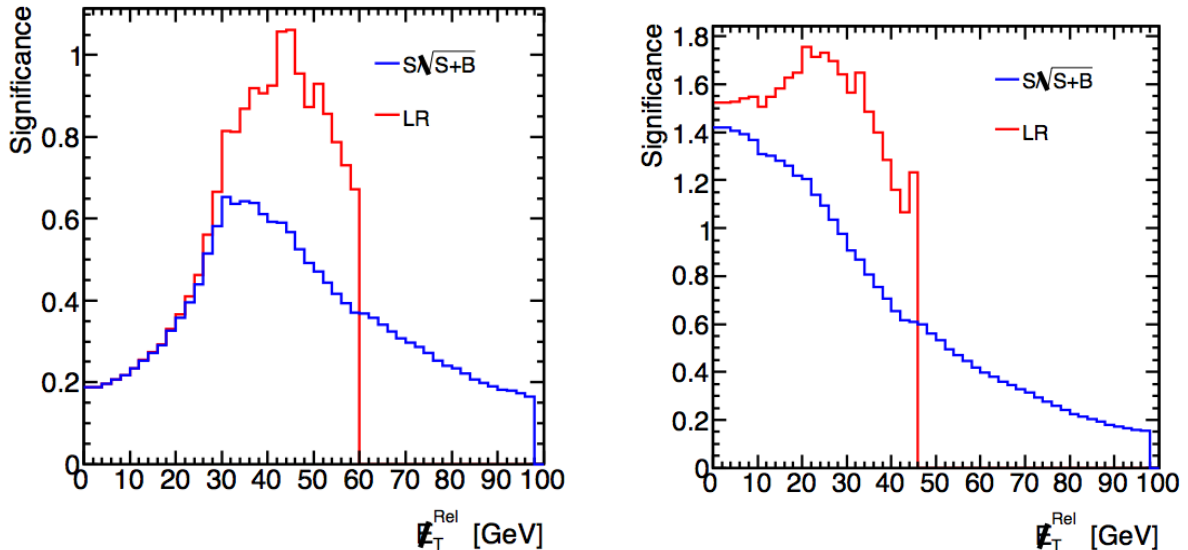


Figure 31: Signal significance curve as a function of the $E_{T, \text{Rel}}^{\text{miss}}$ cut value, for $e^+e^-/\mu^+\mu^-$ (left) and $e^\pm\mu^\mp$ (right).

The optimization study is performed after having applied all the preselection cuts and up to Z-veto cut from the final W^+W^+ event selection cuts, as described in section 7.1. Different combinations of all selection cuts were tested, and it was found that the highest signal sensitivity is achieved when applying the cuts mentioned above. Figure 31 shows the signal significance curve as a function of the $E_{T, \text{Rel}}^{\text{miss}}$ cut value, for both $e^+e^-/\mu^+\mu^-$ and $e^\pm\mu^\mp$. Two optimizing methods are used:

$$A = N_S / \sqrt{N_S + N_B} \quad (9)$$

$$LR = \sqrt{2(N_S + N_B)\ln(1 + N_S/N_B) - N_S} \quad (10)$$

where N_S is the number of signal events and N_B is the number of Drell-Yan background events. Method 9 is based on a simple, robust and intuitive criterion and it is shown as a reference. The curve

³ Drell-Yan events contain both low $M_{\ell\ell}$ ($10 \text{ GeV} < M_{\ell\ell} < 40 \text{ GeV}$) and high $M_{\ell\ell}$ ($M_{\ell\ell} > 40 \text{ GeV}$).

| | $E_T^{\text{miss}} > 30 \text{ GeV},$ $p_T^{ll} > 30 \text{ GeV}$ | $E_{T, \text{Rel}}^{\text{miss}}$ |
|--------------------------|--|-----------------------------------|
| WW | 7.18 ± 0.07 | 7.38 ± 0.07 |
| Drell-Yan | 0.94 ± 0.26 | 0.24 ± 0.14 |
| All backgrounds | 2.60 ± 0.42 | 1.97 ± 0.36 |
| $N_S / \sqrt{N_S + N_B}$ | 2.29 | 2.41 |
| LR | 3.40 | 3.79 |

Table 34: Event yields with SF application (section 10.1) and signal sensitivity when applying $E_T^{\text{miss}} > 30 \text{ GeV}$, $p_T^{ll} > 30 \text{ GeV}$ and $E_{T, \text{Rel}}^{\text{miss}}$ cut.

based on the likelihood ratio calculation (equation 10) is more appropriate, if one wants to achieve the best signal significance dealing with limited MC statistics. The optimal cut value is determined based on this latter method.

The peaks of the curve 9 in figure 31, determine the optimal cut value of $E_{T, \text{Rel}}^{\text{miss}}$ for the $e^+e^-/\mu^+\mu^-$ and $e^\pm\mu^\mp$ cases. It shows that highest sensitivity is achieved when:

- $E_{T, \text{Rel}}^{\text{miss}} = 40 \text{ GeV}$ for $e^+e^-/\mu^+\mu^-$ channel
- $E_{T, \text{Rel}}^{\text{miss}} = 20 \text{ GeV}$ for $e^\pm\mu^\mp$ channel

Other similar studies have been performed, testing other variables such as simplistic E_T^{Signif} , E_T^{miss} optimization, or using the $\Delta\phi(E_T^{\text{miss}}, lep)$ variable, etc. The best result -keeping the method as simple and robust as possible- is found by the use of $E_{T, \text{Rel}}^{\text{miss}}$.

As a reference, $E_{T, \text{Rel}}^{\text{miss}}$ cut efficiency is compared with the efficiency of the cuts used at the first phase of W^+W^- analysis, namely: $E_T^{\text{miss}} > 30 \text{ GeV}$ and $p_T^{ll} > 30 \text{ GeV}$, at the place of $E_{T, \text{Rel}}^{\text{miss}}$. Event yield⁴ for both cases and signal sensitivities are shown in table 34.

To conclude, $E_{T, \text{Rel}}^{\text{miss}}$ shows a remarkable control over the Drell-Yan background, with a suppression factor ~ 4 times larger, compared to the cuts used to the early phase of the analysis. Overall, higher suppression is achieved against all backgrounds, and the signal significance is accordingly improved.

⁴All scale factors are applied (see section 10.1).

7.2 Event selection cut-flow

The W^+W^- event selection cut-flow is shown in Table 35. We observed a total of 65 inclusive $\ell^+\ell^-E_T^{\text{miss}}$ events before jet veto, which is consistent with the MC expectation of 68 events for 34 pb^{-1} integrated luminosity. The signal to background ratio is about 0.2 for inclusive W^+W^- candidates in all the jet multiplicity bins. With jet veto ($E_T^{\text{jet}} > 20 \text{ GeV}$, $|\eta| < 3$), we observed 8 candidate events which is again consistent with MC expectation of ~ 9.7 events (MC only, no scale factor correction). Please note that the MC events used in this analysis are generated with pileup ($< N_{\text{vtx}} > \sim 2$) and reweighted by data in all the MC samples. The electron energy scale correction in data and muon momentum smearing in MC based on the Z mass distributions are included in the analysis. Additional corrections to E_T^{miss} associated with the changes of lepton momenta are also made for the events. These are used both in event selections and efficiency studies using Tag and Probe methods.

| Cuts | $ee + E_T^{\text{miss}}$ | $\mu\mu + E_T^{\text{miss}}$ | $e\mu + E_T^{\text{miss}}$ |
|---------------------------------|--------------------------|------------------------------|----------------------------|
| 2 leptons (SS+OS) | 6096 | 12802 | 134 |
| 2 leptons (OS) | 6057 | 12798 | 126 |
| $M_{\ell\ell} > 15 \text{ GeV}$ | 6044 | 12724 | - |
| Z mass veto | 872 | 1935 | - |
| $E_T^{\text{miss, Rel}}$ cut | 12 | 14 | 39 |
| Njet(0,1,2,3,4,5,>=6) | (1,0,3,6,2,0,0) | (2,2,4,6,0,0,0) | (5,7,10,9,7,1,0) |
| Jet veto (Num. of jet=0) | 1 | 2 | 5 |

Table 35: Event selection cut flow for data collected in 2010 at 7 TeV in the three di-lepton channels. SS denotes same-sign and OS denotes opposite-sign lepton charges.

7.3 Distributions for selected events

Figure 29 shows jet multiplicity distributions for $\ell^+\ell^-E_T^{\text{miss}}$ events. Dots represent data, and stacked histograms are from MC predictions. It is clear that the W^+W^- signature is dominant in the zero-jet bin. To have the best signal-to-background ratio, we applied a jet veto cut in the final W^+W^- event selection. The expected events with jet veto from W^+W^- signal and background are also shown in Table 35.

Figure 32 shows the distributions for W^+W^- candidates: the first row plots are the p_T of leading lepton (left) and the p_T of trailing lepton (right); the second row are the transverse momenta distribution of di-lepton system (left) and the ϕ angle difference between the two leptons (right); the third row is the M_T for the di-lepton+ E_T^{miss} system (left) and p_T for di-lepton+ E_T^{miss} (right). The dots represent data and stacked histograms are from MC predictions.

7.4 W^+W^- signal event selection cut flow and acceptance

Table 36 shows the W^+W^- signal event selection cut flow for three di-lepton channels. The acceptance for prompt electron or muon decay from W 's are treated separately from $WW \rightarrow \tau\nu\ell\nu$. The relative selection efficiencies for each selection step and overall acceptance are given in this Table. No scale factor corrections are applied to the W^+W^- signal acceptance.

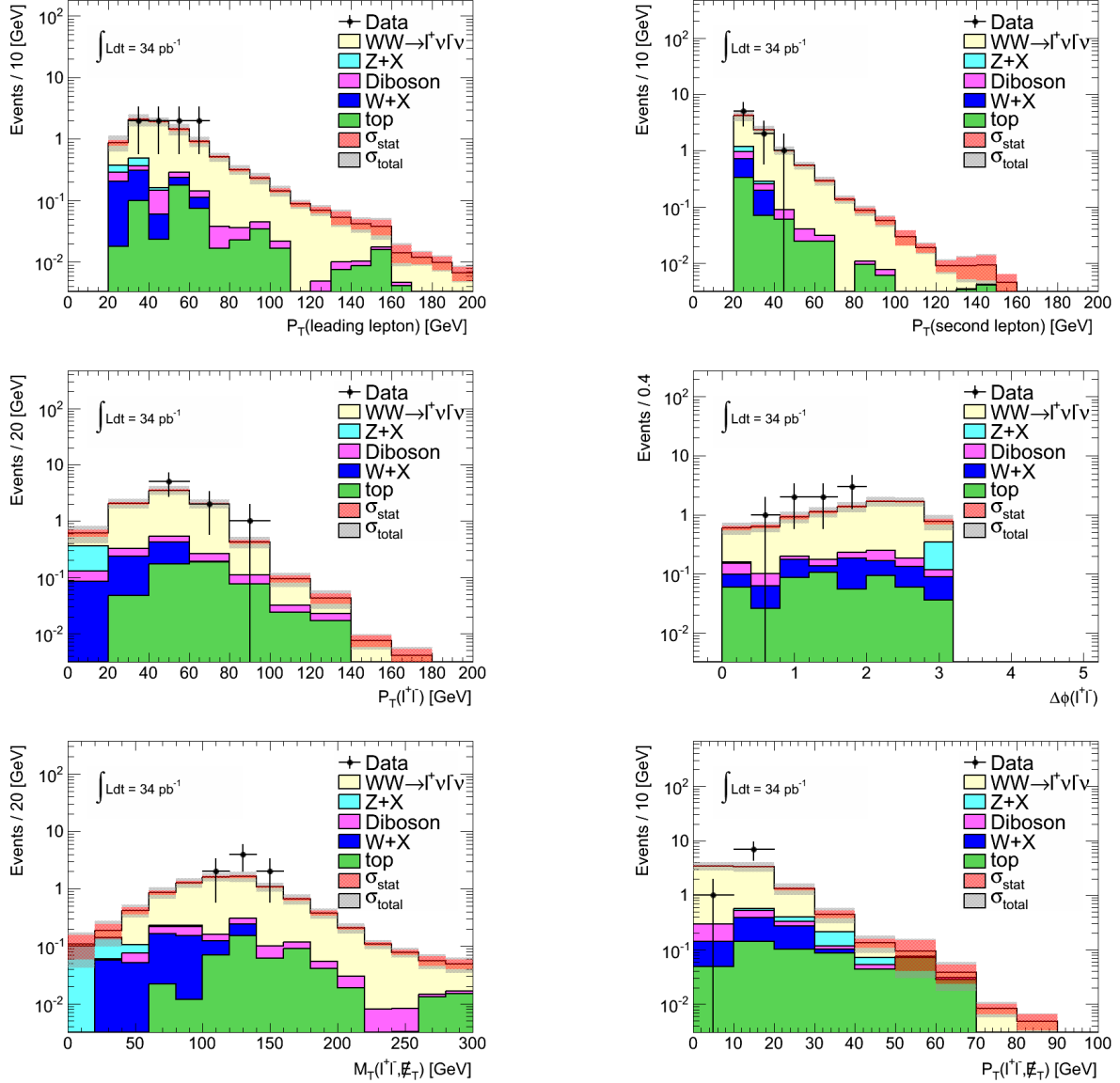


Figure 32: Distributions for W^+W^- candidates for combined ee , $\mu\mu$ and $e\mu$ channels: the first row is the p_T of leading lepton (left) and the p_T of trailing lepton (right); the second row is the $p_T(\ell\ell)$ (left) and the ϕ angle difference between two leptons (right); the third row is the M_T for di-lepton+ E_T^{miss} system (left) and p_T for di-lepton+ E_T^{miss} (right). The dots represent data and stacked histograms are from MC predictions except $W+jets$ background obtained from data-driven methods. Scale factors (described in Section 6.7) are applied to MC. The estimation uncertainties are shown as the red bands (statistic) and grey bands (stat+syst).

| Cuts | <i>ee</i> Channel | | <i>μμ</i> Channel | | <i>eμ</i> Channel | |
|--|-------------------|--------------|-------------------|---------------|-------------------|---------------|
| | <i>eνeν</i> | <i>τνℓν</i> | <i>μνμν</i> | <i>τνℓν</i> | <i>eνμν</i> | <i>τνℓν</i> |
| Total Events | 35516 | 176913 | 35299 | 176913 | 70376 | 176913 |
| 2 leptons (SS+OS) efficiency | 6874 19.4% | 808 0.46% | 14833 42.0% | 1641 0.93% | 20140 28.6% | 2274 1.29% |
| 2 leptons (OS) efficiency | 6835 99.4% | 799 98.8% | 14833 100% | 1640 99.9% | 20061 99.6% | 2263 99.5% |
| $M_{\ell\ell} > 15 \text{ GeV}$ efficiency | 6791 99.3% | 790 98.9% | 14673 98.9% | 1631 99.5% | 20061 - | 2263 - |
| Z mass veto efficiency | 5779 85.1% | 673 85.3% | 12388 84.4% | 1338 82.1% | 20061 - | 2263 - |
| $E_{\text{T}, \text{Rel}}^{\text{miss}}$ cut efficiency | 2362 40.9% | 215 32.0% | 5278 42.6% | 405 30.2% | 13853 69.1% | 1430 63.2% |
| Jet veto (Num. of jet=0) efficiency | 1602 67.8% | 137 63.6% | 3256 61.7% | 233 57.6% | 8837 63.8% | 868 60.7% |
| W^+W^- Acceptance (before SF correction) | 4.51% | 0.08% | 9.22% | 0.13% | 12.56% | 0.49% |
| × SF (Trigger and ID) | 4.24% | 0.075% | 8.81% | 0.12% | 11.91% | 0.46% |
| × SF (Jet Veto) | 4.10% | 0.073% | 8.51% | 0.12% | 11.50% | 0.45% |
| MC Expected Events | 0.74 | 0.08 | 1.53 | 0.15 | 4.18 | 0.45 |

Table 36: W^+W^- MC event selection cut flow, relative selection efficiencies and overall acceptances: before and after scale factor corrections(see Section 6.7). The MC W^+W^- signal expectations are normalized with corrected scale factors and 34 pb^{-1} integrated luminosity, using the cross sections from MCFM with MSTW2008 PDFs.

8 Background estimation with data driven methods

Several data driven methods are developed and applied to the W^+W^- analysis to estimate the $W+\text{jets}$ and Drell-Yan backgrounds. Results obtained by these methods are cross-checked and found to be consistent.

8.1 $W+\text{jets}$ background.

Events in which W bosons are produced in association with QCD jets give rise to background to W^+W^- events when the jet is misidentified as a lepton. The rate at which QCD jets are misidentified as leptons may not be accurately described in the MC, and thus a data-driven method to estimate this background is employed [29, 30]. A description of this method and the $W+\text{jets}$ background prediction is presented in this section.

8.1.1 Data driven $W+\text{jets}$ background estimation

The $W+\text{jet}$ background is estimated from data by defining a selection similar to the W^+W^- signal selection that is enriched in $W+\text{jet}$ events. Events passing this $W+\text{jet}$ enriched selection are used to predict the yield and kinematics of $W+\text{jet}$ events passing the full W^+W^- signal selection by scaling by a “fake factor” that is measured in data.

The $W+\text{jet}$ control sample is defined using an alternative lepton definition that is enriched in QCD jets. Events containing one fully identified lepton, and a jet passing this alternative, “jet-rich” lepton definition are selected. These events are then required to pass the full W^+W^- event selection, where the jet is treated as if it were a fully identified lepton. Events satisfying this selection are enriched in $W+\text{jet}$ events and define the $W+\text{jet}$ control sample. The $W+\text{jets}$ background to W^+W^- is then estimated by scaling the control sample by a measured “fake factor”.

The fake factor is defined in Equation 11 as the ratio of the number of jets satisfying the full lepton identification, to those satisfying the jet-rich lepton selection.

$$f_l \equiv \frac{N_{\text{lepton ID}}}{N_{\text{Jet-Rich ID}}}, \quad (11)$$

The fake factor, f_l , is defined for both electrons and muons, and represents the rate at which QCD jets passing the jet-rich lepton ID are misidentified as leptons passing the full lepton ID. This fake factor is measured in data from di-jet events.

The $W+\text{jet}$ background to W^+W^- is calculated by scaling the number of events in the $W+\text{jet}$ control sample, $N_{\text{lepton ID} + \text{Jet-Rich ID}}$, by the measured fake factor:

$$N_{W+\text{jet Bkg}} = f_l \times N_{\text{lepton ID} + \text{Jet-Rich ID}}. \quad (12)$$

The $W+\text{jet}$ background in the $e-\mu$ channel receives contributions from both misidentified electrons and misidentified muons as shown in Equation 13.

$$N_{W+\text{jet Bkg}}^{e\mu\text{-ch}} = f_e \times N_{\mu \text{ ID} + \text{Jet-Rich } e} + f_\mu \times N_{\text{elec. ID} + \text{Jet-Rich } \mu} \quad (13)$$

The remainder of this section is organized as follows: Section 8.1.2 describes the fake factor calculation and the determination of its systematic uncertainty, Section 8.1.3 presents the $W+\text{jet}$ control region, and Section 8.1.4 presents the $W+\text{jet}$ background estimates.

| Jet-Rich Lepton Definitions | |
|--|---------------------------|
| Electrons | Muons |
| Reconstructed Electron Candidate | STACO Combined Muon |
| $ \eta < 2.47$, outside crack region | $ \eta < 2.4$ |
| Outside regions w/LAr readout problems | - |
| $E_T > 20 \text{ GeV}$ | $p_T > 20 \text{ GeV}$ |
| $ z_0 < 10\text{mm}$ | $ z_0 < 10\text{mm}$ |
| $N_{\text{SCT}}^{\text{hits}} \geq 1, N_{\text{Pixel}}^{\text{hits}} \geq 1$ | |
| $eTCone30 < 6 \text{ GeV}$ | $pTCone20/p_T < 0.5$ |
| Fails full Electron Selection | Fails full Muon Selection |

Table 37: The definition of jet-rich lepton.

8.1.2 Fake factor measurement.

The fake factor depends on the jet-rich lepton definitions. The jet-rich definitions for electrons and muons are given in Table 37.

The fake factors, as defined in Equation 11, are calculated in a jet-triggered data sample. The presence of leptons from on-shell W and Zs in the di-jet sample will bias the calculation of the fake factor. To suppress this contamination, events used in the fake factor calculation are vetoed if they have a W candidate with $m_T > 30 \text{ GeV}$ ⁵ or if they contain two reconstructed electron candidates with an invariant mass within 15 GeV of the Z mass. The remaining W and Z contribution is subtracted from the di-jet sample using the MC prediction. Figure 33 shows the p_T distribution of the jet-rich and fully-identified leptons in the di-jet sample after applying the EW background veto. The di-jet MC sample is normalized to the number of jet-rich objects in the data that pass the L1_J15 trigger. The measured fake factor is shown in Figure 34 as a function of p_T , with and without EW background subtraction.

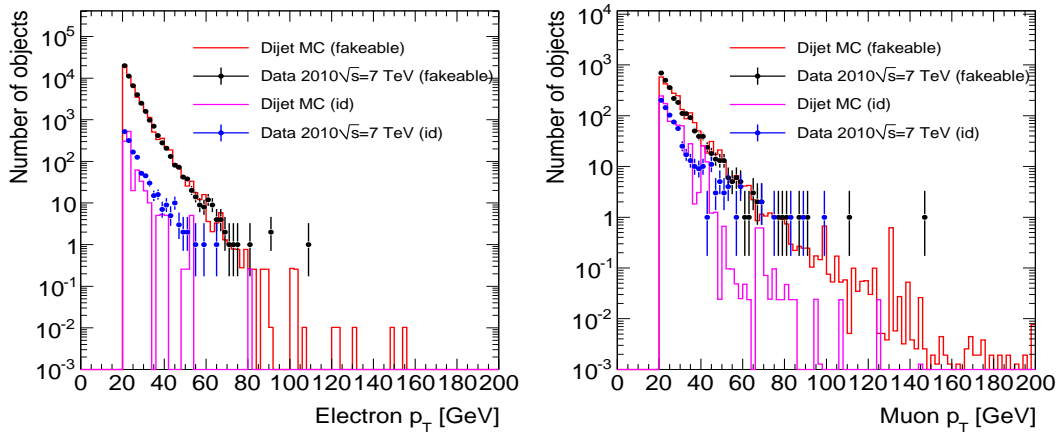


Figure 33: Left: the electron p_T distribution. The di-jet Monte Carlo is normalized to the number of jet-rich leptons in the data passing the L1_J15 and EF_j35_NoEF trigger. Right: the muon p_T distribution.

⁵Here, the transverse mass is defined as $m_T = \sqrt{2P_T^\ell P_T^{\text{miss}} \cdot (1 - \cos \Delta\phi)}$ where P_T^ℓ is the lepton transverse momentum and $\Delta\phi$ the angle between the lepton and the P_T^{miss} directions in the transverse plane.

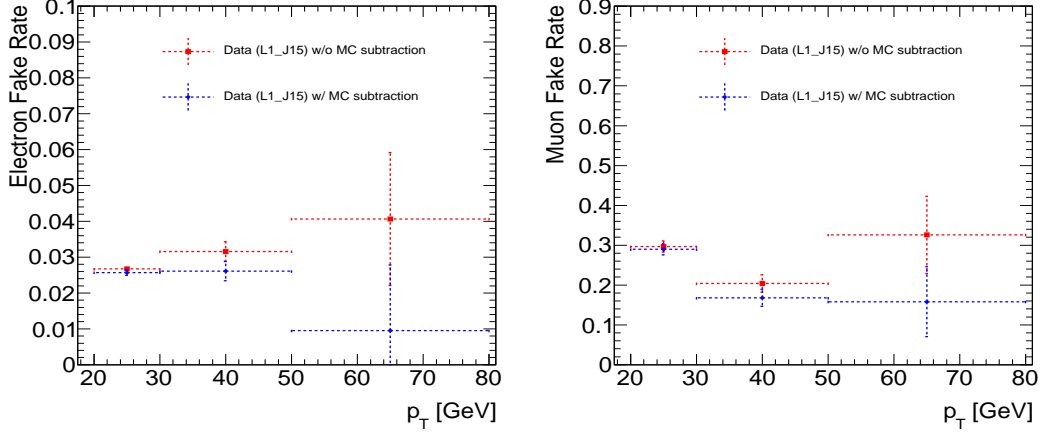


Figure 34: Left(Right): electron (muon) fake factor as a function of p_T . Blue/Red points show the fake factor after/before the EW background subtraction.

The dominant source of systematic uncertainty in the $W+jet$ background prediction comes from the uncertainty in the measured fake factor. Several sources of systematics have been evaluated and will be presented below.

The first source of systematic uncertainty considered is that from the trigger dependence. The fake factor has been measured in different data sets, satisfying different jet triggers. Figure 35 shows the measured fake factors for the different jet triggers in the p_T range between 20 and 30 GeV, where the fake background dominates. A 30% systematic uncertainty is assigned to cover the variation in fake factor among jet-triggered samples.

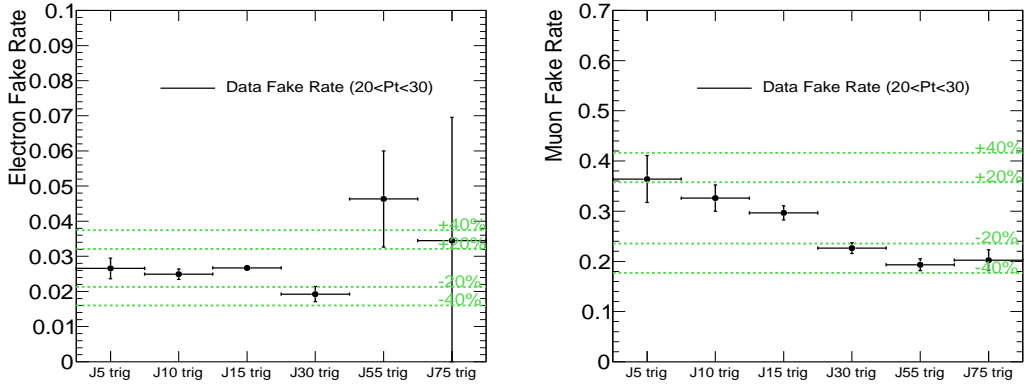


Figure 35: Left: electron fake factor dependence for jet trigger data in the range $20 < p_T < 30$ GeV. The fake factor from the J15 trigger is the central value in this analysis. A $\pm 20\%$, $\pm 40\%$ uncertainty from the central value is shown by the green dashed line.

Another source of systematic uncertainty considered is the stability of the fake factor over the run period. Figure 36 shows the fake factor measured separately for each run period. The majority of the di-jet data were recorded in the earlier run periods due to the high prescales imposed during the later higher-luminosity periods. On the other hand, the majority of the events in the $W+jet$ control region, to

which the fake factor is applied, were recorded during the later runs. A 20% systematic uncertainty is assigned to cover the observed run-to-run differences and any potential luminosity dependent changes in the later runs.

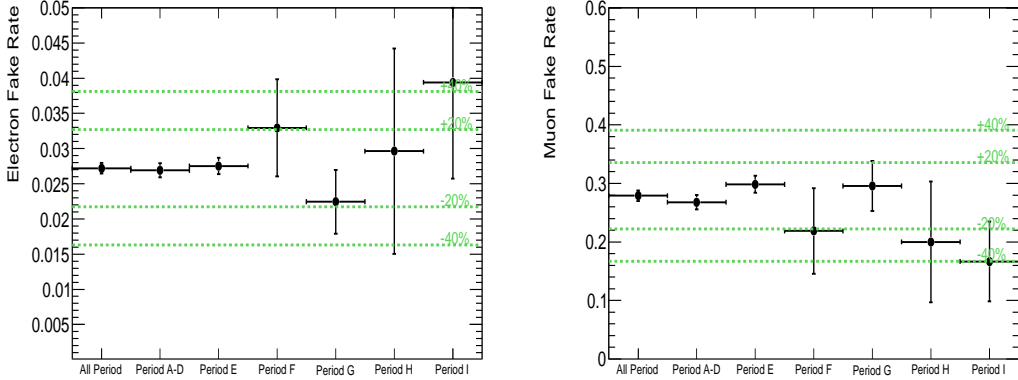


Figure 36: Two plots show the fake factor stability of the J15 trigger for each data period. $A \pm 20\%$, 40% uncertainty from average over the whole period is shown by the green dashed line

The level of real lepton contamination in the di-jet sample leads to another source of systematic uncertainty. The electroweak subtraction from the di-jet sample was performed using MC shapes and theoretical cross sections. There is a systematic uncertainty associated to the theoretical uncertainty of the cross-section, which is at the $\sim 5\%$ level [9]. To evaluate the effect of this uncertainty, the electroweak subtraction is preformed while the cross-section is varied conservatively by $\pm 20\%$. Figure 37 shows the relative differences of fake factors from those obtained at the nominal theoretical cross section. The fake factor systematic from the cross section uncertainty is negligible in this low p_T region.

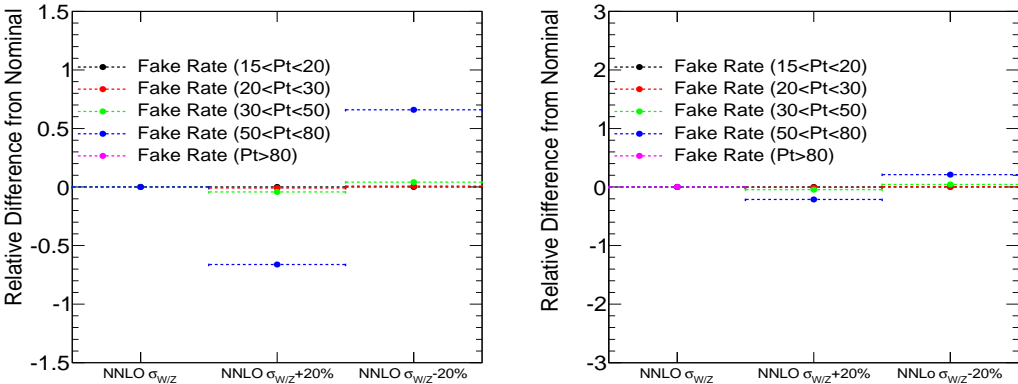


Figure 37: Left (Right): The relative difference of fake factors relative to those at the nominal cross-section for each p_T range. Cross sections were varied by $\pm 20\%$

The final source of systematic uncertainty considered is that from the sample dependence. The fake factor is estimated from a di-jet sample and assumed to apply in a $W+jet$ sample. A systemic uncertainty associated to possible differences between the samples is included. This sample dependence is evaluated

in MC. Figure 38 shows the fake factor of di-jet MC and W +jets MC, excluding the real leptons from W . The fractional difference in the observed fake factor in di-jet Monte Carlo and W +jets Monte Carlo, $f_l^{di-jet} - f_l^{W+jet}/f_l^{di-jet}$ is found to be negligible in the p_T range between 20 and 30 GeV.

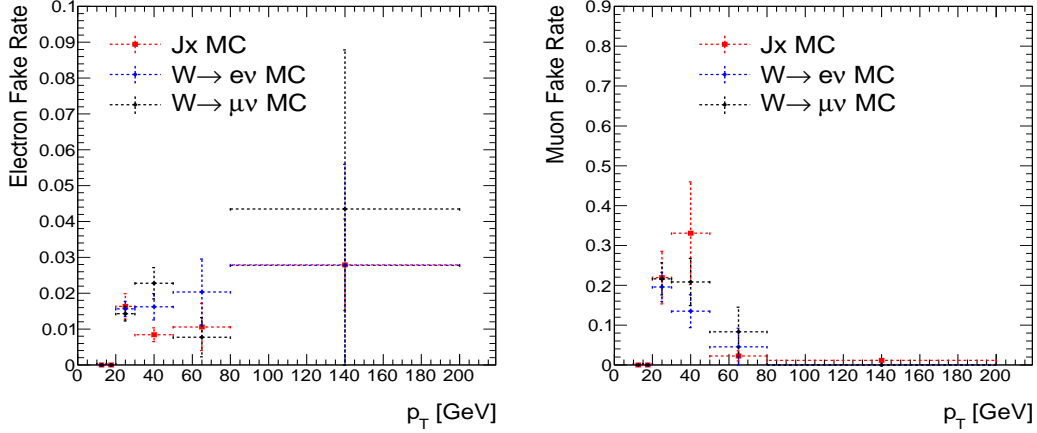


Figure 38: Left: the electron fake factor as a function of electron p_T from di-jet MC sample and W inclusive MC sample. Right: the muon fake factor as a function of muon p_T . Uncertainty shows the MC statistics of samples.

Table 38 shows the summary of systematic uncertainties of the fake factor in the p_T range between 20 and 30 GeV. The total systematic uncertainty of the fake factor is 36% for electrons and 36% for muons. Figure 39 shows the fake factor as a function of p_T after EW subtraction. Each color shows the amount of each systematic uncertainty. In the low p_T region, sample dependence, stability in whole run period and trigger bias are dominant systematics, while statistical uncertainty of multi-jet data is dominates the high p_T region.

| 20 < p_T < 30 GeV | | |
|---------------------------|----------------------|------------------|
| Systematic source | Electron fake factor | Muon fake factor |
| Data statistics | 3.0% | 3.6% |
| Real lepton contamination | Negligible | Negligible |
| Trigger dependence | 30% | 30% |
| Period dependence | 20% | 20% |
| Sample dependence | negligible% | negligible% |
| Total | 36% | 36% |

Table 38: Systematic uncertainty of the fake factor in lepton p_T range between 20 and 30 GeV.

8.1.3 W +jets control regions

In this subsection, the W +jet control regions are presented.

The sample obtained by reversing the opposite-sign lepton requirement in the W^+W^- selection is enriched in W +jet events where the jet is misidentified as a lepton. The fake factor procedure can be applied to the same-sign W +jet control region to predict the yield in the same-sign events in which both

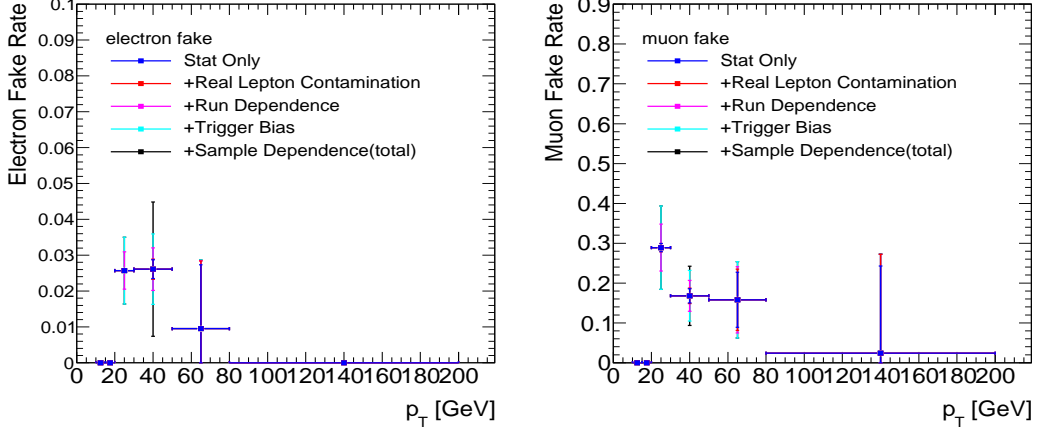


Figure 39: Left (Right): electron (muon) fake factor as a function of p_T including systematic uncertainties.

leptons pass the fully-identified lepton ID, referred to in the following as the same-sign W^+W^- region. This same-sign control region provides a data-driven cross check of the $W+jets$ background procedure.

Table 39 presents the observed data and expected contribution from processes other than $W+jets$ in the same-sign control region. Figure 40 shows kinematic distributions for the same-sign control region. The $W+jet$ MC is normalized to the $W+jets$ yield predicted from data. The observed data distributions are in good agreement with $W+jets$ MC.

Table 40 presents the $W+jet$ yield in the opposite-sign control region. The contribution from non- $W+jet$ processes is larger than for the same-sign region. Figure 41 shows kinematic distributions in the opposite-sign region. The observed data distributions have a good agreement with $W+jets$ MC shapes.

| Channel | Expected contribution from non- $W+jets$ | Observed one ID + one jet-rich events | Predicted $W+jets$ yield from data |
|--------------------------------|--|---------------------------------------|------------------------------------|
| ee-channel | 0.36 | 4 | 3.64 ± 2.00 |
| $\mu\mu$ -channel | 0.005 | 1 | 0.995 ± 1.00 |
| $e\mu$ -channel | 2.50 | 19 | 16.5 ± 4.36 |
| ee+ $\mu\mu$ +e μ -channel | 2.87 | 24 | 21.14 ± 4.90 |

Table 39: Break down of the $W+jet$ yield in the same-sign $W+jet$ control region. Second column is the expected contribution to the control region from non- $W+jets$ processes, the third column is the observed data in the control region, and the last column is the $W+jets$ yield in the control region.

8.1.4 $W+jets$ background prediction.

The $W+jets$ background prediction is obtained by applying the fake factor to the events in the $W+jet$ control region presented in the previous subsection.

Before presenting the background in the W^+W^- signal region, we validate the $W+jets$ method with the same-sign region. Table 41 presents the estimated $W+jets$ contribution from data, the MC estimate of contributions from non- $W+jet$ processes, and the W^+W^- signal contribution to the same-sign W^+W^- control region. The $W+jet$ background prediction is corrected for the non- $W+jet$ contribution to the same-sign $W+jet$ control region. In the same-sign region, the estimated $W+jets$ contribution is

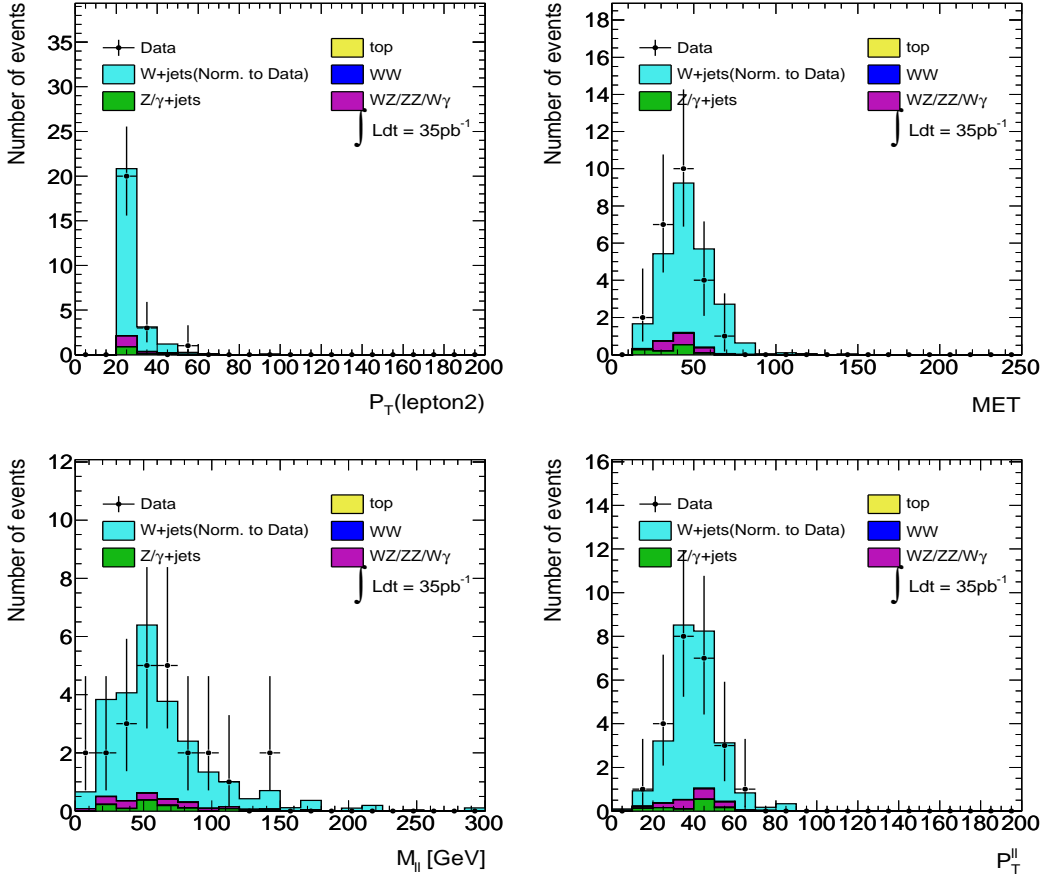


Figure 40: Kinematic distributions of events in the same-sign W +jets control region.

$0.80 \pm 0.28(\text{syst}) \pm 0.31(\text{stat})$. One data event is observed and is consistent with the predicted same-sign yield.

The W +jets background prediction in the W^+W^- signal region is presented in Table 42. The W +jet background prediction is corrected for the non- W +jet contribution to the opposite-sign W +jet control region. The estimated W +jets background is $0.54 \pm 0.21(\text{syst}) \pm 0.32(\text{stat})$ in the opposite-sign signal region.

| Channel | Expected contribution from non- W +jets | Observed one ID + one jet-rich events | Predicted W +jets yield from data |
|-------------------------------|---|---------------------------------------|-------------------------------------|
| ee-channel | 1.03 | 4 | 2.97 ± 2.00 |
| $\mu\mu$ -channel | 0.11 | 0 | 0 |
| $e\mu$ -channel | 4.90 | 23 | 18.10 ± 4.80 |
| $ee + \mu\mu + e\mu$ -channel | 6.2 | 27 | 20.80 ± 5.20 |

Table 40: Break down of the W +jet yield in the opposite-sign W +jet control region. Second column is the expected contribution to the control region from non- W +jets processes, the third column is the observed data in the control region, and the last column is the W +jets yield in the control region.

| Channel | Estimated W +jets from Data | Other Bkg. prediction from MC | WW prediction from MC | Observed data |
|-------------------------------|--|-------------------------------|-----------------------|---------------|
| ee-channel | $0.10 \pm 0.05(\text{stat.}) \pm 0.03(\text{syst.})$ | 0.11 | 0.004 | 0 |
| $\mu\mu$ -channel | $0.29 \pm 0.29(\text{stat.}) \pm 0.10(\text{syst.})$ | 0.06 | 0.001 | 0 |
| $e\mu$ -channel | $0.41 \pm 0.11(\text{stat.}) \pm 0.15(\text{syst.})$ | 0.27 | 0.02 | 1 |
| $ee + \mu\mu + e\mu$ -channel | $0.80 \pm 0.31(\text{stat.}) \pm 0.28(\text{syst.})$ | 0.44 | 0.03 | 1 |

Table 41: Predicted yield in the W^+W^- same-sign region. Second column gives the W +jets data-driven estimate, third column is the expected MC contribution from non- W +jets backgrounds, and the last column gives the expected W^+W^- contribution from MC.

| Channel | Estimated W +jets from Data |
|-------------------------------|--|
| ee-channel | $0.08 \pm 0.05(\text{stat.}) \pm 0.03(\text{syst.})$ |
| $\mu\mu$ -channel | $0 \pm 0.29(\text{stat.}) \pm 0.10(\text{syst.})$ |
| $e\mu$ -channel | $0.46 \pm 0.12(\text{stat.}) \pm 0.17(\text{syst.})$ |
| $ee + \mu\mu + e\mu$ -channel | $0.54 \pm 0.32(\text{stat.}) \pm 0.21(\text{syst.})$ |

Table 42: Estimated W +jets background in the W^+W^- signal region. The overall systematic uncertainty is calculated as quadratic sum of ($ee + e\mu$) and $\mu\mu$

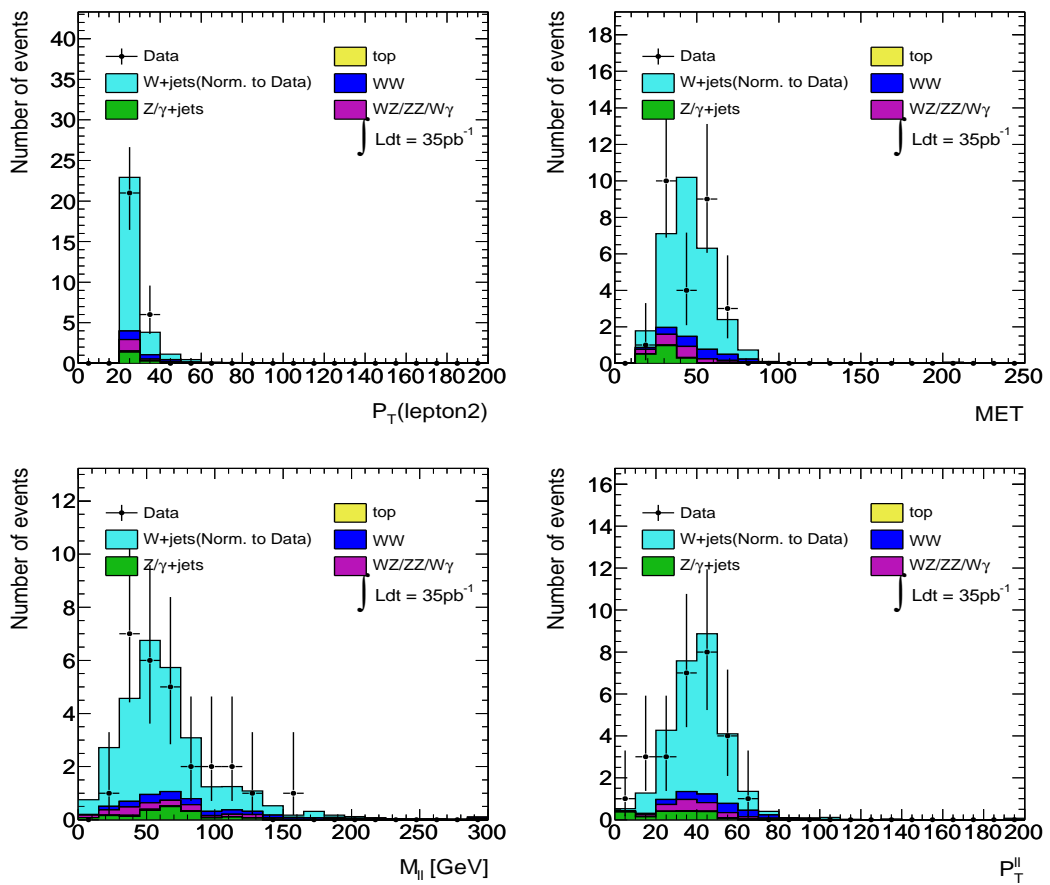


Figure 41: Kinematic distributions of events in the $W+\text{jets}$ opposite-sign region.

8.2 Drell-Yan Background

Drell-Yan events, like W^+W^- events, produce two high p_T leptons. Drell-Yan events are distinguished from W^+W^- events using a $E_{T,\text{Rel}}^{\text{miss}}$ cut of 40 GeV in the ee and $\mu\mu$ channels and 20 GeV in the $e\mu$ channel. In addition, a Z mass window cut of 10 GeV around M_Z is applied to the ee and $\mu\mu$ channels to remove the bulk of $Z \rightarrow \ell\ell$ events. However, the Drell-Yan E_T^{miss} distribution has a tail that extends to high E_T^{miss} . Using $E_{T,\text{Rel}}^{\text{miss}}$ reduces the tail from mis-measured leptons, but a small probability remains to include Drell-Yan in the signal. Additionally in $Z \rightarrow \tau\tau$ events having zero jets, the two τ leptons are back-to-back. This causes the real E_T^{miss} from the τ decays to be small and aligned with a lepton leading to small $E_{T,\text{Rel}}^{\text{miss}}$ in the event. For this reason, the source of large $E_{T,\text{Rel}}^{\text{miss}}$ in all three channels is the same, being principally attributed to the E_T^{miss} resolution and pileup effects. Given the large relative cross section of Drell-Yan events, they contribute a non-negligible background to the W^+W^- signal. Monte Carlo simulation of Drell-Yan events reproduces a large $E_{T,\text{Rel}}^{\text{miss}}$ tail. However, an accurate prediction of the Drell-Yan background from Monte Carlo requires correct simulation of detector response and particle multiplicity at a level of 3 orders of magnitude below the core of the distribution. The central value of the Drell-Yan background is determined from Monte Carlo and a partially data driven method has been used to evaluate the systematic uncertainty. The method applies a systematic determined by the discrepancy between data and Monte Carlo within the Z peak.

8.2.1 Comparison of Monte Carlo Generators

For this study, the ALPGEN Monte Carlo generator is used for the $Z/\gamma^* \rightarrow ee$ and $Z/\gamma^* \rightarrow \mu\mu$ events and PYTHIA is used for $Z/\gamma^* \rightarrow \tau\tau$ events due to a mis-modelling of tau decays in ALPGEN. Low $M_{\ell\ell}$ (10 GeV < $M_{\ell\ell}$ < 40 GeV for ALPGEN, 10 GeV < $M_{\ell\ell}$ < 60 GeV for PYTHIA) and high $M_{\ell\ell}$ ($M_{\ell\ell} > 40$ GeV for ALPGEN, $M_{\ell\ell} > 60$ GeV for PYTHIA) Monte Carlo samples are simulated separately and combined to determine the Drell-Yan event yields. Samples are weighted by the parameters in Table 4. The predictions for each Monte Carlo generator are shown in Table 43. Where the Monte Carlo predicts zero events, the statistical uncertainty applied is the 68% confidence level upper limit assuming a Poisson distribution: 1.15 events. The event weight, 0.09, multiplied by 1.15 gives the 0.10 statistical uncertainty. In the $\mu\mu$ channel of the ALPGEN results, the low $M_{\ell\ell}$ sample provides the only Monte Carlo event that passes. Because the high $M_{\ell\ell}$ sample has a much larger acceptance than the low $M_{\ell\ell}$ sample, also here the statistical uncertainty is applied based on 1.15 high $M_{\ell\ell}$ events.

Drell-Yan events were also generated using MC@NLO. Only large $M_{\ell\ell}$ ($M_{\ell\ell} > 60$ GeV) MC@NLO samples were generated. The variation in the Drell-Yan signal selection yields from the three generators (see Table 43) shows good agreement with the data driven background uncertainty. The general normalization of the Drell-Yan Monte Carlo is tested by comparing event yields in a Drell-Yan rich region. In the ee and $\mu\mu$ channels, the normalization is performed using events passing the full signal selection except the $E_{T,\text{Rel}}^{\text{miss}}$ cut and having an invariant mass within 10 GeV of the PDG Z mass, reversing the standard Z mass exclusion cut. For the $e\mu$ channel, the control region requires the full signal selection except the $E_{T,\text{Rel}}^{\text{miss}}$ cut and requiring $E_{T,\text{Rel}}^{\text{miss}} < 10$ GeV. In the control regions for all three channels the Monte Carlo prediction is consistent with data within uncertainties. Since there is good agreement between data and Monte Carlo in the $e\mu$ control region, no additional scaling is applied and allows the systematic uncertainty determined in the ee and $\mu\mu$ channels to be applied to the $e\mu$ channel.

8.2.2 Systematic Uncertainty Estimate

A partially data driven method has been used to determine the uncertainty on the Drell-Yan background. The method uses the observed discrepancy between the $E_{T,\text{Rel}}^{\text{miss}}$ distributions in data and Monte Carlo within the Z peak region and applies that discrepancy as a systematic to the background predicted from

| Generator | ee | $\mu^+\mu^-$ | $e\mu$ | combined |
|-----------|--------------------------|--------------------------|--------------------------|--------------------------|
| ALPGEN | $0.00 \pm 0.10 \pm 0.07$ | $0.01 \pm 0.10 \pm 0.07$ | $0.22 \pm 0.06 \pm 0.15$ | $0.23 \pm 0.15 \pm 0.17$ |
| MC@NLO | $0.02 \pm 0.01 \pm 0.01$ | $0.06 \pm 0.02 \pm 0.04$ | $0.27 \pm 0.07 \pm 0.18$ | $0.35 \pm 0.07 \pm 0.18$ |
| PYTHIA | $0.00 \pm 0.01 \pm 0.01$ | $0.05 \pm 0.02 \pm 0.03$ | $0.24 \pm 0.06 \pm 0.16$ | $0.29 \pm 0.07 \pm 0.16$ |

Table 43: Predicted Drell-Yan contribution in the signal region of the ee , $\mu\mu$, and $e\mu$ channels for three Monte Carlo generators. Entries are in the form of value \pm stat \pm syst uncertainties. The reported systematic uncertainty is derived from the data driven estimate in 8.2.2

Monte Carlo. The method assumes that the mechanism that causes a discrepancy between data and Monte Carlo is independent of the invariant mass of the sample. Additionally its is assumed that any discrepancy between data and Monte Carlo is caused by a mis-modelling of the Drell-Yan sample. The assumption is justified because all other backgrounds to W^+W^- have real missing energy whereas Drell-Yan can only obtain large $E_{T, Rel}^{\text{miss}}$ through fluctuations in detector resolution. For this method leptons are selected as described in the object selection section. After the Data-Quality, trigger, vertex, and E_T^{miss} cleaning requirements are made, events are selected inside the Z mass window ($|M_{\ell\ell} - M_Z| < 10\text{GeV}$). The jet veto is also applied. This selection provides a large sample of Drell-Yan events having relatively little W^+W^- signal contamination. The data are then compared to the full Monte Carlo prediction. Figure 42 shows the $E_{T, Rel}^{\text{miss}}$ distributions for data and Monte Carlo. Assuming that any discrepancy between data and Monte Carlo arises from Drell-Yan mis-modelling of the E_T^{miss} distribution, the discrepancy is quantified as

$$S = \frac{N_{Data}(E_{T, Rel}^{\text{miss}} > 30\text{GeV}) - N_{MC}(E_{T, Rel}^{\text{miss}} > 30\text{GeV})}{N_{DY}(E_{T, Rel}^{\text{miss}} > 30\text{GeV})} \quad (14)$$

Where N_{Data} is the number of data events, N_{MC} is the number of events predicted by the sum of all Monte Carlo samples and N_{DY} is the number of events predicted by the Drell-Yan Monte Carlo alone. A $E_{T, Rel}^{\text{miss}}$ cut of 30 GeV is used because no data exist in the Z window above $E_{T, Rel}^{\text{miss}} = 35\text{GeV}$. Since a 30 GeV cut already selects events well on the tails of the $E_{T, Rel}^{\text{miss}}$ distribution, it is assumed that the result obtained with this cut value is applicable to the analysis cut value of 40 GeV. Using the distributions from Figure 42, the relevant quantities from Equation 14 are shown in the table below,

| Channel | N_{Data} | N_{MC} | N_{DY} | S |
|----------|------------|-----------------|-----------------|------------------|
| ee | 2 | 2.89 ± 0.43 | 2.4 ± 0.42 | -0.38 ± 0.61 |
| $\mu\mu$ | 5 | 5.97 ± 0.62 | 4.88 ± 0.61 | -0.20 ± 0.47 |

For both channels the S value is negative indicating that the Monte Carlo over estimates the data. Since the S values are providing a handle on the amount by which Monte Carlo disagrees with data, the absolute values are used. The two channels are combined in a weighted average to give a prediction of 0.27 ± 0.37 . Both the S value and its uncertainty are sensitive to the discrepancy, so as a conservative estimate the value and its error are added linearly to give a final background uncertainty of 64%.

The uncertainty as obtained from the ee and $\mu\mu$ channels is applied to the $e\mu$ channel. This is conservative estimate because the Monte Carlo is expected to better predict real E_T^{miss} from τ decays. In order for the value to apply, the $E_{T, Rel}^{\text{miss}}$ distributions must be similar between the $e\mu$ channel and the ee and $\mu\mu$ channels. Figure 43 shows that the shapes agree well between the same flavor and $e\mu$ channels. The presence of a small slope in the ratio plot indicates that the $e\mu$ channel tends to have lower $E_{T, Rel}^{\text{miss}}$ than the ee or $\mu\mu$ channels. In this case, applying the systematic determined from the same flavor channels is an over estimate of the systematic for the $e\mu$ channel.

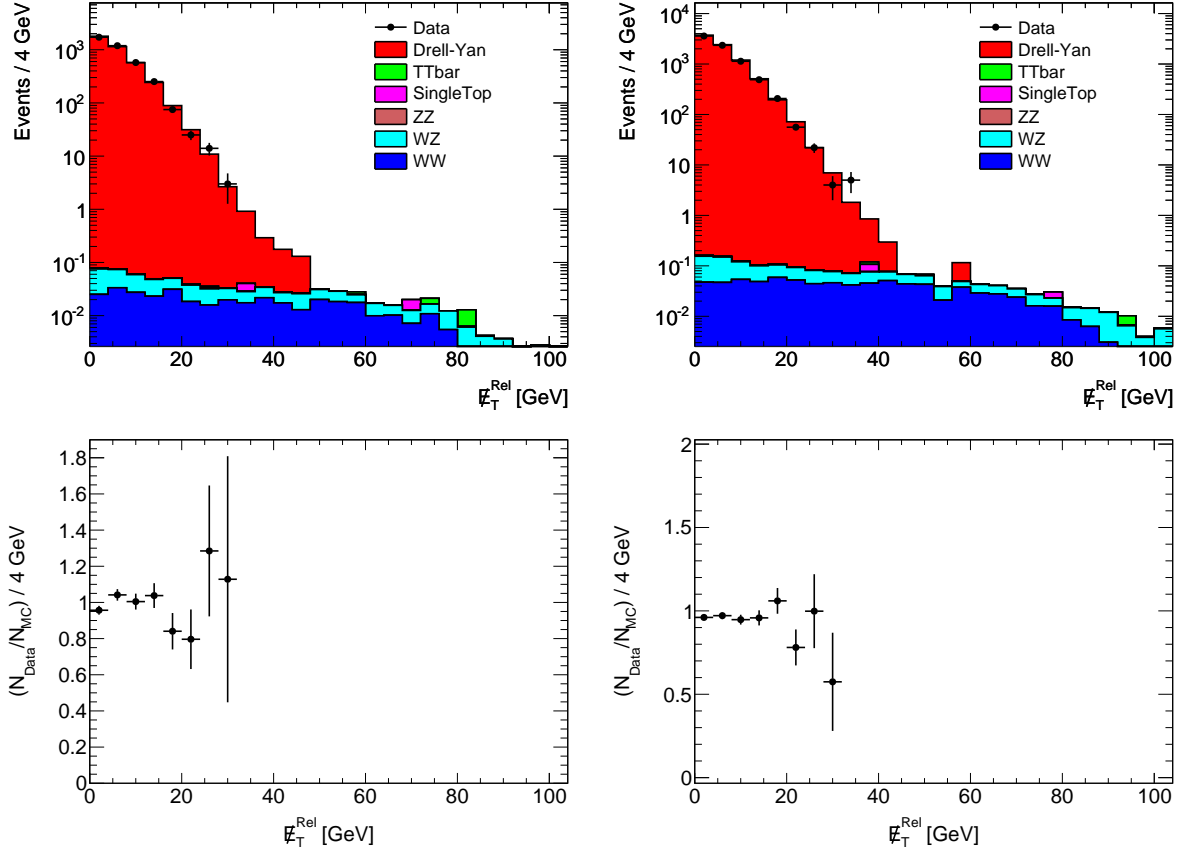


Figure 42: Missing energy distribution for data and Monte Carlo for events selected within the Z mass window for the electron channel (left) and muon channel (right). The bottom plots show the ratio of data to Monte Carlo

The central value of the Drell-Yan background is taken from ALPGEN Monte Carlo. Where the Monte Carlo has zero events in the signal region, an upper limit is used. The predicted backgrounds used in this analysis are shown in the ALPGEN results of Table 43.

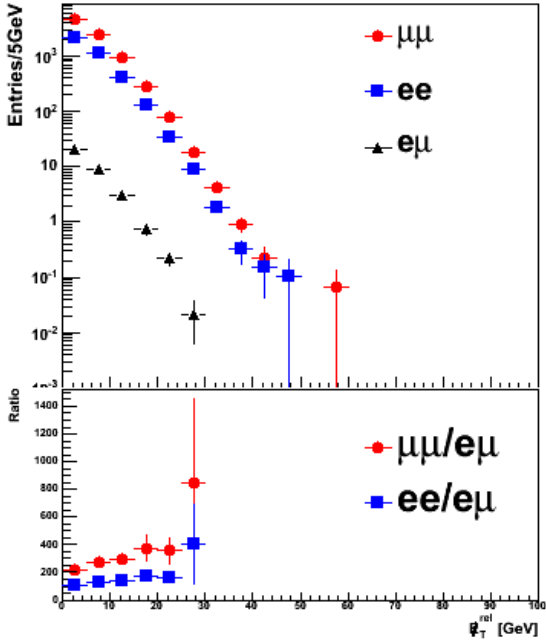


Figure 43: Comparison of the $E_{T, \text{Rel}}^{\text{miss}}$ distributions between ee , $\mu\mu$, and $e\mu$ channels. The bottom plot is a ratio of ee to emu and $\mu\mu$ to emu

8.3 Background from cosmic muons

In rare cases, cosmic muons which appear to have large momentum can cause the muon trigger to fire, and subsequently be reconstructed as two separate muons originating from the interaction region. If the cosmic muon track intersects a hadronic interaction, this event could in principle look like a signal event. In previous studies [31], the cosmic background was estimated as follows:

During low-luminosity running with 8 bunches in collision, the L1_MU0 trigger item was triggered at about 4 Hz. Given the LHC frequency, one can calculate that the probability of a cosmic muon triggering L1_MU0 in coincidence with a collision is at most $4.4 \cdot 10^{-5}$. In these studies cosmic muon events in empty bunches were then used to set an upper limit on the cosmic background. For this analysis, excluding a cosmic contribution to the final selection with this method would require about 80 million recorded cosmic muon events, due to the integrated luminosity of 34 pb^{-1} . The cross-section of minimum bias events is on the order of 50mb, therefore 34 pb^{-1} correspond to $1.8 \cdot 10^{12}$ minimum bias collisions. With a pileup of two collisions per bunch crossing, this leads to approximately 40 million triggers of L1_MU0 from cosmic muons.

Since only about one million cosmic events during beam were recorded in 2010, we use characteristic features of cosmic muon events to exclude contamination. The main characteristics of cosmic muon events are that the two reconstructed muons are back-to-back, not only in the phi plane $\Delta\phi = \pi$ but also in pseudorapidity $\eta_1 + \eta_2 = 0$.

Using cosmic muon events recorded by a special trigger during empty bunch crossings, the distribution of $\Delta\phi$ and $\eta_1 + \eta_2$ for muons that pass the quality cuts were acquired. Using these distributions one can derive a 3σ interval for both variables, in which 99.7% of the cosmic muons are expected. This box was found to be $|\eta_1 + \eta_2| < 0.0033$ and $\Delta\phi > 3.14$. Only 2 out of the 12798 events with two muons with

opposite sign were found in this range before any selection cuts, with no events surviving to the final selection. This indicates that background to this analysis due to cosmic muons is negligible.

8.4 Top Background

The decay products from both top-pair ($t\bar{t} \rightarrow WbWb$) and single top ($tW \rightarrow WbW$) processes contain W^+W^- in final states. The top events are characteristic by hadronic jet activities in final states. Using jet-veto cut the majority of the top background can be removed from the W^+W^- event selection. However, some top events containing jets with transverse energy E_T^{jet} less than 20 GeV would still mimic the SM W^+W^- events. The top background estimation is estimated using MC simulations. The results obtained by MC simulation are cross checked by using data driven methods. Method A uses jet multiplicity control regions to estimate the top contribution in zero jet bin; Method B uses a top control sample with b -tagging to estimate the top contribution. Details are presented in this section.

8.4.1 Top Background Estimation from MC

The MC simulations include Top pair production ($t\bar{t}$) and single Top production. The simulated events and MC predicted cross-sections for these processes are shown in Table 5. The lepton (electron and muon) energy/momentum scales and resolutions are re-smeared in the MC based on calibration using $Z \rightarrow \ell^+\ell^-$ events. The W^+W^- selection cuts are applied to the Top MC events including jet-veto. The Top background contamination in W^+W^- sample is estimated using the survived MC Top events which are normalized to the SM cross-sections with 34 pb^{-1} integrated luminosity. The expected Top background from MC expectations (after SF correction) are 0.04 ± 0.02 for the ee channel, 0.14 ± 0.06 for the $\mu\mu$ channel and 0.35 ± 0.10 for the $e\mu$ channel. The results are listed in the Table 55. The total Top background estimated from MC simulations is $0.53 \pm 0.12 \text{ (stat)} \pm 0.28 \text{ (syst)}$ after scale factor correction.

The sources of the systematic uncertainties for Top background are listed in Table 52. The luminosity uncertainty measured with van der Meer scans is 3.4% as shown in Table 48. Theoretical uncertainty on $t\bar{t}$ cross section is 12% ref [32]. We have assumed the same uncertainty for single Top background. One of the major systematic uncertainties for Top background comes from the effect of jet energy scale uncertainty on jet veto cut, which is determined to be 40% in Section 6.3.1. The other major systematic uncertainty comes from the Initial State Radiation (ISR) and Final State Radiation (FSR), which is estimated to be 32% in Section 8.4.2.

The systematic uncertainties on triggers and lepton ID efficiencies is described in Table 49. Electron and muon channels are calculated separately. Muon Pt scale and resolution smearing do not directly change the muon acceptance, so it's not counted in acceptance uncertainty. The pileup vertex re-weighting effect for Top background is relatively small, the uncertainty is estimated by calculating the changes with and without vertex re-weighting. The total systematic uncertainty is a linear sum of the three channels.

8.4.2 Initial and Final State Radiation of Top

The effect of ISR/FSR variation on the Top acceptance is studied using the AcerMC [33] generator interfaced to PYTHIA, and varying the parameters controlling ISR and FSR in a range consistent with experimental data [34]. The Monte Carlo samples and the parameters varied to increase and decrease the ISR and FSR are described in [35]. The dataset ID for the default sample is 105205, and the dataset IDs for ISR/FSR variations are 117255-117260. The kinematic distributions of these MC datasets can be found in [36]. The variables used for the ISR/FSR variation are: PARP(64), PARP(67), PARP(72) and PARJ(82). The variation of PARP(64) corresponds to a variation in $1/(\Lambda_{QCD}^{ISR})^2$, PARP(67) controls the maximum parton virtuality in space-like parton showers, PARP(72) is Λ_{QCD}^{FSR} and PARJ(82) is the FSR infra-red cutoff.

Figure 44 shows the jet multiplicity distributions for each ISR/FSR variation. ISR and FSR have opposite effects on the jet multiplicity. An enhancement of ISR can lead to radiation of hard partons

with a hard recoil from Top system, thereby increasing jet multiplicity. An FSR parton carries away momentum from the final state partons, hence making the jet momenta softer and possibly failing the jet E_T threshold. The result is a reduction of jet multiplicity. Varying both ISR/FSR simultaneously sort of cancels the jet multiplicity variation effects. Table 44 summarizes the fractional acceptance difference due to different ISR/FSR variations. To avoid overestimating the systematic uncertainty due to limited MC statistics, the uncertainty of ISR/FSR variation is evaluated from two samples with both ISR/FSR variations up or down. The ISR/FSR uncertainty in the 0 jet bin, $7 \pm 25\%$, is calculated by symmetrizing the variations from last two rows. The final ISR/FSR systematic uncertainty of Top, 32% is determined to be the one sigma statistical upward fluctuation from the symmetric uncertainty. Note that the assumption of the same uncertainty for both single-top and top-pair production has been made.

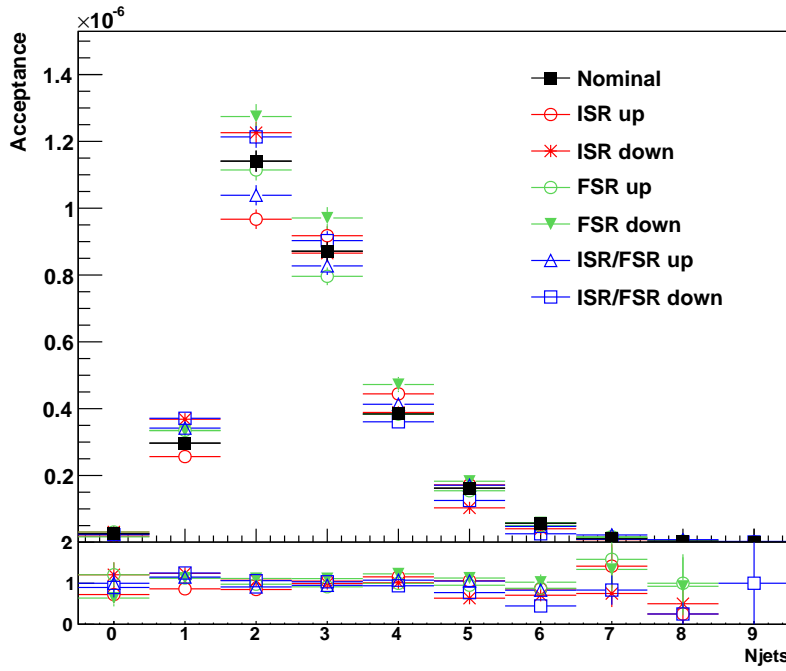


Figure 44: The jet multiplicity distribution of $t\bar{t}$ production after WW event selection except jet veto requirement. The ISR/FSR upward variation increase/decrease the jet multiplicity.

8.4.3 Top background estimation from data using events with large jet multiplicity (Method A)

The Top events are dominated at high jet multiplicity region as shown in Figure 29. In order to estimate the Top background at the 0-jet bin, we use events with jet multiplicity ($N_{jet} = 2\&3$ and $N_{jet} \geq 4$) as two independent control samples and the small other background contribution in the control samples is subtracted using the estimations described elsewhere in the note. The basic idea is to determine the Top background in the 0-jet bin in data by scaling the corresponding MC predicted contribution with the ratio of data over the Top MC events in the control region

$$N_{Top}^{\text{Estimated}}(N_{jet} = 0) = N_{Top}^{\text{MC}}(N_{jet} = 0) \times \frac{N_{\text{data}}(\text{control region})}{N_{Top}^{\text{MC}}(\text{control region})} \quad (15)$$

so that the determination is less sensitive to potentially large theoretical uncertainty on the prediction

| | 0jet | 1jet | 2jet | 3jet | 4jet |
|--------------|--------------|---------------|---------------|--------------|---------------|
| ISR down | 21 ± 30 | 24 ± 9.1 | 8 ± 4.2 | -1 ± 4.5 | -12 ± 4.8 |
| ISR up | -28 ± 21 | -14 ± 6.9 | -15 ± 3.5 | 5 ± 4.7 | 11 ± 5.8 |
| FSR down | -43 ± 18 | 1 ± 8 | 0 ± 4.1 | 0 ± 4.6 | 7 ± 5.8 |
| FSR up | 20 ± 30 | 13 ± 8.5 | -2 ± 3.9 | -9 ± 4.2 | -1 ± 5.3 |
| ISR/FSR down | -14 ± 23 | 25 ± 9.2 | 6 ± 4.1 | 3 ± 4.6 | -15 ± 4.7 |
| ISR/FSR up | 0 ± 26 | 15 ± 8.6 | -9 ± 3.7 | -5 ± 4.3 | 8 ± 5.6 |

Table 44: Fractional acceptance difference [%] with respect to the nominal AcerMC top-pair production. The final ISR/FSR systematic, 32%, for the 0jet selection is evaluated by symmetrizing the uncertainty in the sample of varying both ISR/FSR up and down and taking the large statistical uncertainty into account.

of the Top production. Using this semi-data driven method, we obtain the following estimations of the Top background in the 0-jet bin

$$N_{\text{Top}}^{\text{Estimated}}(N_{\text{jet}} = 0) = \begin{cases} 0.55 & (\pm 0.10) & (\pm 0.03) & (^{+0.17}) & (^{+0.28}) & \pm 0.19 & (N_{\text{jet}} = 2 \& 3) \\ 0.52 & (^{+0.20}) & (\pm 0.01) & (^{+0.16}) & (^{+0.41}) & \pm 0.22 & (N_{\text{jet}} \geq 4) \\ -0.17 & & & -0.11 & -0.28 & & \end{cases} \quad (16)$$

where the first uncertainty is statistical, the other uncertainties are due to those of the background subtraction (assumed conservatively to be 100%), of $N_{\text{Top}}^{\text{MC}}(N_{\text{jet}} = 0)$, of the jet E_T threshold variation ($\pm 10\%$) and of initial and final state radiation setting variations. This method is not sensitive to the luminosity uncertainty and all other global normalization uncertainties because of the ratio $N_{\text{Top}}^{\text{MC}}(N_{\text{jet}} = 0)/N_{\text{Top}}^{\text{MC}}$ (control region).

8.4.4 Top background estimation from data using a b -tagged control sample (Method B)

In this section a method to extract the jet veto efficiency, the fraction of top events that pass a full-jet veto, is described. One considers the extraction of the jet veto efficiency of top background from a control sample that comprises two high transverse momentum leptons, missing transverse energy and a b -tagged hadronic jet. The experimental full-jet veto efficiency for the top background, P_2^{Data} , is expressed as the square of the veto efficiency in data events with at least one b -tagged jet, $P_1^{\text{Btag,Data}}$ ⁶, multiplied by a correction calculated with MC:

$$P_2^{\text{Data}} = \left(P_1^{\text{Btag,Data}} \right)^2 \frac{P_2^{\text{MC}}}{\left(P_1^{\text{Btag,MC}} \right)^2} \quad (17)$$

where P_2^{MC} and $P_1^{\text{Btag,MC}}$ are the corresponding quantities in MC. The final prediction relies on the rate of top events observed in data:

$$N_{\text{Top}}^{\text{Data}}(\ell\ell + E_{\text{T}}^{\text{miss}}, 0j) \approx N_{\text{Top}}^{\text{Data}}(\ell\ell + E_{\text{T}}^{\text{miss}}) \left(P_1^{\text{Btag,Data}} \right)^2 \frac{P_2^{\text{MC}}}{\left(P_1^{\text{Btag,MC}} \right)^2}, \quad (18)$$

where $N_{\text{Top}}^{\text{Data}}(\ell\ell + E_{\text{T}}^{\text{miss}}, 0j)$ and $N_{\text{Top}}^{\text{Data}}(\ell\ell + E_{\text{T}}^{\text{miss}})$ are the number of predicted top background events after the application of a full jet veto and the number of top background events observed in data without

⁶In events with two leptons, met and at least one b-tag, is the ratio of the number of events without extra jets (in addition to the tagging b-jet) and the total number of events.

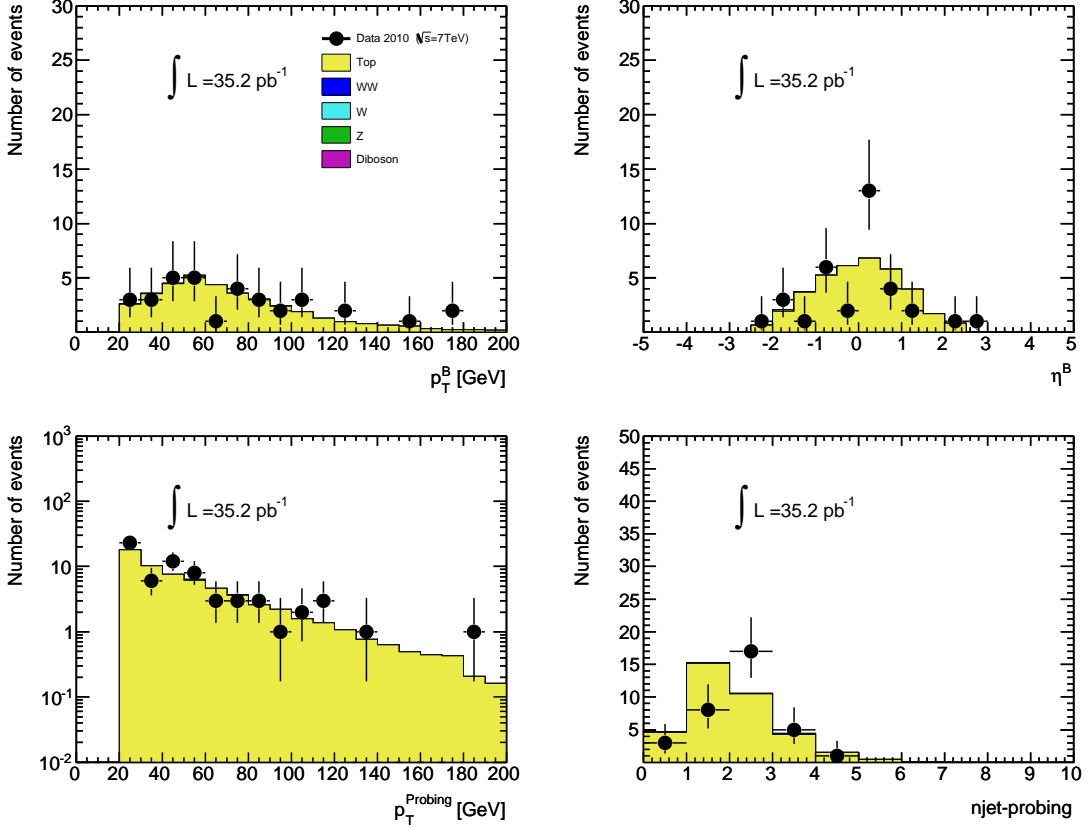


Figure 45: Jet distributions in data compared to MC in the b -tagged control sample. The upper plots display the transverse momentum (left) and pseudo-rapidity (right) of the b -tagged jets. The lower plots display the transverse momentum (left) and the multiplicity of the probing jets (right). The data is compared with MC corresponding to the most relevant processes (see text).

the application of any requirements on the jet multiplicity in the final state, respectively. The extraction of processes not related to top backgrounds for the measurement of $N_{Top}^{Data}(\ell\ell + E_T^{\text{miss}})$ is implied (these backgrounds were subtracted from the data yield using their MC values). In this formula, uncertainties related to the luminosity measurement and the residual theoretical uncertainties of the total cross-section of top processes cancel out. Figure 45 displays a few relevant distributions in data and MC pertaining to the control sample with at least one b -jet. The tagging b -tagged is defined as the b -jet with the largest SV0 weight in the event. Probing jets are defined as the rest of the jets in the event. The data is compared with MC corresponding to the most relevant processes: top ($t\bar{t}$, single top), continuum W^+W^- , W +jets and Z +jets. The sample with at least one b -jet is dominated by top events. The distributions relevant to the b -tagged jets and the rest of the jet activity have been checked. Overall, the MC describes reasonably well the data.

The following systematics are taken into account in the measurement of $N_{Top}^{Data}(\ell\ell + E_T^{\text{miss}}, 0j)$:

- Statistics in the b -tagging control sample in the data, $\approx 100\%$.⁷
- Systematics of the normalisation of $Z \rightarrow \tau^+\tau^-$ and the continuum W^+W^- production in the b -tagging control sample, negligible.

⁷This estimate is obtained with Poisson errors.

| $P_1^{Btag,Data}$ | $P_1^{Btag,MC}$ | $(P_1^{Btag,MC})^2 / P_{2,MC}$ | $N_{Top}^{Data}(\ell\ell + E_T^{\text{miss}})$ | $N_{Top}^{Data}(\ell\ell + E_T^{\text{miss}}, 0j)$ | $N_{Top}^{MC}(\ell\ell + E_T^{\text{miss}}, 0j)$ |
|------------------------|-----------------|--------------------------------|--|--|--|
| $0.09^{+0.09}_{-0.05}$ | 0.13 | 1.53 ± 0.26 | 50.7 ± 8.6 | $0.25^{+0.50}_{-0.25}$ | 0.55 |

Table 45: Summary of results for the jet veto efficiency used for the prediction of the number of top background events in the W^+W^- signal-like region (see text).

| Method | MC | Method A | Method B |
|------------|-----------------|---|------------------------|
| Prediction | 0.53 ± 0.12 | 0.55 ± 0.10 ($N_{\text{jet}} = 2 \& 3$) $0.52^{+0.20}_{-0.17}$ ($N_{\text{jet}} \geq 4$) | $0.25^{+0.50}_{-0.25}$ |

Table 46: Summary of top background extraction results. Results are shown in terms of the total expected number of events for the integrated luminosity of all the data taking periods. The errors are statistics only in the table. For the final results, we use the MC central value for top background estimation.

- The impact of jet energy scale uncertainty is $\approx 30\%$.
- Statistics of the dilepton+ E_T^{miss} normalising control sample, $\approx 10\%$.

This list of systematics leads to a total of $\approx 100\%$ error on the measurement of $N_{Top}^{Data}(\ell\ell + E_T^{\text{miss}}, 0j)$. The results are shown in Table 45.

8.4.5 Summary of top background estimates

In this section we summarize the estimation of the top backgrounds with three different approaches: MC estimation, a data sample with large jet multiplicity (Method A) and a data sample with a b -jet tag (Method B). The three methods yield results that agree within the errors (see Tab. 46). The estimate from MC is used for the extraction of the W^+W^- signal.

9 Systematics

The systematic uncertainties of theoretical cross-sections related to this analysis are given in Table 47. These uncertainties affect the MC signal and background expectation calculations, which will be described in this section.

The luminosity uncertainty measured with van der Meer scans is 3.4% as shown in Table 48. Systematic uncertainty studies for W^+W^- analysis (signal acceptance and background estimation) have already been described in the related sections of this paper. The systematic uncertainties for signal acceptance are given in Table 49. Based on this table, the overall signal acceptance uncertainty is $\sim 7.4\%$, which is calculated as the quadratic sum of the weighted average lepton acceptance uncertainties of three dilepton channels ($\sim 7.3\%$) and acceptance uncertainty due to PDF uncertainties (1.2%, see Appendix E). The systematic uncertainty for W^+W^- signal expectation is around 9.8%, which is calculated in Table 54. In addition to lepton detection uncertainties, other systematic uncertainties of background estimation are given in Table 50. For W+jets and Drell-Yan backgrounds, the systematic uncertainties are determined by data-driven methods, which are shown in Table 51. The systematic uncertainties for top and other diboson processes are determined by MC events, which are shown in Table 52 and Table 53.

After including luminosity, cross-section, lepton identification, jet veto, IRS/FSR, and pileup effect uncertainties, the background estimations and systematic uncertainties for ee , $\mu\mu$ and $e\mu$ channels are 0.17 ± 0.08 , 0.25 ± 0.15 and 1.26 ± 0.31 , respectively. The uncertainties are calculated by linearly summing the systematic uncertainties of top and diboson backgrounds (assuming 100% correlation), and then quadratically adding the contributions from Drell-Yan and W+jets (which are independently estimated from data).

Finally, the total background and its uncertainties are determined to be $1.68 \pm 0.37(\text{stat}) \pm 0.42(\text{syst})$. The total systematic uncertainty is calculated as $\sqrt{(0.28 + 0.04)^2 + 0.21^2 + 0.17^2}$, taking into account that the MC-estimated top and diboson background uncertainties are fully correlated, while the uncertainties for W+jets and Drell-Yan backgrounds are independently estimated from data. The overall background uncertainty is 0.56 events, calculated as the quadratic sum of $0.37(\text{stat}) \oplus 0.42(\text{syst})$. Therefore, the overall background estimation systematic uncertainty is $\sim 33.0\%$. We use a total of 33% systematic uncertainty in the overall W^+W^- background estimation for the cross section and detection sensitivity calculations.

| Source | Uncertainty | Influence | References |
|------------------------|-------------|--------------------------|------------|
| W^+W^- cross-section | 5% | MC signal expectation | ref [9] |
| $W/Z + jets$ | 10% | MC background estimation | ref [37] |
| $W/Z + \gamma$ | 5% | MC background estimation | ref [38] |
| $t\bar{t}$ | 12% | MC background estimation | ref [32] |

Table 47: Systematic uncertainties of cross-sections

| Source | Uncertainty | Influence | References |
|------------|-------------|-----------------|------------------------|
| luminosity | 3.4% | MC expectations | van der Meer Scan [39] |

Table 48: Luminosity measurement uncertainty

| Source | Mean | Uncertainty | Influence | References |
|---|-------|-------------|-------------------------|---------------|
| ee trig. SF | 100% | 0.02% | MC signal/bkg acc. | Section 5 |
| $\mu\mu$ trig. SF | 100% | 0.04% | MC signal/bkg acc. | Section 5 |
| $e\mu$ trig. SF | 100% | 0.02% | MC signal/bkg acc. | Section 5 |
| μ eff. SF (Overall) | 98.0% | 1.0% | MC signal efficiency | Section 6.2.4 |
| e eff. SF (Overall) | 97.0% | 3.3% | MC signal efficiency | Section 6.1 |
| μ Pt Scale/Resolution ($\mu\mu$) | - | 0.56% | MC signal/bkg acc. | Section 6.2.5 |
| μ Pt Scale/Resolution ($e\mu$) | - | 0.22% | MC signal/bkg acc. | Section 6.2.5 |
| Vertex Reweighting | - | 0.5% | MC signal/bkg acc. | Section 6.5.1 |
| E_T^e dependent eff. uncertainty (ee) | - | 6.0% | MC signal/bkg acc. | Section 6.1 |
| E_T^e dependent eff. uncertainty ($e\mu$) | - | 3.4% | MC signal/bkg acc. | Section 6.1 |
| ee SF (trigger and ID) | 94.1% | 7.6% | | |
| $\mu\mu$ SF (trigger and ID) | 96.0% | 1.5% | | |
| $e\mu$ SF (trigger and ID) | 95.1% | 4.9% | | |
| Jet Veto Eff. SF (W^+W^- signal) | 96.6% | 6.0% | MC diboson efficiency | Section 6.3.1 |
| ee SF (overall) | 90.9% | 9.7% | | |
| $\mu\mu$ SF (overall) | 92.7% | 6.2% | | |
| $e\mu$ SF (overall) | 91.9% | 7.7% | | |
| PDF Uncertainty on Acc. | - | 1.2% | MC W^+W^- signal acc. | Appendix E |

Table 49: Scale factors and systematic uncertainties on triggers and efficiencies of particle ID and selections.

| Source | Uncertainty | Influence | References |
|----------------------|-------------|-------------------|---------------|
| Jet Veto on Top (MC) | 40% | MC bkg efficiency | Section 6.3.1 |
| ISR/FSR on Top (MC) | 32% | MC bkg efficiency | Section 8.4 |

Table 50: Additional systematic uncertainties for MC top background estimations

| Source | Mean | Stat. Uncertainty | Syst. Uncertainty | References |
|----------------------------|------|-------------------|-------------------|------------|
| W+jets bkg (ee) | 0.08 | 0.05 | 0.03 | Section 8 |
| W+jets bkg ($\mu\mu$) | 0 | 0.29 | 0.10 | Section 8 |
| W+jets bkg ($e\mu$) | 0.46 | 0.12 | 0.17 | Section 8 |
| W+jets bkg (total) | 0.54 | 0.32 | 0.21 | Section 8 |
| Drell-Yan bkg (ee) | 0 | 0.10 | 0.07 | Section 8 |
| Drell-Yan bkg ($\mu\mu$) | 0.01 | 0.10 | 0.07 | Section 8 |
| Drell-Yan bkg ($e\mu$) | 0.22 | 0.06 | 0.15 | Section 8 |
| Drell-Yan bkg (total) | 0.23 | 0.15 | 0.17 | Section 8 |

Table 51: Background estimation for W+jets(data-driven method); For Drell-Yan sample, the mean value and statistical uncertainties are from MC estimation with scale factors applied and the systematic uncertainty is from data-driven method, which is described in Section 8.

| | Uncertainties | | | | | $N^{estimated}$ | $\pm \Delta N$ |
|----------|---------------|---------------|----------|-------------|--------|-----------------|----------------|
| | Lumi. | Cross-section | Jet-Veto | Lepton Acc. | Pileup | ISR/FSR | |
| ee | 0.034 | 0.12 | 0.40 | 0.076 | 0.005 | 0.32 | 0.04 |
| $\mu\mu$ | 0.034 | 0.12 | 0.40 | 0.015 | 0.005 | 0.32 | 0.14 |
| $e\mu$ | 0.034 | 0.12 | 0.40 | 0.049 | 0.005 | 0.32 | 0.35 |
| total | 0.34 | 0.12 | 0.40 | 0.042 | 0.005 | 0.32 | 0.28 |

Table 52: MC top background uncertainty calculation (The scale factors for acceptance are applied).

| | Uncertainties | | | | | $N^{estimated}$ | $\pm \Delta N$ |
|----------|---------------|---------------|----------|-------------|--------|-----------------|----------------|
| | Lumi. | Cross-section | Jet-Veto | Lepton Acc. | Pileup | | |
| ee | 0.034 | 0.05 | 0.06 | 0.076 | 0.005 | 0.05 | 0.006 |
| $\mu\mu$ | 0.034 | 0.05 | 0.06 | 0.015 | 0.005 | 0.10 | 0.009 |
| $e\mu$ | 0.034 | 0.05 | 0.06 | 0.049 | 0.005 | 0.23 | 0.023 |
| total | 0.034 | 0.05 | 0.06 | 0.042 | 0.005 | 0.38 | 0.04 |

Table 53: Uncertainty calculation for MC other diboson background (WZ, ZZ, $W\gamma$ and $Z\gamma$). Scale factors for acceptance are applied, and the Jet-Veto SF is used for WZ process.

| | Uncertainties | | | | | $N^{estimated}$ | $\pm \Delta N$ |
|----------|---------------|---------------|-----------|----------|-------------|-----------------|----------------|
| | Lumi. | Cross-section | A_{PDF} | Jet-Veto | Lepton Acc. | Pileup | |
| ee | 0.034 | 0.05 | 0.012 | 0.06 | 0.076 | 0.005 | 0.82 |
| $\mu\mu$ | 0.034 | 0.05 | 0.012 | 0.06 | 0.015 | 0.005 | 1.68 |
| $e\mu$ | 0.034 | 0.05 | 0.012 | 0.06 | 0.049 | 0.005 | 4.62 |
| total | 0.034 | 0.05 | 0.012 | 0.06 | 0.042 | 0.005 | 7.12 |

Table 54: MC W^+W^- signal uncertainty calculation (The scale factors for acceptance and Jet-Veto are applied). A_{PDF} is the W^+W^- signal acceptance uncertainty due to PDF uncertainty. W^+W^- signal yields are estimated using MCFM with MSTW2008 PDFs.

10 Results

This section summarizes the observed WW candidates and the signal and background estimates from which the WW production cross section is extracted. The WW detection significance is also calculated.

10.1 Observed W^+W^- candidates and MC expectations

The observed and expected number of events after applying all W^+W^- selection cuts are shown in Table 55. The overall WW signal acceptance has been shown in Section 7.4. The scale factor corrections (see Section 6.7) have been applied to MC expectations. The overall muon detection correction factor is 0.960 (mainly due to muon-ID inefficiency) for dimuon events. The overall electron detection correction factor is 0.941 (due to e-ID, e-isolation, and d_0 cut) for di-electron events. The overall correction factor for $e\mu$ events is 0.951. The additional scale factor for the jet veto cut is 0.966 (see Section 6.3.2). Section 9 gives the details for the systematic uncertainties used in this section. The results for the W +jets background estimation and the systematic uncertainty for the Drell-Yan background are obtained using data-driven methods which are described in Section 8.1 and Section 8.2, respectively. Both statistical (first) and systematic (second) uncertainties are given for all three dilepton channels in the table. The signal to background ratio ranges from 3.7 to 6.7 for the different dilepton final states. The combined observation and prediction from three dilepton channels are shown in Table 56.

Figures 46–48 each show one selected W^+W^- candidate event in data for each of the three investigated final states (Figure 46: $e^+e^-E_T^{\text{miss}}$, Figure 47: $\mu^+\mu^-E_T^{\text{miss}}$ and Figure 48: $e^+\mu^-E_T^{\text{miss}}$ final state).

| Final State | $e^+e^-E_T^{\text{miss}}$ | $\mu^+\mu^-E_T^{\text{miss}}$ | $e^\pm\mu^\mp E_T^{\text{miss}}$ |
|-----------------------------|---------------------------|-------------------------------|----------------------------------|
| Observed Events | 1 | 2 | 5 |
| Expected WW Signal | | | |
| MCFM with MSTW2008 PDF set | $0.82 \pm 0.02 \pm 0.09$ | $1.68 \pm 0.04 \pm 0.15$ | $4.63 \pm 0.06 \pm 0.46$ |
| MC@NLO with CTEQ6.6 PDF set | $0.79 \pm 0.02 \pm 0.09$ | $1.61 \pm 0.04 \pm 0.14$ | $4.46 \pm 0.06 \pm 0.44$ |
| Background estimations | | | |
| Top(MC) | $0.04 \pm 0.024 \pm 0.02$ | $0.14 \pm 0.06 \pm 0.07$ | $0.35 \pm 0.10 \pm 0.19$ |
| W+jets (data-driven) | $0.08 \pm 0.05 \pm 0.03$ | $0 \pm 0.29 \pm 0.10$ | $0.46 \pm 0.12 \pm 0.17$ |
| Z+jets* (MC/data-driven) | $0 \pm 0.10 \pm 0.07$ | $0.01 \pm 0.10 \pm 0.07$ | $0.22 \pm 0.06 \pm 0.15$ |
| Other dibosons (MC) | $0.05 \pm 0.01 \pm 0.006$ | $0.10 \pm 0.004 \pm 0.009$ | $0.23 \pm 0.05 \pm 0.023$ |
| Total Background | $0.17 \pm 0.11 \pm 0.08$ | $0.25 \pm 0.31 \pm 0.15$ | $1.26 \pm 0.17 \pm 0.31$ |
| Signal / Background | 4.8 | 6.7 | 3.7 |

Table 55: W^+W^- signal (including about a $\sim 10\%$ contribution from tauonic decays) and background expectations determined by MC (with SF applied) and estimated using data driven methods. Both statistical (first) and systematic (second) uncertainties are given in the table. For the total systematic background uncertainties, top and “other dibosons” background systematics are first combined linearly (assuming 100% correlation), and then the Z+jets and the W+jets systematic uncertainties (independently estimated from data) are added quadratically. In case of the quoted errors greater than the central values, the lower boundary of background contribution should be taken as zero. *The central value and statistical uncertainty for the Z+jets process estimation is MC based while the systematic uncertainties are derived from a data-driven method.

| Source | number of events (after SF correction) |
|-----------------------------|--|
| MC signal expectation from | 7.12±0.07±0.70 |
| MCFM with MSTW2008 PDF set | |
| Top | 0.53±0.12±0.28 |
| W+X | 0.54±0.32±0.21 |
| Z+X | 0.23±0.15±0.17 |
| Diboson | 0.38±0.04±0.04 |
| Total Background Estimation | 1.68±0.37±0.42 |
| Expected Total Events | 8.80±0.38±1.12 |
| Data | 8 |

Table 56: The total number of dilepton events passing the full $W^+W^- \rightarrow \ell^+\nu_\ell\ell^-\bar{\nu}_\ell$ selection criteria from collision data, compared to the expectation from MC signal and background estimation (MC and data-driven methods). Both statistical (first uncertainty) and systematic (second) uncertainties are given. For the total systematic background uncertainty, top and “other dibosons” background systematics are first combined linearly (assuming 100% correlation), and then the Z+X and the W+X systematic uncertainties (independently estimated from data) are added quadratically. The SF corrections are applied to MC.

10.2 Measurement of the W^+W^- production cross section

The W^+W^- production cross section is determined from the three dilepton channels ($WW \rightarrow e\bar{e}v\bar{v}$, $\mu\nu\bar{\mu}\bar{\nu}$ and $e\nu\mu\nu$) using two different methods. The first method uses the simple formula shown in Equation 19:

$$\sigma_{WW} = \frac{N_{obs} - N_{bkg}}{\epsilon \mathcal{A} \mathcal{L} Br}, \quad (19)$$

where N_{obs} is the number of observed events, N_{bkg} is the number of expected background, $\epsilon \mathcal{A}$ is the acceptance times efficiency with SF correction which are treated as one number, \mathcal{L} is the integrated luminosity and Br is the branching ratio of leptonic decays of $W^+W^- \rightarrow \ell^+\nu_\ell\ell^-\bar{\nu}_\ell$.

The second method uses a maximum log-likelihood function to fit the W^+W^- cross section using the CERN MINUIT package. The maximum log-likelihood based on Poisson statistics is constructed using selected MC and data events for the individual dilepton channels as shown in Equation 20:

$$F = \ln \prod_{i=1}^3 \frac{e^{-(N_s^i + N_b^i)} (N_s^i + N_b^i)^{N_{obs}^i}}{N_{obs}^i!}, \quad N_s^i = \sigma_{WW} \times Br \times L \times A \times SF, \quad (20)$$

where $i = 1, 2, 3$ runs over the three dilepton channels. N_s^i , N_b^i and N_{obs}^i represent the expected signal, background events and observed data events for the i -th dilepton channel. Br is the branching ratio, L is the integrated luminosity, A is signal acceptance and SF is the scale factor to correct the selection efficiency difference between data and MC. The W^+W^- cross section σ_{WW} is determined by maximizing the log-likelihood function F .

The measured W^+W^- cross sections using the simple formula and the maximum log-likelihood fit methods are listed in Table 57. The mean values of the W^+W^- cross sections obtained from both methods are consistent with each other and with the SM NLO prediction for W^+W^- production of 46 ± 3 pb.

Combining the three dilepton channels, the fitted W^+W^- cross section is $41.2^{+20.5}_{-16.2}(stat) \pm 4.9(syst)$ pb. The statistical uncertainty is the dominant uncertainty for this measurement ($\sim 44\%$). The total systematic uncertainty is $\sim 12.0\%$ which includes the luminosity uncertainty (3.4%), acceptance uncertainty ($\sim 7.4\%$) and background estimation total uncertainty ($\Delta N_b/N_b = 33\%$). The systematic error is calculated using error propagation: $\sigma_{syst}/\sigma_{WW} = \sqrt{(\Delta L/L)^2 + (\Delta A/A)^2 + (\Delta N_b/(N_{obs} - N_b))^2}$.

| Channels | N_s | N_b | N_{obs} | σ_{WW} (pb) | Fitted σ_{WW} (pb) |
|----------------|-------|-------|-----------|--------------------|---------------------------|
| <i>even</i> | 0.82 | 0.17 | 1 | 46.8 | $46.8^{+76.6}_{-39.4}$ |
| $\mu\nu\mu\nu$ | 1.68 | 0.25 | 2 | 48.2 | $48.2^{+48.6}_{-30.4}$ |
| $e\nu\mu\nu$ | 4.63 | 1.26 | 5 | 37.4 | $37.4^{+25.8}_{-19.2}$ |
| Total | 7.13 | 1.68 | 8 | 41.0 | $41.2^{+20.5}_{-16.2}$ |

Table 57: Inputs for the WW cross-section measurements and the corresponding extracted results. The given uncertainties are statistical only.

10.3 W^+W^- detection sensitivity

The W^+W^- detection sensitivity is estimated using the log-likelihood ratio method as shown in Equation 21.

$$-2 \ln Q = -2 \ln \frac{L(s+b)}{L(b)}; \quad L(s+b) = \frac{e^{-(N_s+N_b)}(N_s + N_b)^{N_{obs}}}{N_{obs}!}, \quad L(b) = \frac{e^{-N_b}(N_b)^{N_{obs}}}{N_{obs}!}, \quad (21)$$

where N_s , N_b and N_{obs} represent expected signal, background, and observed data events for the three di-lepton channels combined. To take into account the possibility of background fluctuations, 10 million pseudo-experiments were performed, using the expected number of background events as the mean value of a Poisson distribution to produce ‘observed’ events (N_{obs}) for each pseudo-experiment. The background uncertainty of 0.56 events is included as a Gaussian variation of the expected background yield. This uncertainty on the background estimate includes both statistical and systematic uncertainties.

With eight observed W^+W^- candidate events and 1.68 ± 0.56 (stat \oplus syst) estimated background events, we estimate that the probability for the background to fluctuate up to at least the observed number of events in the absence of the signal is 1.2×10^{-3} , corresponding to a significance of 3.0 standard deviations for the signal observation. The expected W^+W^- detection sensitivity from the MC simulation is 3.4 standard deviations, with a probability of 4.0×10^{-4} for the background-only hypothesis.

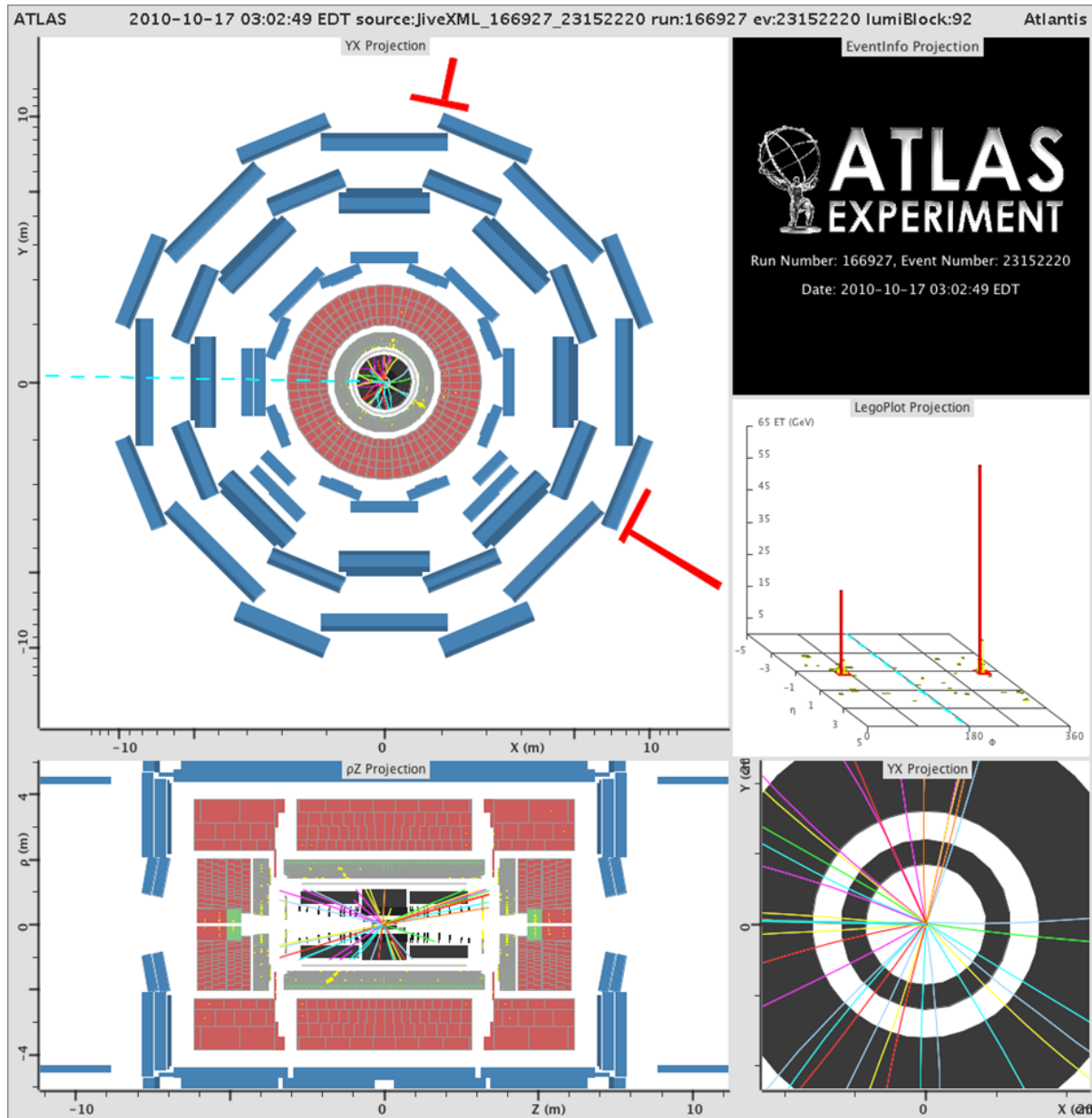


Figure 46: An event display for a candidate from $q\bar{q}' \rightarrow WW \rightarrow ee\nu\nu$.

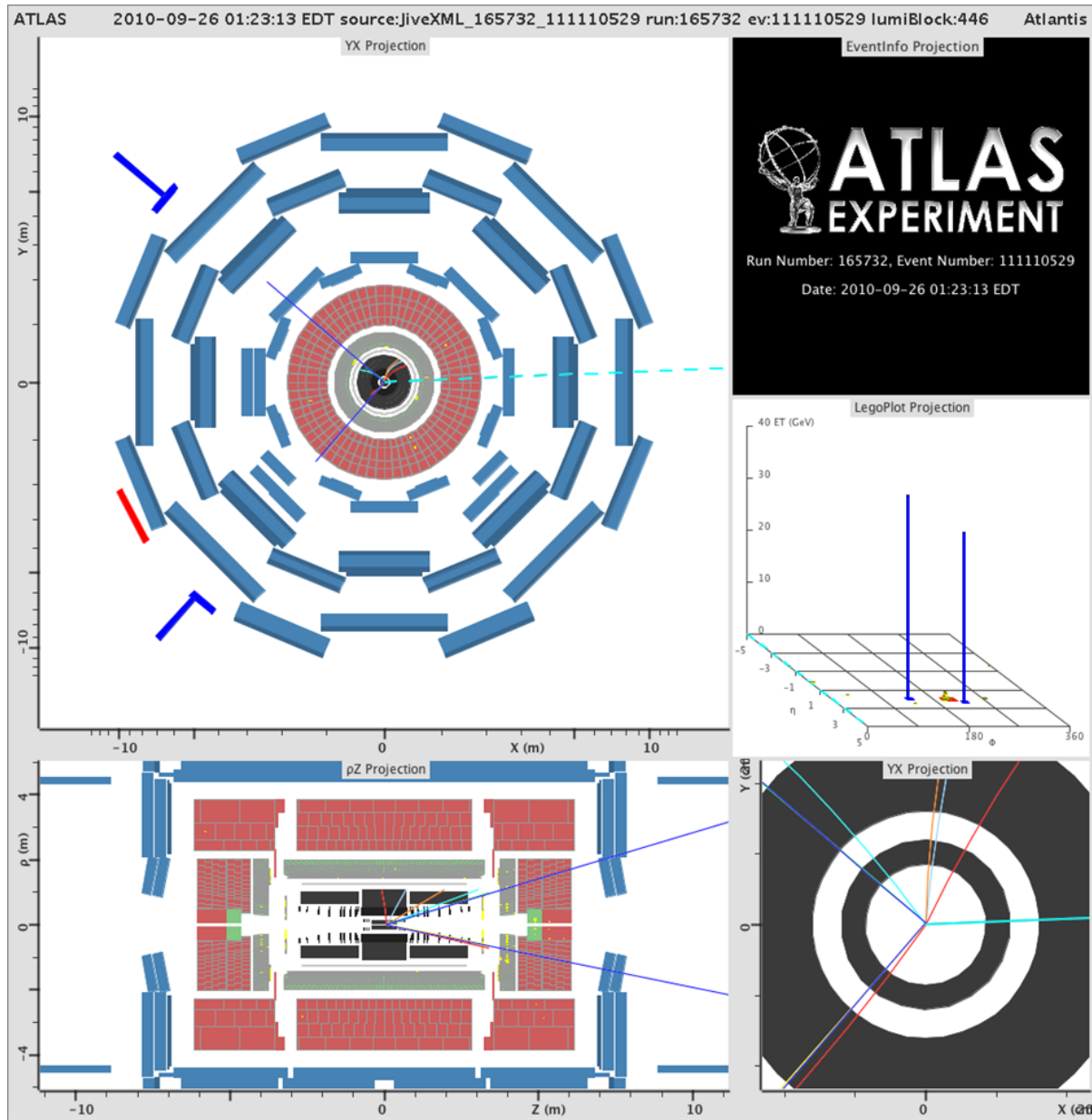


Figure 47: An event display for a candidate from $q\bar{q}' \rightarrow WW \rightarrow \mu\nu\mu\nu$.

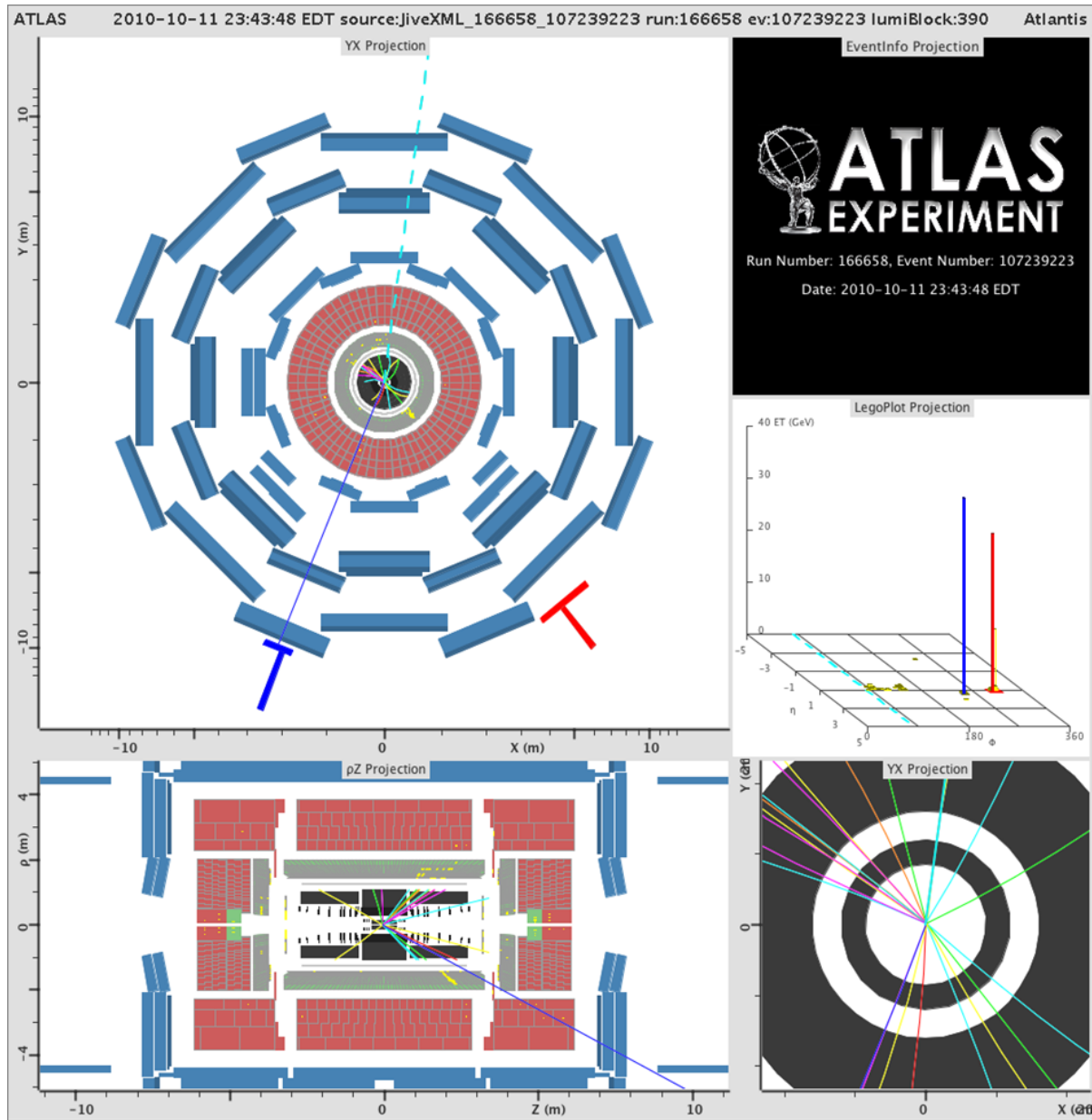


Figure 48: An event display for a candidate from $q\bar{q}' \rightarrow WW \rightarrow e\nu\mu\nu$.

A W+jets background validation

Figure 49 shows the comparison of p_T distribution for Jet-Rich electron and muon of dijet MC and that of W +jets MC. p_T distribution of Jet-Rich lepton from W +jets seems to be harder than that from dijet MC passed J15 trigger. To reduce p_T dependence among samples, it would be reasonable to estimate fake rate as a function of p_T .

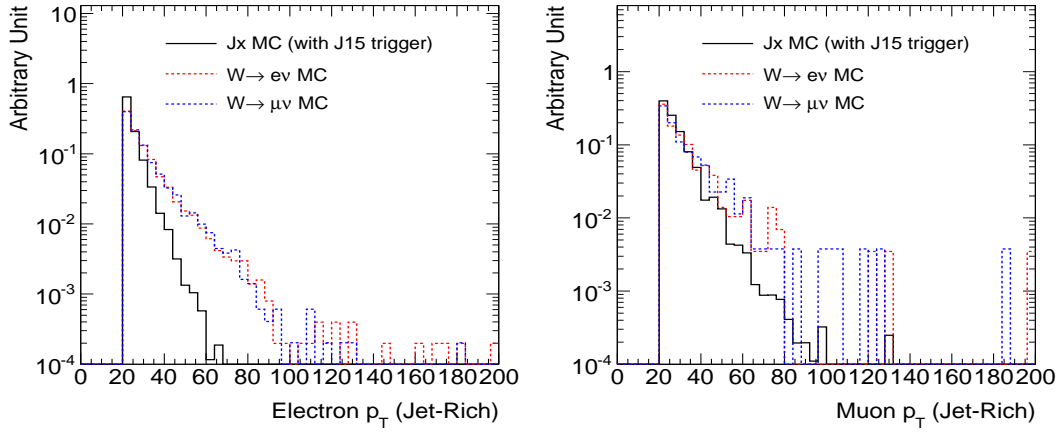


Figure 49: The comparison of p_T distribution between Jet-Rich lepton of dijet MC and that of W +jets MC. Left(Right): Jet-Rich electron(muon) p_T distribution.

Figure 50 shows p_T distribution for dijet MC and observed data passed J15 trigger. MC distribution is normalized to the number of observed Jet-Rich ID objects. Jet-Rich ID object shapes are modeled well by the MC for electron and muon, respectively, according to the ratio of Jet-Rich ID object. However the ratio of lepton ID object are different. In particular, the ratio of lepton ID object for electron seems to be higher although the dijet MC statistics are very limited. As a results, fake factor is not modeled well by the MC.

B W+jets background cross check.

The W +jet background presented in Section 8.1 has been independently cross checked. This independent cross check has been done using a variation of the data-driven method described above. A description of differences in the W +jet background method and results of the cross check are presented in this section.

The remainder of this section is organized as follows: Section B.0.1 highlights the differences in the fake factor calculation and measurement in data, Section B.0.3 describes a data-driven cross check of the W +jet background estimation, Section B.0.4 presents the W +jet background estimates, and Section B.0.5 discusses the consistency of the two methods.

B.0.1 Calculation of the fake factor.

The definition of the fake factor depends on the jet-rich lepton definitions. A major difference between the two W +jet methods is the jet-rich lepton definitions. Both the fully-identified and jet-rich leptons are required to pass common acceptance, kinematic and isolation requirements. These common requirements are listed in Table 58.

The fully-identified electrons are further required to satisfy electron ID, whereas the jet-rich leptons are further required to fail the RobustMedium electron ID. Two fully-identified lepton definitions are

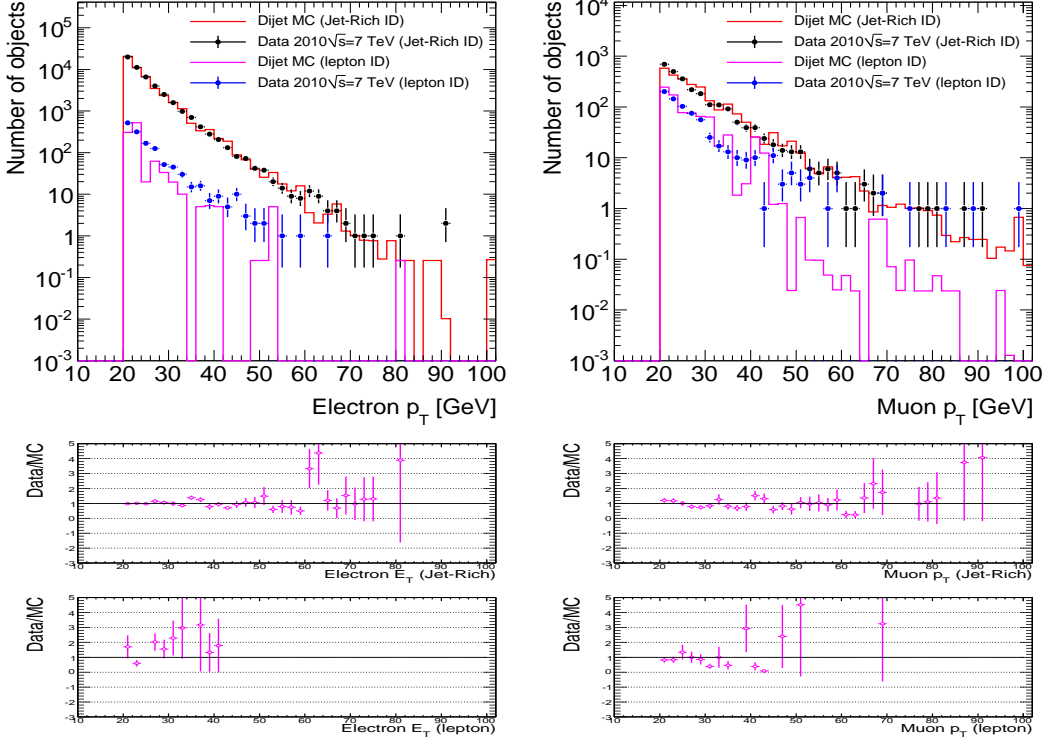


Figure 50: Left three plots show electron p_T distribution and the ratio of data to MC for Jet-Rich Id object and lepton Id object. Right three plots show muon p_T distribution and the ratio of data to MC for Jet-Rich Id object and lepton Id object.

used. The first, uses the standard RobusterTight electron ID and is used to determine the W +jet background in the W^+W^- signal selection. The second is the standard W^+W^- electron definition where the looser RobustMedium electron ID replaces RobusterTight. This lepton definition is used to cross-check the procedure with increased statistics.

Another major difference with the present W +jet background procedure is the sample used to calculate the fake factors. The fake factors, as defined in Equation 11, is calculated using events triggering the `EF_g17_etcut` trigger. This trigger requires a reconstructed EM cluster above 17 GeV and does not make any electron ID requirement. Electrons from electroweak processes are suppressed by excluding events that have missing E_T above 15 GeV or containing two reconstructed electron candidates with an invariant mass within 10 GeV of the Z mass. The remaining electroweak contribution to the dijet sample is subtracted using W and Z MC.

A major systematic uncertainty associated to the fake factor determination is the variation due to jet kinematics and composition. In order to assess this systematic the dijet sample is divided into sub-samples according to the E_T of the opposite side jet ($\Delta R > 0.4$). The fake factors are then measured separately for each JX sub-sample, where X is the opposite side jet E_T threshold in GeV. The variation of the fake factor among the JX sub-samples provides a measure of the systematic uncertainty on the fake factor calculation. The measured fake factors as a function of electron E_T for RobustMedium and RobusterTight are shown in Figure 51. The fake factor is the weighted average for each bin and the yellow band represents the $\pm 30\%$ variation of this weighted average, which covers the fake factors determined in the various JX sub-samples.

| Common Lepton Selection |
|---|
| Reconstructed Electron Candidate |
| Geometrical Acceptance: $ \eta < 2.5$, outside crack region |
| Data Quality: Outside regions w/LAr readout problems |
| Kinematic Acceptance: $E_T > 20\text{GeV}$ |
| Impact parameter requirement: $\frac{d_0}{\sigma_{d_0}} < 10$ and $z_0 < 10 \text{ mm}$ |
| Track Quality: $N_{Si} > 0$ |
| Track p_T : track $p_T > 2\text{GeV}$ |
| Isolation Requirement: $eTCone30 < 6\text{GeV}$ |

Table 58: Common Selection that is applied to both the fully-identified and jet-rich lepton ID.

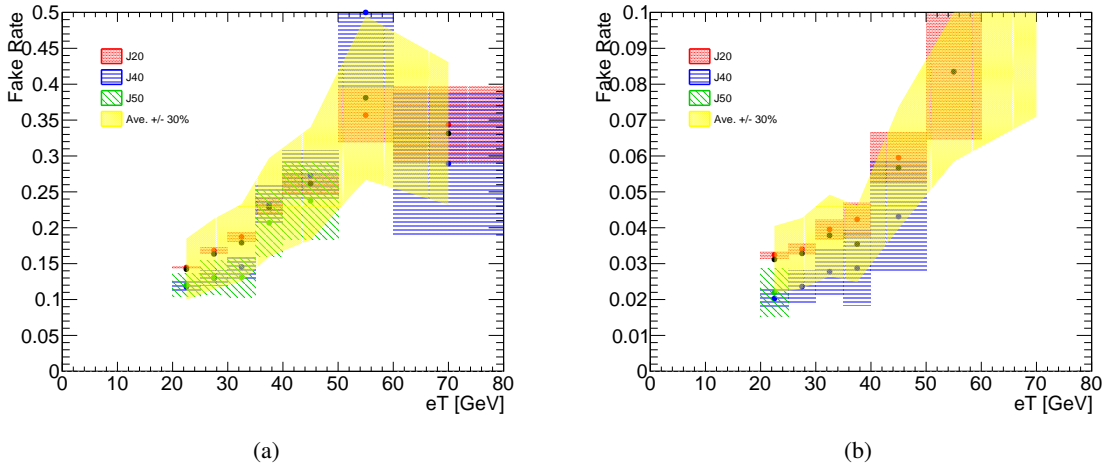


Figure 51: Measured fake factor as a function of electron E_T for RobustMedium (a) and RobusterTight (b) electron ID.

B.0.2 Non- W +jet Correction to W +jet Control Region.

The W +jet control region is constructed to be enriched in W +jet events. Contamination of this region by events from other physics processes will bias the W +jet background estimation. W +jet background prediction is corrected due to the presence of $W+\gamma$, Z , top, and W^+W^- events in the W +jet control region. These corrections are obtained by running the W +jet background procedure on the $W+\gamma$, Z , top, and W^+W^- MC. The final W +jet background prediction is made by subtracting the W +jet background estimated from the non- W +jet MC, from the W +jet estimation from data. The non- W +jet correction is on the order of 10% of the total W +jet background. The MC corrections are presented along with the results of the W +jet background from data in Tables 63 and 64 in Section B.0.4.

B.0.3 Same sign control region

The sample obtained by reversing the opposite-sign lepton requirement in the W^+W^- selection is enriched in W +jet events where the jet is misidentified as a lepton. The fake factor procedure can be applied to the same-sign W +jet enriched events to predict the yield in the same-sign events in which both leptons pass the fully-identified lepton ID. This same-sign control region provides a data-driven cross check of the fake factor procedure. To increase the statistics in this control region the jet veto, Z

veto, and the di-lepton p_T cut have been dropped from the W^+W^- event selection.

The observed number of events along with the prediction in the same-sign control region are presented in Tables 59 - 62. The prediction includes the W +jet modeling from the fake factor procedure as well as the contributions from $W+\gamma$, Z , top, and W^+W^- predicted by the MC. The results are shown for the e-e and e- μ channels using both RobustMedium and RobusterTight electron ID. The W +jet prediction in the e- μ channels only contain the contribution from jets misidentified as electrons, the smaller contribution from jets misidentified as muons has been neglected. The uncertainties on the predicted number of events include the statistical and systematic uncertainties on the W +jet prediction as well as the statistical uncertainties on the MC predictions. The systematic uncertainty on the W +jet prediction is given by the 30% uncertainty on the fake factor. Although the uncertainties are large, a general agreement between the observed and predicted number of events in the same-sign control region is found.

| ee-channel (Medium) | N_{Event}^{Raw} | N_{Event} |
|-------------------------------------|-------------------|--------------------|
| W+Jet Estimate from Data | 8 | 1.242 ± 0.576 |
| W+Jet MC Correction from $W+\gamma$ | 0.525 | -0.094 ± 0.033 |
| W+Jet MC Correction from Z | 0.0 | 0.0 ± 0.0 |
| W+Jet MC Correction from Top | 0.696 | -0.102 ± 0.036 |
| W+Jet MC Correction from W^+W^- | 0.023 | -0.005 ± 0.002 |
| Total W+Jet Prediction | - | 1.041 ± 0.578 |
| $W+\gamma$ MC Prediction | - | 0.672 ± 0.105 |
| Z MC Prediction | - | 0.0 ± 0.0 |
| Top MC Prediction | - | 0.441 ± 0.101 |
| W^+W^- MC Prediction | - | 0.033 ± 0.003 |
| Total Prediction | - | 2.187 ± 0.596 |
| Observed | - | 0 |

Table 59: Same-sign prediction for the ee-channel using RobustMedium electron ID. The total W +jet background is the sum of the data estimation and the MC corrections. The total prediction is the sum of the W +jet prediction and the $W+\gamma$, Z , top, and W^+W^- predictions from the MC.

B.0.4 Application to Signal Region

The W +jet background obtained from the fake factor procedure for the e-e and e- μ channels is presented in Tables 63 and 64. The total background is the sum of the W +jet estimation from data and the non- W +jet MC correction. The total uncertainties are the quadratic sum of the uncertainties on the W +jet prediction from data and the MC corrections. The systematic uncertainties are due to a 30% systematic uncertainty on the measured fake factor.

B.0.5 Comparison of W+Jets methods.

The W +jet procedure presented in Section 8.1, referred to here as method-T, estimated the W +jet background to be $0.08 \pm 0.05 \pm 0.03$ in the ee-channel and $0.45 \pm 0.12 \pm 0.16$ in the e μ -channel. The W +jet procedure presented in Section B, referred to here as method-P, estimated the W +jet background to be $0.12 \pm 0.07 \pm 0.04$ in the ee-channel and $0.68 \pm 0.17 \pm 0.24$ in the e μ -channel. The two procedures use a similar method to extract the W +jet background and are thus correlated. Overlap in the W +jet control regions and potential common systematics, prevents one from naively comparing the difference in

| ee-channel (Tight) | N_{Event}^{Raw} | N_{Event} |
|-------------------------------------|-------------------|--------------------|
| W+Jet Estimate from Data | 7 | 0.233 ± 0.113 |
| W+Jet MC Correction from $W+\gamma$ | 0.341 | -0.013 ± 0.004 |
| W+Jet MC Correction from Z | 0.0 | 0.0 ± 0.0 |
| W+Jet MC Correction from Top | 0.764 | -0.014 ± 0.005 |
| W+Jet MC Correction from W^+W^- | 0.016 | -0.001 ± 0.0 |
| Total W+Jet Prediction | - | 0.206 ± 0.113 |
| $W+\gamma$ MC Prediction | - | 0.066 ± 0.029 |
| Z MC Prediction | - | 0.0 ± 0.0 |
| Top MC Prediction | - | 0.183 ± 0.075 |
| W^+W^- MC Prediction | - | 0.006 ± 0.001 |
| Total Prediction | - | 0.461 ± 0.139 |
| Observed | - | 0 |

Table 60: Same-sign prediction for the ee-channel using RobusterTight electron ID. The total W +jet background is the sum of the data estimation and the MC corrections. The total prediction is the sum of the W +jet prediction and the $W+\gamma$, Z, top, and W^+W^- predictions from the MC.

central values with the associated uncertainty as a measure of consistency. The remainder of this section discusses sources of the central value disagreement and the compatibility of the results.

There are two aspects of W +jet background procedure in which there is discretionary freedom: the assignment of fake-factor central values and the definition jet-rich leptons. Different specifications can produce equally valid background estimates, while differing in the central values.

The first place where a choice is made that effects the W +jet background prediction is assignment of fake-factor the central values. As presented above, the fake-factors are only known to the $\sim 30\%$ level. There is not a unique procedure for assigning the fake-factor central value. Several methods exist, which produce results that agree within the uncertainty. Method-T has chosen to use the fake factor of the jet-triggered sample with the highest statistics, J15. Method-P has chosen to take the weighed average of the J20,J30, and J50 fake-factors measurements described above.. It has been verified that the 30% systemic uncertainty covers the differences in procedure, which is at the 10% level. Given the difference in the samples used to determine the fake-factors, and in the procedures for determining their central values, the assigned systematic uncertainty can be used to measure of the level agreement in the predictions.

The other place where a choice is made is in the definition the jet-rich leptons. The fully-identified leptons definitions are dictated by the lepton selection used in the analysis. The choice of the jet-rich definitions are, on the other hand, arbitrary. There are reasons for considering different jet-rich definitions. Some tend to reduce statistical uncertainty, others would have smaller systematic uncertainties. There is no one correct choice, and indeed the W +jet background procedures used in this analysis have different jet-rich definitions. Differences in jet-rich definitions give rise to different fake-factors and different W +jet control samples. In a high statistics sample, the difference in fake-factor will be compensated by the differences in the number of events in the W +jet control region, such that the background procedures will agree within uncertainties.

Method-T has chosen a jet-rich electron definition in which RobusterTight electrons are vetoed. Method-P has chosen a jet-rich electron definition in which RobustMedium electrons are vetoed. (There are other slight differences which can be set aside for the moment.) For method-T, the jet-rich definition is more inclusive, the fake-factor is smaller, and there is a larger expected W +jet control region. For method-P, the jet-rich definition is less inclusive, the fake-factor is larger, and there is a smaller expected

| eμ-channel (Medium) | N_{Event}^{Raw} | N_{Event} |
|---|-------------------|--------------------|
| W+Jet Estimate from Data | 28 | 5.3 ± 1.879 |
| W+Jet MC Correction from W+ γ | 2.237 | -0.531 ± 0.165 |
| W+Jet MC Correction from Z | 0.915 | -0.194 ± 0.066 |
| W+Jet MC Correction from Top | 1.168 | -0.21 ± 0.069 |
| W+Jet MC Correction from W^+W^- | 0.052 | -0.013 ± 0.004 |
| Total W+Jet Prediction | - | 4.352 ± 1.889 |
| W+ γ MC Prediction | - | 2.628 ± 0.203 |
| Z MC Prediction | - | 0.272 ± 0.082 |
| Top MC Prediction | - | 0.876 ± 0.135 |
| W^+W^- MC Prediction | - | 0.07 ± 0.004 |
| Total Prediction | - | 8.198 ± 1.906 |
| Observed | - | 10 |

Table 61: Same-sign prediction for the $e\mu$ -channel using RobustMedium electron ID. The total W +jet background is the sum of the data estimation and the MC corrections. The total prediction is the sum of the W +jet prediction and the $W+\gamma$, Z, top, and W^+W^- predictions from the MC.

W +jet control region.

We have preformed an event-by-event comparison of the events in the two W +jet control regions.

In the ee-channel, the two methods have found the same four events. The W +jet predictions are different because of the difference in fake-factors. There could have been different events in W +jet control regions given the different jet-rich definitions. These differences were not seen and are attributed to the small statistics of the sample.

In the $e\mu$ -channel, method-T has 23 event in the W +jet control region and method-P has 22 events in the W +jet control region. There is agreement on 16 events. Method-P has 6 events which method-T does not. Four are due to differences in jet-rich electron definition: method-T requires $N_{Pix} > 0$, whereas method-P requires $N_{Si} > 0$. These four events have reconstructed electron candidates with $nSi > 0$ but no pixel hits. These differences in W +jet control region are expected.

Method-T has 7 events which method-P does not. All are due to differences in jet-rich electron definition. Six have electron candidates passing RobustMedium, one has an electron with $\frac{d0}{\sigma_{d0}} > 10$. These events satisfy method-P's jet-rich definition, but fail that of method-T. Again, these differences in W +jet control region are expected.

The statistical uncertainties on the W +jet predictions do not fully cancel in a copmarision of the results. The correlation in the W +jet control regions is high, but not unity.

It is felt that there is a satisfactory level of agreement in the W +jet results given the low statistics, the differences in jet-rich definitions, and the differneces fake-factor determinations. The systematic uncertainties are an indication of this agreement, and there is not a complete cancelation of the large statistical uncertainties. A combination of the two results is non-trivial, given the correlations in the procedures. It is felt that it ts best to proceed using the results of method-T for the significance and cross section determination, and to employ method-P as an independent validation of the W +jet background prediction.

| eμ-channel (Tight) | N_{Event}^{Raw} | N_{Event} |
|--|-------------------|--------------------|
| W+Jet Estimate from Data | 28 | 0.994 ± 0.352 |
| W+Jet MC Correction from W+ γ | 2.237 | -0.082 ± 0.026 |
| W+Jet MC Correction from Z | 0.915 | -0.034 ± 0.012 |
| W+Jet MC Correction from Top | 1.168 | -0.039 ± 0.013 |
| W+Jet MC Correction from W^+W^- | 0.052 | -0.002 ± 0.001 |
| Total W+Jet Prediction | - | 0.836 ± 0.354 |
| W+ γ MC Prediction | - | 0.327 ± 0.075 |
| Z MC Prediction | - | 0.026 ± 0.026 |
| Top MC Prediction | - | 0.439 ± 0.106 |
| W^+W^- MC Prediction | - | 0.023 ± 0.002 |
| Total Prediction | - | 1.651 ± 0.378 |
| Observed | - | 1 |

Table 62: Same-sign prediction for the e μ -channel using RobusterTight electron ID. The total W+jet background is the sum of the data estimation and the MC corrections. The total prediction is the sum of the W+jet prediction and the W+ γ , Z, top, and W^+W^- predictions from the MC.

| ee-channel | N_{Event}^{Raw} | $N_{Event} \pm (\text{stat}) \pm (\text{syst})$ |
|--------------------------------------|-------------------|---|
| W+Jet Estimate from Data | 4.0 | $0.1305 \pm 0.0653 \pm 0.0392$ |
| Total MC Correction | - | $-0.0155 \pm 0.0026 \pm 0.0032$ |
| W+Jet MC Correction from W+ γ | 0.3241 | $-0.0099 \pm 0.0024 \pm -0.003$ |
| W+Jet MC Correction from Z | 0.0321 | $-0.0006 \pm 0.0006 \pm -0.0002$ |
| W+Jet MC Correction from Top | 0.0364 | $-0.0012 \pm 0.0008 \pm -0.0003$ |
| W+Jet MC Correction from W^+W^- | 0.1225 | $-0.0039 \pm 0.0002 \pm -0.0012$ |
| Total W+Jet Background | - | $0.1151 \pm 0.0653 \pm 0.0392$ |

Table 63: W+jet background prediction for the ee-channel. Total W+jet background is the sum of the data estimation and the MC corrections.

| eμ-channel | N_{Event}^{Raw} | $N_{Event} \pm (\text{stat}) \pm (\text{syst})$ |
|--------------------------------------|-------------------|---|
| W+Jet Estimate from Data | 22.0 | $0.7839 \pm 0.1671 \pm 0.2352$ |
| Total MC Correction | - | $-0.1051 \pm 0.0095 \pm 0.0202$ |
| W+Jet MC Correction from W+ γ | 1.6016 | $-0.0435 \pm 0.0047 \pm -0.013$ |
| W+Jet MC Correction from Z | 1.1884 | $-0.05 \pm 0.0082 \pm -0.015$ |
| W+Jet MC Correction from Top | 0.0364 | $-0.0006 \pm 0.0004 \pm -0.0002$ |
| W+Jet MC Correction from W^+W^- | 0.3354 | $-0.011 \pm 0.0003 \pm -0.0033$ |
| Total W+Jet Background | - | $0.6789 \pm 0.1674 \pm 0.2352$ |

Table 64: W+jet background prediction for the e μ -channel. Total W+jet background is the sum of the data estimation and the MC corrections.

C Estimate W+jets background using matrix method

The matrix method is used to estimate the W+jets background. This method involves the selection of a tight sample and a loose sample. In this study the tight sample is obtained by applying the full W^+W^- selection cuts while the loose sample is selected with all the cuts except that only one isolated lepton is required instead of two in the W^+W^- selection. The W+jets background can be obtained from the following two equations:

$$N_{loose} = N_{WW} + N_{Wjets}$$

$$N_{iso} = \epsilon_{lep} \times N_{WW} + \epsilon_{jet} \times N_{Wjets}$$

Where N_{loose} is the number of events in the loose sample, while N_{iso} is the number of events in the tight sample. ϵ_{lep} is the single lepton isolation efficiency, which is measured from data using tag-and-probe technique. ϵ_{jet} is the isolation efficiency of the lepton fakes from jets determined by MC (electron) or by QCD jet data events (muon) (see Figure 52). The determination of isolation efficiency is described in Section 6.

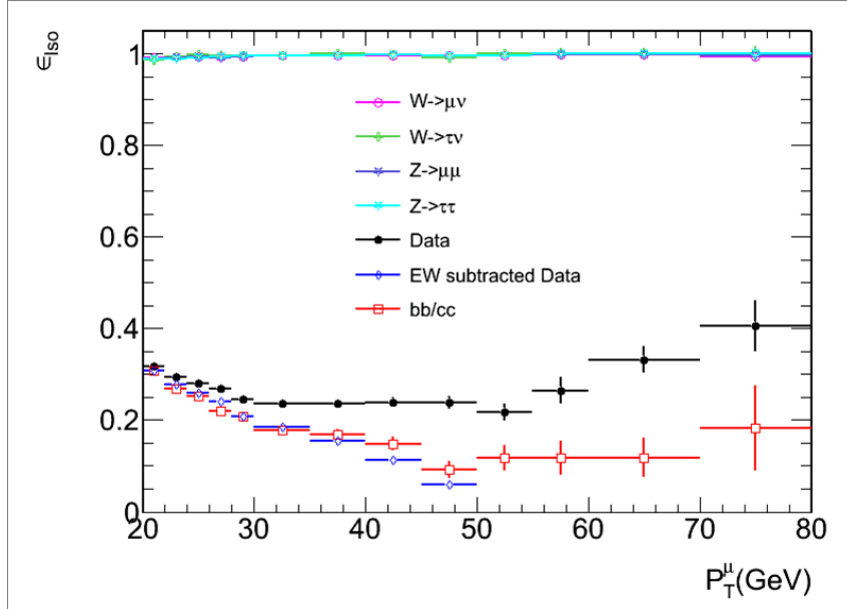


Figure 52: Fake muon rate as a function of muon p_T obtained from QCD rich data sample. The blue dots in plot are the fake rate from the EW subtracted data.

The estimation of W+jets contamination in the zero-jet bin in each channel are detailed in Table 65. The final result for W+jets where the jet fakes a muon is <0.2 at 68% confidence level or <0.4 at 90% confidence level. The estimated W+jets background where the jet fakes an electron is $0.71 \pm 0.15(\text{stat}) \pm 0.22(\text{sys})$. The total W+jets background should be the sum of these two cases.

Table 65: W+jets background estimation in W^+W^- selection using matrix method for 0 jet bin.

| Channels | N_{loose} | N_{iso} | ϵ_{lep} | ϵ_{jet} | N_{Wjets} | $\epsilon_{jet} \times N_{Wjets}$ |
|---|-------------|-----------|------------------|------------------|-------------|-----------------------------------|
| $W(\rightarrow \mu) + jet(\rightarrow \mu)$ | 5 | 5 | 0.991 | 0.18 | 0 | 0 |
| $W(\rightarrow e) + jet(\rightarrow \mu)$ | 6 | 6 | 0.991 | 0.18 | 0 | 0 |
| $W(\rightarrow \mu) + jet(\rightarrow e)$ | 7 | 6 | 0.974 | 0.20 | 1.060 | 0.212 |
| $W(\rightarrow e) + jet(\rightarrow e)$ | 3 | 1 | 0.974 | 0.20 | 2.483 | 0.497 |

D MET Studies

In this section we evaluate the performance of the E_T^{miss} reconstruction relevant to the analysis. This also includes investigating the correlation between E_T^{miss} and the transverse momentum of the di-lepton system. In order to do this we choose a control sample made of di-lepton events with an invariant mass close to the Z boson mass. All the requirements of the event selection are made except for the fact that the Z boson veto is reversed (see Section 7.1) and the requirements on the E_T^{miss} and $P_{T\text{ll}}$ are not applied.

The data is compared with the Z boson MC (Pythia samples).⁸ All MC samples used here have a simulation of the pile-up. The MC samples have been reweighed according to the number of vertexes with at least three tracks. The reweighting factors are similar to those used in Section 6.5.1. In all plots shown in this section the MC is normalized to the number of events in data.

Figure 53 displays the distribution of the transverse momentum of the di-lepton system. Overall the description of the data by the MC is reasonable. In principle this is a measure of how well Pythia describes the recoil of the Z system due to soft and semi-hard radiation and other minor effects. This plot does not tell us much about the details about how this activity is distributed in η and p_T . These are relevant quantities for the simulation of the E_T^{miss} and requires a detailed study of the underlying event in Z events.

Figure 54 shows the E_T^{miss} distributions for the di-electrons and di-muon events. Overall the description of the MET resolution by the MC is reasonable. The MC only contains the Z boson. In a future update the di-lepton candidates from continuum W^+W^- and top backgrounds will be added. These may enhance the region of large E_T^{miss} . It is noted that the MC description seems somewhat worse for electrons. The tails in the E_T^{miss} distribution for the di-muon sample are larger in data than in MC. This needs further investigation. The differences between data and MC with regards to the probability of measuring an event with E_T^{miss} is taken into account in the systematic.

Figure 55 show the azimuthal angle of the E_T^{miss} for the di-electron and di-muon samples. The data displays a slightly stronger modulation than MC. However, the size of the modulation in data is significantly smaller than that observed with minimum bias and di-jet events. The systematics on the acceptance of a cut on E_T^{miss} due to this modulation was found to be negligibly small compared to other systematic checks performed for the W observation.

Figure 56 shows the difference in azimuthal angle of the vector of the E_T^{miss} and the vector of the transverse momentum of the di-lepton system. The MC description is also reasonable.

Figure 57 displays the distributions of the sumet (scalar sum of the transverse energy of all the objects used for the computation of E_T^{miss} , $\sum E_T$) in data and MC. The upper plots display the total sumet. The rest of the plots show the contributions of the three components that the E_T^{miss} comprises in the current definition: calorimetric ($(\sum E_T)_{LH}$), muon and the calorimetric component that is matched to the muon. It is worth noting that, given past experience, we expect data to have busier-than-mc hadronic activity. This is seen in the two upper plots of Figure 57. The effect, however, is significantly smaller than observed earlier.⁹ The data-MC difference is small compared to the total $\sum E_T$ for both cases. The difference is larger for muons than it is for electrons. This needs to be investigated further.

Figure 58 shows the E_T^{miss} significance. The latter is defined as the ratio $E_T^{\text{miss}} / \sqrt{\sum E_T}$. The excess of events with moderate values of the E_T^{miss} significance may partially due to the residual contribution from continuum W^+W^- and top backgrounds. This will become clear when the corresponding MC samples will be added. The difference in the shape for the di-electron case is a bit worrisome and require further investigation.

⁸In the nominal analysis the ALPGEN samples are used instead. This is not a concern since we are investigating the E_T^{miss} performance after the application of a full jet veto.

⁹This may be due partially to the new improved description of the underlying event in MC.

| | $(\sum E_T)^{Data}$ | $(\sum E_T)^{MC}$ | Δ | $(\sum E_T)_{LH}^{Data}$ | $(\sum E_T)_{LH}^{MC}$ | Δ |
|----------|---------------------|-------------------|----------|--------------------------|------------------------|----------|
| ee | 241.8 | 239.3 | 2.4 | 241.7 | 239.3 | 2.4 |
| $\mu\mu$ | 243.9 | 239.2 | 4.7 | 169.8 | 163.9 | 5.9 |

Table 66: Average values of the total sumet and the calorimetric sumet in data and MC, and their difference. The results are given in GeV for the two di-lepton samples considered here (see text).

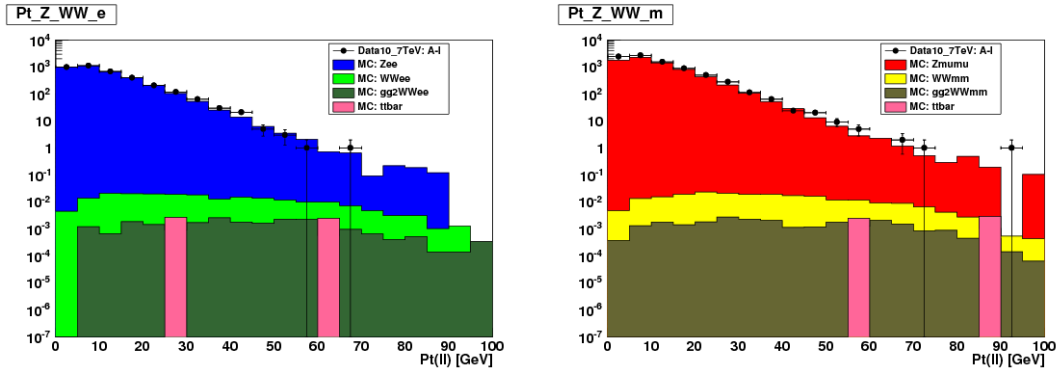


Figure 53: Distribution of the transverse momentum of the di-lepton system in data and MC for di-electrons (left) and di-muons (right).

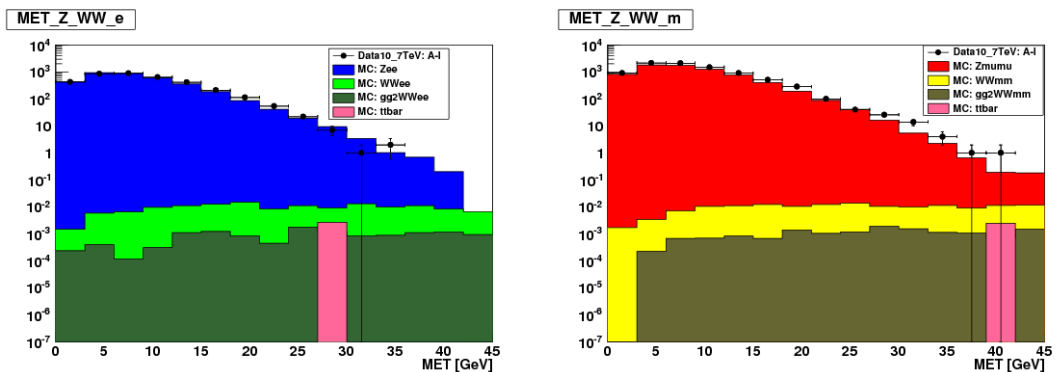


Figure 54: E_T^{miss} distribution in data and MC for di-electrons (left) and di-muons (right).

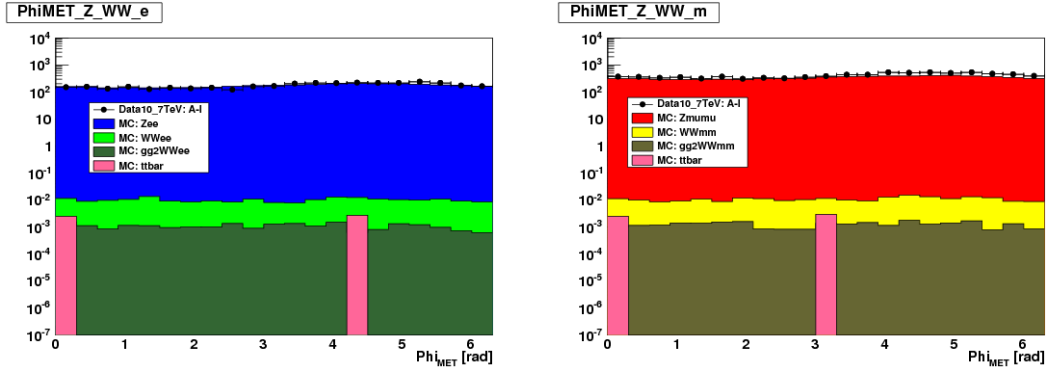


Figure 55: Distribution of azimuthal angle of the $E_{\text{T}}^{\text{miss}}$ in data and MC for di-electrons (left) and di-muons (right).

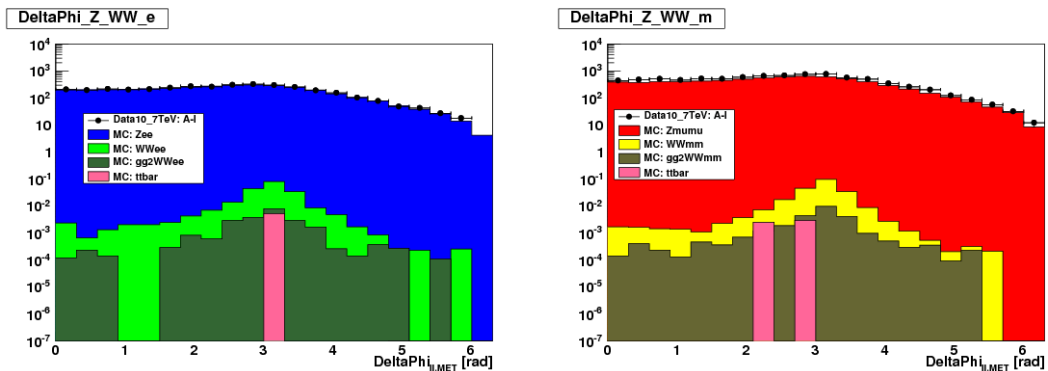


Figure 56: Distribution of the azimuthal angle difference between the $E_{\text{T}}^{\text{miss}}$ and the transverse momentum of the di-lepton system in data and MC for di-electrons (left) and di-muons (right).

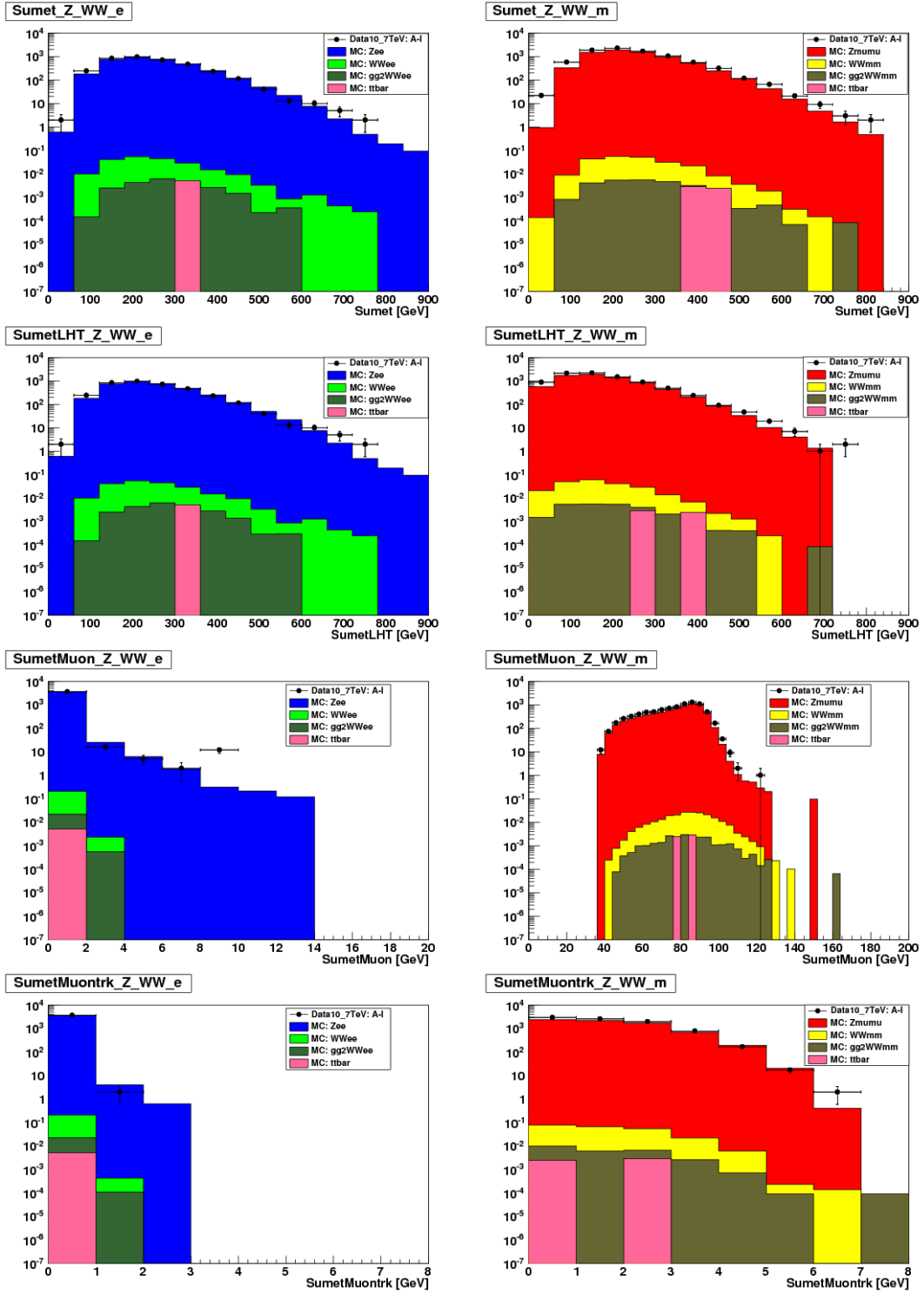


Figure 57: Distributions of the sumet in data and MC for di-electrons (left) and di-muons (right). The upper plots display the total sumet. The rest of the plots show the contributions of the three components that the E_T^{miss} comprises in the current definition (see text).

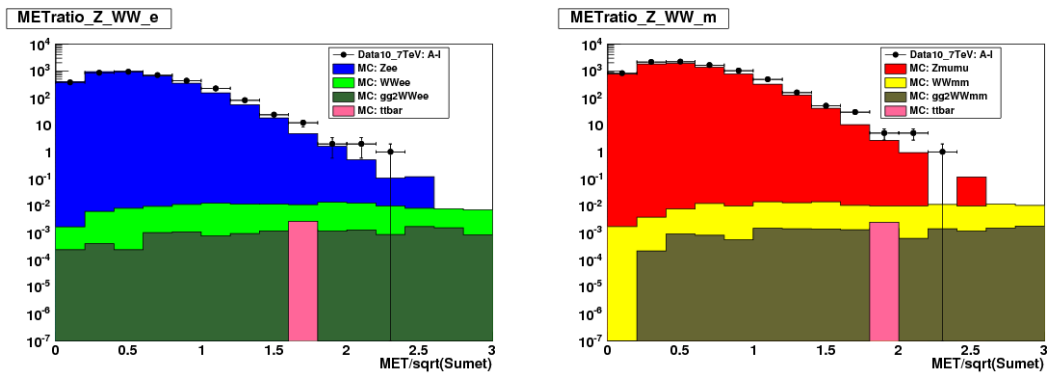


Figure 58: Distribution of the E_T^{miss} significance in data and MC for di-electrons (left) and di-muons (right).

E PDF Uncertainty of WW Acceptance

The calculation of the total cross-section takes into account the geometrical acceptance due to phase-space requirement and is entirely based on the Monte-Carlo simulations. The central value of the acceptance, A , is calculated based on the MC@NLO generated with CTEQ 6.6 NLO parton distribution function (PDF) and the corresponding ATLAS MC09 tune. The systematic uncertainties on the acceptances due to the limited knowledge of the proton PDFs comes from the error matrixes in CTEQ 6.6 and the differences in the central values of the acceptance between CTEQ and MSTW. There is no need to include NNLO uncertainty to the PDF systematics based on the fact that CTEQ 6.6 PDF set is obtained with the NLO Parton Shower kernel and NLO Matrix Element is used for WW acceptance calculation. The calculation of the acceptance uncertainties is itemized below:

- the uncertainty within CTEQ 6.6 PDF set is obtained by following a standard procedure described in the CTEQ manual. The symmetric uncertainty is evaluated by averaging positive and negative uncertainties.

$$\sigma^+ = \sigma^- = \frac{\sqrt{\sum_{i=0}^n [\max(A_i - A_0, 0)]^2} + \sqrt{\sum_{i=0}^n [\max(A_0 - A_i, 0)]^2}}{2A_0}, \quad (22)$$

where A_0 is the WW acceptance evaluated at the central value of CTEQ 6.6. The acceptance of the other PDF set is evaluated by applying event-by-event PDF re-weighting technique to the 9 WW signal samples listed in Table 3. The gg fusion production is ignored due to the small fraction (3%) of total WW production cross-section.

- the uncertainty between different PDF sets. It is estimated by comparing CTEQ6.6 to the central MSTW2008 NLO 68% CL PDF set.

The uncertainty calculated from 44 CTEQ6.6 error eigenvectors is 0.9%. The central value deviation from MSTW2008 NLO is 0.8%. The combined systematic uncertainty with quadratic sum is 1.2%. The PDF uncertainties of each dilepton channel are summarized in Table 67.

There are three independent studies carried out to cross-check this number and they are summarized in Table 67. These three studies are performed at the generator level with event selection cuts applied at the parton level. The first cross-check is based on the same procedure described above by using 1M PYTHIA events. The combined systematic uncertainties, 0.9%, is consistent to the MC@NLO re-weighting method. The second cross-check is done by replacing PYTHIA by MCFM samples generated with the CTEQ6M and CTEQ6.6 PDF sets. The third cross-check is based on comparing MC@NLO Monte Carlo samples produced with 3 additional different PDF sets: MRST2004 NLO, MRST2006 NNLO, HERAPDF. The results of MRST2006 NNLO and HERAPDF are listed as interesting comparisons. The relative large variations between different dilepton flavors are limited by Monte Carlo statistics.

In summary, the PDF systematic uncertainties of WW signal acceptance is determined to be 1.2%. All three cross-checks give results consistent with those obtained from the MC@NLO re-weighting method.

| Generator | PDF Set | ee (%) | $\mu\mu$ (%) | $e\mu$ (%) | ll (%) |
|----------------------|-----------------|--------|--------------|------------|----------|
| MC@NLO reweight | CTEQ6.6 44 sets | 0.9 | 0.9 | 0.9 | 0.9 |
| | MSTW2008 NLO | 0.6 | 1.0 | 0.8 | 0.8 |
| | Combined | 1.1 | 1.3 | 1.2 | 1.2 |
| PYTHIA reweight | CTEQ6.6 44 sets | 0.7 | 0.7 | 0.8 | 0.8 |
| | MSTW2008 NLO | 0.4 | 0.4 | 0.4 | 0.4 |
| | Combined | 0.8 | 0.8 | 0.9 | 0.9 |
| MCFM production | CTEQ6.6 44 sets | | | 0.7 | |
| | CTEQ6M 40 sets | | | 0.8 | |
| MC@NLO production | MRST2004 NLO | 0.8 | 0.6 | 0.1 | - |
| | MRST2006 NNLO | 0.8 | 0.1 | 0.2 | - |
| | HERAPDF | 0.9 | 1.4 | 1.8 | - |
| | (Max-Min)/2 | 0.8 | 1.0 | 0.9 | - |

Table 67: Summary of the fractional uncertainties of WW acceptance in each dilepton channels using PDF re-weighting in MC@NLO samples. The comparisons to three other independent cross-checks are also included.

F Additional W^+W^- Plots

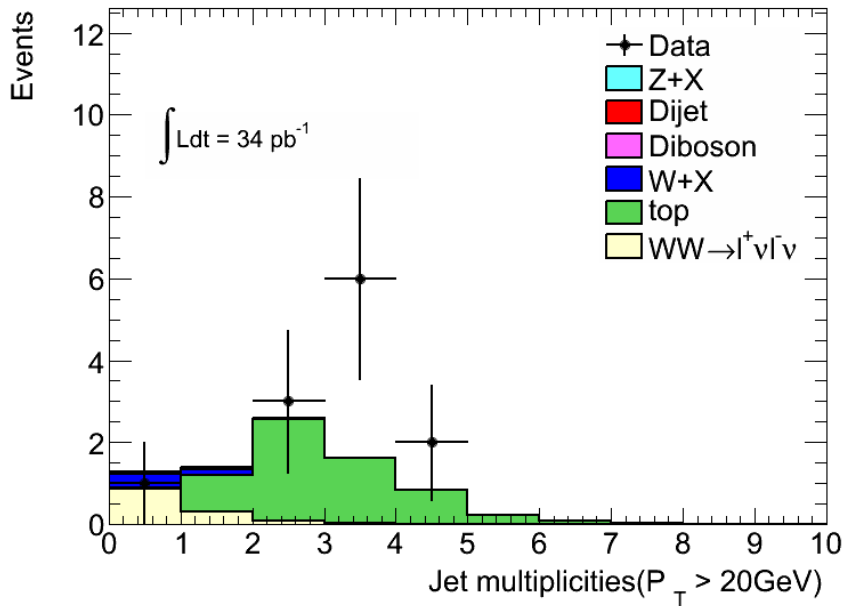


Figure 59: Jet multiplicity for events passing the full W^+W^- selection in ee channel except jet veto. The dots represent data and stacked histograms are from MC predictions.

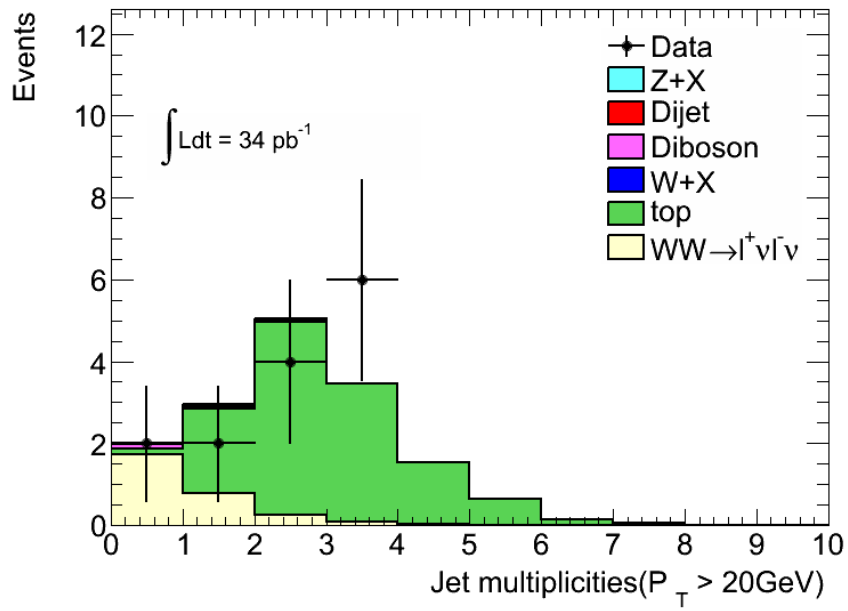


Figure 60: Jet multiplicity for events passing the full W^+W^- selection in $\mu\mu$ channel except jet veto. The dots represent data and stacked histograms are from MC predictions.

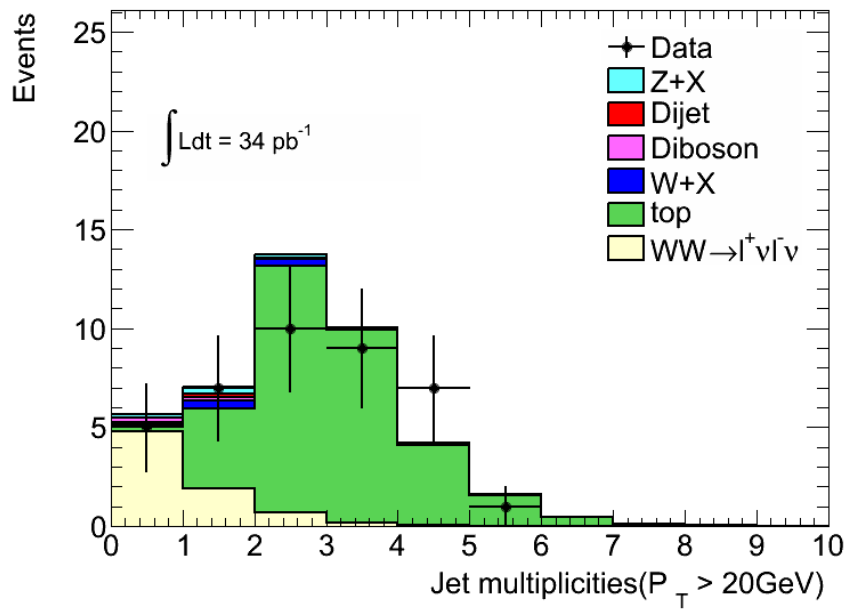


Figure 61: Jet multiplicity for events passing the full W^+W^- selection in $e\mu$ channel except jet veto. The dots represent data and stacked histograms are from MC predictions.

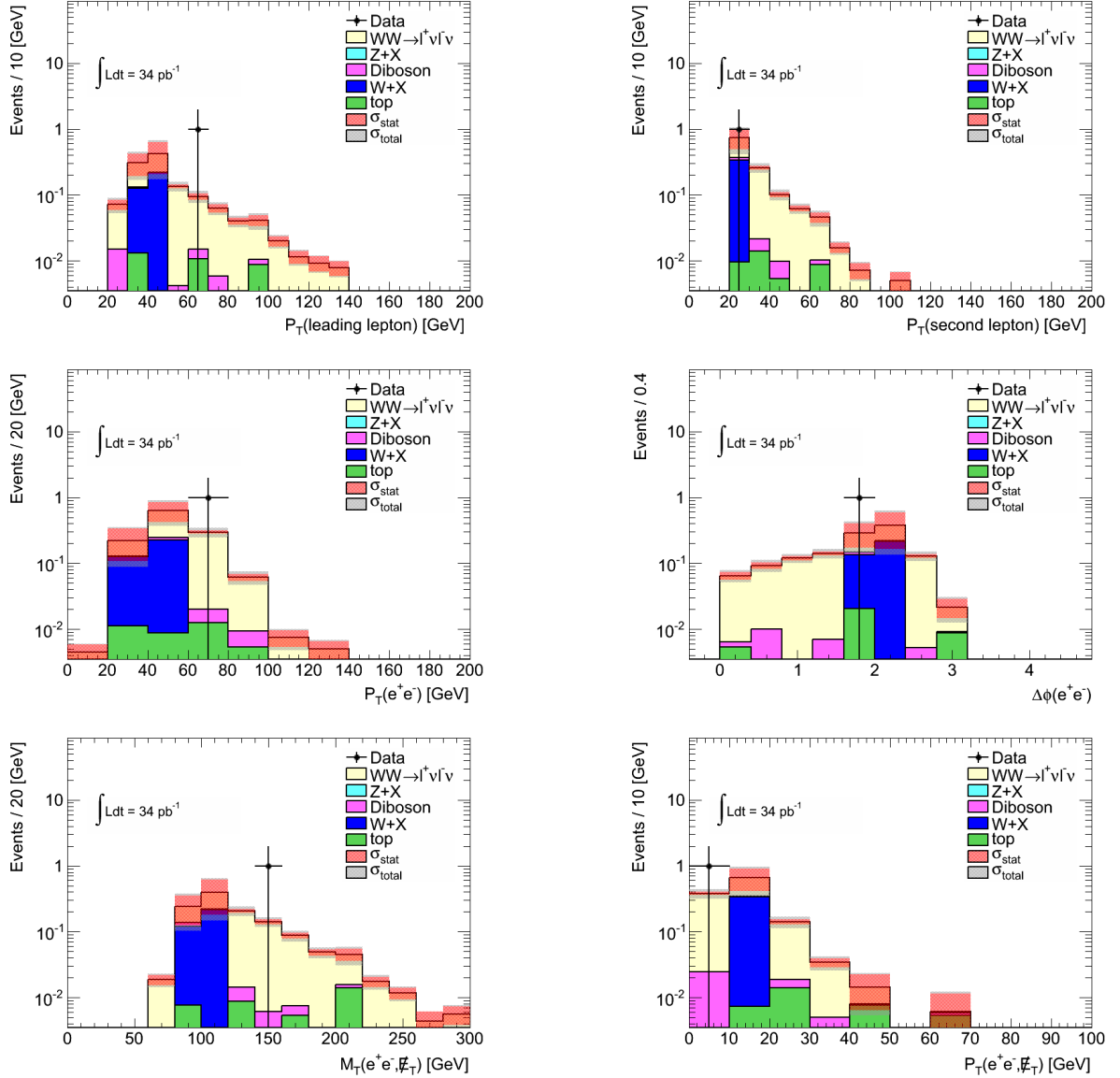


Figure 62: Distributions for W^+W^- candidates for combined ee channel: the first row is the p_T of leading lepton (left) and the p_T of trailing lepton (right); the second row is the $p_T(\ell\ell)$ (left) and the ϕ angle difference between two leptons (right); the third row is the M_T for di-lepton+ E_T^{miss} system (left) and p_T for di-lepton+ E_T^{miss} (right). The dots represent data and stacked histograms are from MC predictions. Scale factors (described in Section 6.7) are applied to MC.

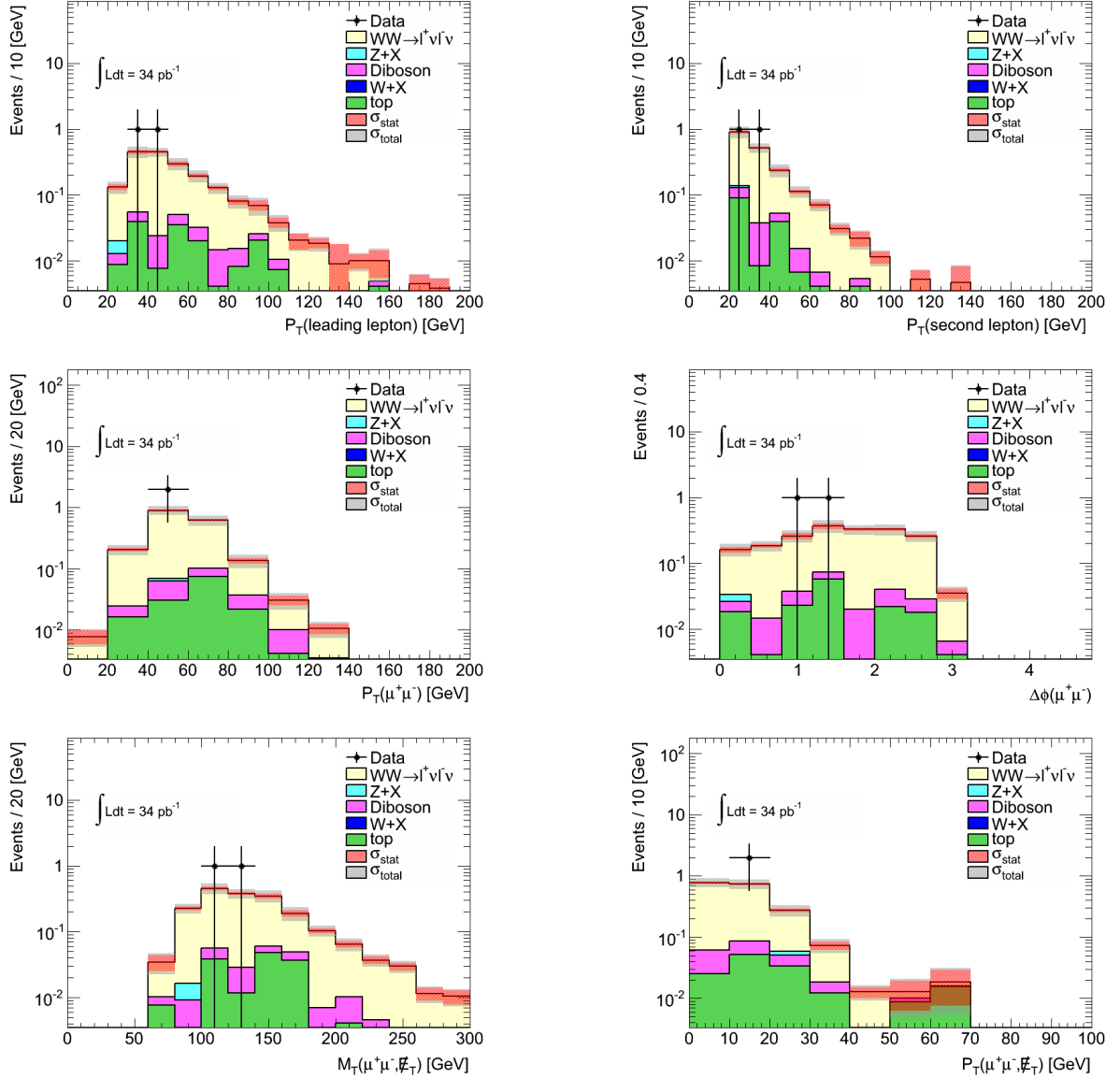


Figure 63: Distributions for $W^+ W^-$ candidates for combined $\mu\mu$ channel: the first row is the p_T of leading lepton (left) and the p_T of trailing lepton (right); the second row is the $p_T(\ell\ell)$ (left) and the ϕ angle difference between two leptons (right); the third row is the M_T for di-lepton+ E_T^{miss} system (left) and p_T for di-lepton+ E_T^{miss} (right). The dots represent data and stacked histograms are from MC predictions. Scale factors (described in Section 6.7) are applied to MC.

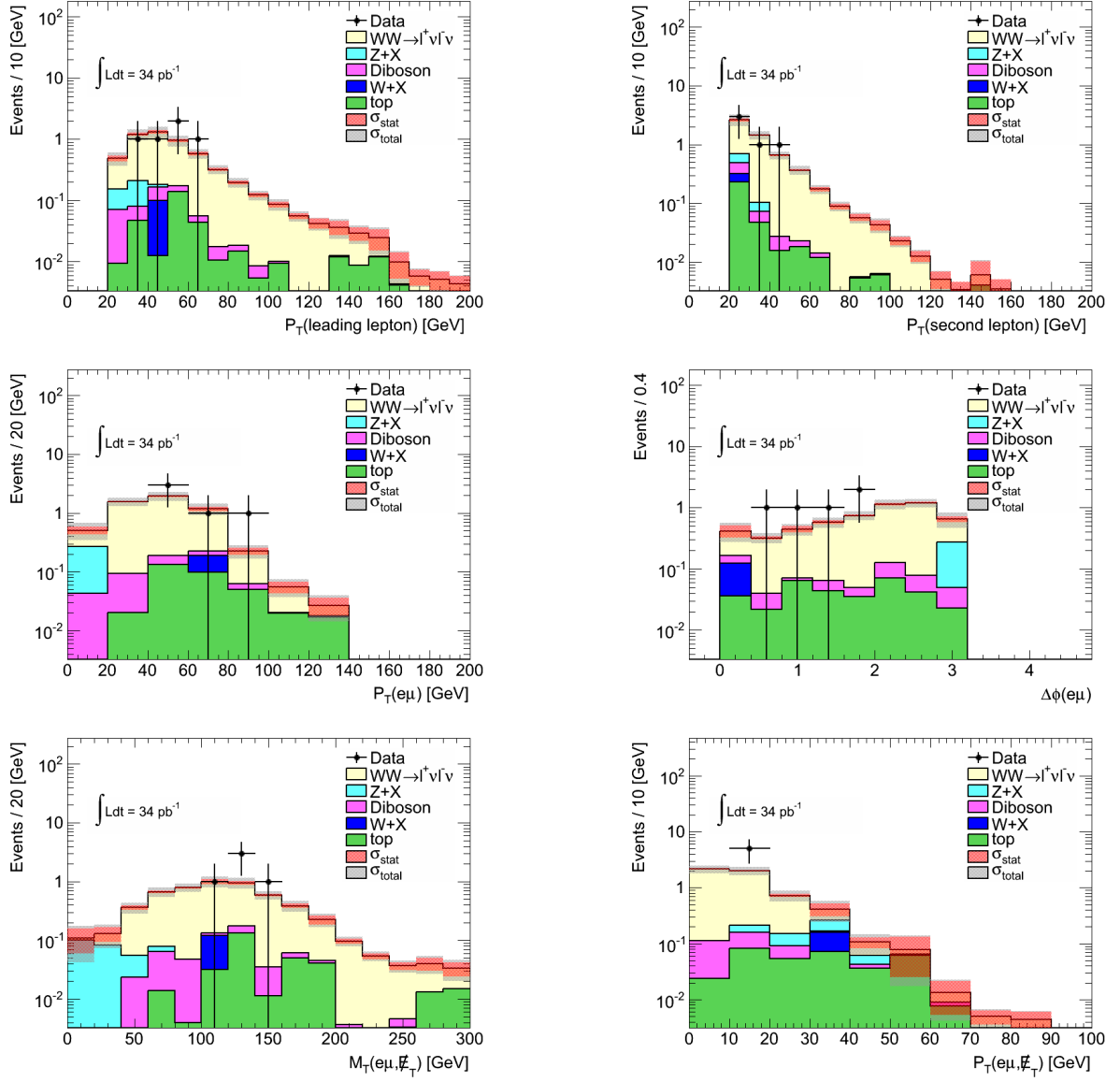


Figure 64: Distributions for W^+W^- candidates for combined $e\mu$ channel: the first row is the p_T of leading lepton (left) and the p_T of trailing lepton (right); the second row is the $p_T(\ell\ell)$ (left) and the ϕ angle difference between two leptons (right); the third row is the M_T for di-lepton+ E_T^{miss} system (left) and p_T for di-lepton+ E_T^{miss} (right). The dots represent data and stacked histograms are from MC predictions. Scale factors (described in Section 6.7) are applied to MC.

References

- [1] <https://atlas-datasummary.cern.ch/lumicalc/>.
- [2] <https://twiki.cern.ch/twiki/bin/viewauth/Atlas/GoodRunsListsTutorial>,
<https://atlasdqm.cern.ch/grl/>, <http://atlasdqm.web.cern.ch/atlasdqm/grlgen/>.
- [3] <https://twiki.cern.ch/twiki/bin/view/AtlasProtected/WWWZMCSamples>.
- [4] Stefano Frixione and Bryan Webber. <http://www.hep.phy.cam.ac.uk/theory/webber/MCatNLO/>.
- [5] G. Corcella et al. HERWIG 6.5: an event generator for Hadron Emission Reactions With Interfering Gluons (including supersymmetric processes). *JHEP*, 0101:010, 2001.
- [6] T. Bineth, M. Ciccolini, N. Kauer, and M. Kramer. Gluon-induced W-boson pair production at the LHC. *JHEP*, 12:046, 2006.
- [7] J.M. Butterworth et.al. ATL-COM-PHYS-2010-695.
- [8] Torbjorn Sjostrand et al. High-energy physics event generation with PYTHIA 6.1. *Comput. Phys. Commun.*, 135:238–259, 2001.
- [9] J Butterworth, E Dobson, U Klein, B Mellado Garcia, T Nunnemann, J Qian, D Rebuzzi, and R Tanaka. Single boson and diboson production cross sections in pp collisions at $\sqrt{s}=7$ tev. Technical Report ATL-COM-PHYS-2010-695, CERN, Geneva, Aug 2010.
- [10] T. Matsushita et al. <http://indico.cern.ch/conferenceDisplay.py?confId=121493g>.
- [11] G. Aad et al. The ATLAS Experiment at the CERN Large Hadron Collider. *JINST*, 3:S08003, 2008.
- [12] <http://alxr.usatlas.bnl.gov/lxr-stb5/source/atlas/Reconstruction/egamma/egammaEvent/egammaEvent/egammaPIDdefs.h>.
- [13] G Aad. Measurement of the $W \rightarrow l\nu$ and $Z/\gamma^* \rightarrow ll$ production cross sections in proton-proton collisions at $\sqrt{s} = 7$ TeV with the ATLAS detector. oai:cds.cern.ch:1299479. (arXiv:1010.2130. CERN-PH-EP-2010-037), Oct 2010. Comments: 38 pages plus author list (57 pages total), 16 figures, 15 tables.
- [14] <https://twiki.cern.ch/twiki/bin/view/AtlasProtected/EnergyScaleResolutionRecommendations>.
- [15] MCP group. <https://svnweb.cern.ch/trac/atlasgrp/browser/CombPerf/MuonPerf/Notes/2010-Autumn/MuonEfficiencyWithZNote/MuonEfficiencyWithZNote.pdf>.
- [16] M. Schott. <http://indico.cern.ch/getFile.py/access?contribId=4&resId=0&materialId=slides&confId=113455>.
- [17] MCP group. <https://twiki.cern.ch/twiki/bin/view/AtlasProtected/MCPAnalysisGuidelinesRel15>.
- [18] MCP group. Muon momentum resolution in first pass reconstruction of pp collision data recorded by atlas in 2010. https://svnweb.cern.ch/trac/atlasgrp/browser/CombPerf/MuonPerf/Notes/2010-Autumn/MuonMomentumResolutionNote/res_conf_note.pdf.
- [19] Matteo Cacciari, Gavin P. Salam, and Gregory Soyez. The anti-kt jet clustering algorithm. *JHEP*, 04:063, 2008.

- [20] Jet energy scale and its systematic uncertainty for jets produced in proton-proton collisions at $\sqrt{s} = 7$ tev and measured with the atlas detector. ATLAS-CONF-2010-056.
- [21] Jet energy resolution and selection efficiency relative to track jets from in-situ techniques with the ATLAS Detector Using Proton-Proton Collisions at a Center of Mass Energy $\sqrt{s} = 7$ TeV. Technical Report ATLAS-CONF-2010-054, CERN, Geneva, Jul 2010.
- [22] Jet energy scale and its systematic uncertainty for jets produced in proton-proton collisions at $\sqrt{s} = 7$ TeV and measured with the ATLAS detector. Technical Report ATLAS-CONF-2010-056, CERN, Geneva, Jul 2010.
- [23] Calibrating the b -Tag and Mistag Efficiencies of the SV0 b -Tagging Algorithm in 3 pb^{-1} of Data with the ATLAS Detector. Technical Report ATLAS-CONF-2010-099, CERN, Geneva, Dec 2010.
- [24] J M Campbell, E Castaneda-Miranda, Y Fang, N Kauer, B Mellado, and S L Wu. Normalizing Weak Boson Pair Production at the Large Hadron Collider. *Phys. Rev.*, D80:054023, 2009.
- [25] <https://twiki.cern.ch/twiki/bin/view/AtlasProtected/JetEtmissDataAnalysisRecommendationSummer2010>.
- [26] <https://twiki.cern.ch/twiki/bin/view/AtlasProtected/WZElectroweakCommonTopics>.
- [27] S Grinstein, M Martinez, E Meoni, C Ochando, and E Perez. Study on the impact of lepton-jet overlap removal in $Z (\rightarrow 1 + 1 -) + \text{jets}$ final states. (ATL-COM-PHYS-2010-021), Jan 2010.
- [28] <https://twiki.cern.ch/twiki/bin/view/atlasprotected/howtocleanjets>.
- [29] T Masubuchi. Data driven method of $w + \text{jets}$ fake background estimation for the $h \rightarrow w w^{(*)} \rightarrow \ell \nu \ell \nu$ decay mode. Technical Report ATL-COM-PHYS-2009-643, CERN, Geneva, Dec 2009.
- [30] Prospects for higgs boson searches using the $h \rightarrow w w^{(*)} \rightarrow \ell \nu \ell \nu$ decay mode with the atlas detector for 10 tev. Technical Report ATL-PHYS-PUB-2010-005, CERN, Geneva, Jun 2010.
- [31] J Barreiro Guimaraes da Costa et al. $W \rightarrow \mu \nu$ and $Z \rightarrow \mu \mu$ cross-sections measurements in proton-proton collisions at $\sqrt{s} = 7$ TeV with the ATLAS Detector. Technical Report ATL-COM-PHYS-2010-685, CERN, Geneva, Aug 2010. Support documentation for the $W \rightarrow \mu \nu$ and $Z \rightarrow \mu \mu$ cross section publication with 315 nb^{-1} .
- [32] Sven Moch and Peter Uwer. Theoretical status and prospects for top-quark pair production at hadron colliders. *Phys. Rev.*, D78:034003, 2008.
- [33] Borut Paul Kersevan and Elzbieta Richter-Was. The Monte Carlo event generator AcerMC version 2.0 with interfaces to PYTHIA 6.2 and HERWIG 6.5. 2004.
- [34] Peter Zeiler Skands. Tuning Monte Carlo Generators: The Perugia Tunes. *Phys. Rev.*, D82:074018, 2010.
- [35] S. Allwood-Spires et al. Monte Carlo samples used for top physics. ATL-COM-PHYS-2010-836, Oct 2010.
- [36] Liza Mijovic, TOP Cross-Section meeting on May 21 2010, <http://indico.cern.ch/conferenceDisplay.py?confId=80559>.
- [37] W/z+jet cross section measurements at the large hadron collider. ATL-PHYS-PROC-2009-062.

- [38] Marius Groll. Associated production of weak bosons at the LHC with the ATLAS detector. *J. Phys. Conf. Ser.*, 171:012086, 2009.
- [39] Updated luminosity determination in pp collisions at root(s)=7 tev using the atlas detector. ATLAS-CONF-2011-011.